Opening the system to the environment: new theories and tools in classical and quantum settings

Stefano Scali

Supervisors: Janet Anders, Simon Horsley

Submitted by Stefano Scali to the University of Exeter as a thesis for the degree of Doctor of Philosophy in Physics, September 2023.

To little Nora, hoping for you to find
passion, to be kind and open-minded.
Try everything you can, never settle.
Work hard but always have fun.

I wish you a wonderful life.

List of publications

- *SpiDy.jl - open-source Julia package for the study of non-Markovian stochastic dynamics* - **S Scali**, S Horsley, J Anders, F Cerisola (JOSS, submitted)
- *Accounting for quantum effects in atomistic spin dynamics* - M Berritta, **S Scali**, F Cerisola, J Anders - arXiv preprint arXiv:2305.17082 (PRB, accepted)
- *Anisotropic signatures in the spin-boson model* - F Hartmann, **S Scali**, J Anders - arXiv preprint arXiv:2305.16964 (PRB, accepted)
- *Graph theory approach to exceptional points in wave scattering* - **S Scali**, J Anders, SAR Horsley - Journal of Physics A: Mathematical and Theoretical
- *Quantum-classical correspondence in spin-boson equilibrium states at arbitrary coupling* - F Cerisola, M Berritta, **S Scali**, SAR Horsley, JD Cresser, J Anders - arXiv preprint arXiv:2204.10874 (PRX Quantum, in review)
- *Local master equations bypass the secular approximation* - **S Scali**, J Anders, LA Correa - Quantum 5, 451
- *Entanglement distance for arbitrary M-qudit hybrid systems* - D Cocchiarella, **S Scali**, S Ribisi, B Nardi, G Bel-Hadj-Aissa, R Franzosi - Physical Review A 101 (4), 042129
- *Entanglement estimation in non-optimal qubit states* - **S Scali**, R Franzosi - Annals of Physics (2019) 167995

Contents

List of Figures

1 Introduction

This thesis is a mix–and–match of topics that I found the most original and appealing during the time of my PhD. Rather than being a single–subject thesis, it is a tortuous stream of topics sometimes sharing very little with each other. Nonetheless, a single common factor pools all of them, I always consider open systems.

These few paragraphs are a little introduction of how this thesis ended up being the way it is. In my Masters project, I learned about the phenomenon of non–Hermitian singularities also know as exceptional points (EPs). In this first contact with non–Hermitian systems, I worked on microwave ring resonators and explored different geometrical setups to find EPs. I built the theory and the package to scan the parameter space searching for high–order EPs but I explored no physical consequences. This project was indeed my first contact with the world of open systems, classical in this case. Both the physical consequences and the classical/quantum aspects of the EPs remained a curiosity at this point. Starting my PhD, the next most natural step was to continue exploring the phenomenon of the EPs and more general characteristics of open systems in different frameworks and theories. For this reason, in this thesis, I study open system from several perspectives, from a pure quantum thermodynamic setting in the form of master equations (see Sec. 3), to classical wave scattering setups (see Sec. 2), to the stochastic dynamics with classical/quantum statistics of the spin-boson model (see Sec. 4). All these topics have in common some interaction with external sources or baths. In the first two topics, I built the theory and explored different aspects and consequences of the appearance of the EPs. In the latter, I have extended a theoretical framework of stochastic spin dynamics in the presence of non-Markovian interaction with a bath and contributed to define the quantum-to-classical correspondence of the model. In the latter project, I was also able to leverage my coding experience to build a full package for simulating the stochastic dynamics of spins and harmonic oscillators (see Sec. 5).

This thesis is a journey through which I tried to make different theories and tools dialogue. During this time, I independently learned and applied tools for the analysis of non–Hermitian degeneracies and explored, learned, and lost myself in the vastness (and wilderness) of graph theory. I have also autonomously learned

new coding languages and studied the best software practices in order to obtain quick and reliable stochastic simulations. The time for some expert guidance has been key when I tried to merge my "solo" topics with the topics of expertise of my supervisors and collaborators. In this process, I learned about master equations, wave scattering and spin–boson theories. As this naivety in the adoption of new topics might suggest to you, this thesis has not been built in a homogeneous manner. On the one hand, it is possible to read the different sections of the thesis independently and in any order. On the other hand, the order presented here is not chronological but rather it is the order I believe the topics can be better linked one another. Sometimes, they remain standalone, but always self-consistent.

As a mere curiosity of chronology, I firstly tackled the problem of EPs in open systems when Luis Correa was in Exeter. Then it was time for the COVID pandemic and there has been a time of adjustment (and struggle), ending in a major shift of topic, namely the spin–boson project led by Janet Anders. After this, another big jump happened, motivated by my interest for graph theory. Here, Simon Horsley proposed a possible theoretical platform and I started working on the interpretation of EPs via graph theory in wave scattering. During this time, I also finished rebuilding and continued improving the Julia package for stochastic simulations. This has been a symbiotic and very productive collaboration with Federico Cerisola. But as I mentioned, the story line in this thesis is not quite chronological.

The thesis is organized as follows. Section 2 is a first, unconventional, approach to the topic of EPs. Having grown interest in the topic of combinatorics and graph theory, I wanted to exploit its very abstract and mathematical tools to reinterpret something very physical, that is, the EPs in wave scattering. To do this, I build the interpretation of scattering events from a graph theory perspective and show how EPs can be understood within this interpretation. In Section 3, I move from a completely classical treatment to a purely quantum one. In this section, I consider two quantum resonators coupled to two baths and study their dynamics with local and global master equations. Here, the EPs are the key physical features used as a witness of validity of the master equation. Choosing the wrong master equation in the regime of interest can indeed mask physical and fundamental features of the system. In Section 4, there are no EPs. However I

transition towards a classical/quantum framework via the topic of open systems. My main contribution in this work is the classical stochastic treatment and simulation of a spin coupled to a bath. In this work, I show how a natural quantum–to–classical transition occurs at all coupling strengths when certain limits of spin length are taken. As a key result, I also show how the coupling to the environment in this stochastic framework induces a classical counterpart to quantum coherences in equilibrium. After this last topic, in Section 5, I briefly present the key features of the code I built (and later extended) for the latter project. This, in the form of a Julia registry package named *SpiDy.jl*, has seen further applications in branching projects and allows for further exploration of the theoretical framework. Finally, I conclude with a discussion section (see Sec. 6) where I recap the different conclusions gathered in the previous sections and propose several possible directions.

2 Graph theory approach to exceptional points in wave scattering

2.1 Statement of contribution

In the following work, I devised the idea to apply graph theory to wave scattering problems, while the idea to use the same framework to describe exceptional point conditions followed as a consequence. Thus, I learned and developed graph theory, built the code, generated the results and wrote the paper. The target platform in the form of discrete dipole approximation has been proposed by Simon Horsley while I revised and rewrote the derivation.

Note that this section requires the reader to familiarize with specific and slightly technical graph theoretic definitions and terms. These are only reported in the main text but are expanded with relative examples in the appendices. For this reason and given how independent the different sections are, the reader can choose to start from another section and come back to this later.

2.2 Summary

In this section, we use graph theory to solve wave scattering problems in the discrete dipole approximation. As a key result of this work, in the presence of active scatterers, we present a systematic method to find arbitrary large–order zero eigenvalue exceptional points (EPs). This is achieved by solving a set of non–linear equations that we interpret, in a graph theory picture, as vanishing sums of scattering events. We then show how the total field of the system responds to parameter perturbations at the EP. Finally, we investigate the sensitivity of the power output to imaginary perturbation in the design frequency. This perturbation can be employed to trade sensitivity for a different dissipation balance of the system. The purpose of the results of this section is manifold. On the one hand, we aim to shed light on the link between graph theory and wave scattering. On the other hand, the results of this section find application in all those settings where zero eigenvalue EPs play a unique role like in coherent perfect absorption (CPA) structures.

2.3 Introduction

Although wave scattering is an elementary process and straightforward to picture, its analysis continues to fuel developments in electromagnetic and acoustic material research. While a small object (particle) scatters as a point source with a strength proportional to the applied field, larger objects scatter the wave between their constituent parts. This multiple scattering process is an infinite chain of possible scattering events, interfering to give the total field. This complicated interaction breaks the simple relationship between the applied and scattered wave amplitudes. From this complex interaction, several fields of research emerge including metamaterials [1], photonic crystals [2], propagation and imaging through disordered media [3], and random lasing [4].

The last decade has seen a large body of research into wave scattering in non–Hermitian materials, originating from Bender's proposed parity–time symmetric extension to quantum mechanics [5]. Non–Hermitian materials differ from ordinary matter in that they are usually driven, containing regions where the wave can be amplified, in addition to regions of absorption. This absorption and re–emission of wave energy provides much more control over the wave field compared to passive structures, demonstrated in designs for invisible and reflectionless media [6, 7, 8], cloaking [9], one–way propagation [10], coherent perfect absorption [11, 12], and disordered media without scattering [13]. Controlled wave amplification has now been demonstrated from GHz [14] to optical frequencies [15], as well as in acoustics [16, 17, 18].

In this work, we investigate the problem of designing non–Hermitian arrays of particles with controllable exceptional point degeneracies. Exceptional points (EPs) are peculiar to non–Hermitian materials where two or more modes of the system have both eigenvalues and eigenvectors that coalesce. They have attracted considerable interest [19] exhibiting an apparently increased sensitivity to system perturbations [20, 21], with the degenerate modes transforming into one another after cycling the system parameters [22, 23]. To the best of our knowledge, while extensive work has been done on higher–order exceptional points [21, 24, 25], no consistent method to find N^{th}–order EPs in wave scattering systems has been presented yet. In this work, we provide a recipe based on graph theory for implementing an exceptional point of arbitrary order in a sys-

tem of scattering particles. The resulting system exhibits scattering properties with an extreme sensitivity to small changes in the particles' positions.

Our graph theory approach is based on the discrete dipole approximation (DDA) [26, 27]. This is an established method for calculating the field scattered from any configuration of N particles. Originally introduced by Purcell to calculate the scattering from astrophysical dust [28], this method is now commonly applied to, e.g., metamaterial design [29, 30] and wave propagation in disordered media [31] thanks to its vast range of validity [32]. By treating the particles as point sources, with a strength proportional to the incident field, the scattering problem can be solved self consistently determining the field on each particle. This requires the inversion of an $N \times N$ matrix, which rapidly becomes analytically intractable as the number of particles (scatterers) increases. Here, we provide a graph theory representation of this matrix inversion. We use this to understand the requirements on the scatterer parameters for the system to exhibit an exceptional point of arbitrary order, finding a remarkably simple picture in terms of vanishing sums of graphs related to different scattering events.

The section is organized as follows: in Sec. 2.4, we review the discrete dipole approximation (DDA). In Sec. 2.5, we show how to interpret DDA by means of graph theory. In Sec. 2.6, we derive the single scattering events and define orders of interactions. By means of the graph theory interpretation, we perform and give insights on weak and strong interaction limits. In Sec. 2.7, we present a method to design N^{th}–order EPs with zero eigenvalue in systems described by DDA, perhaps the most important result of this section. To do this, we derive the conditions to find these EPs (Sec. 2.7.1) and, consequently, we interpret these conditions in terms of graphs in a scattering setting (Sec. 2.7.2). In this setting, we show the effects of the EPs on the system's properties (Sec. 2.7.3), namely the total field and the power output. Finally, we show how one can exploit perturbations to the design resonant frequency to tune the dissipation balance across the array of scatterers. However, this comes at the cost of a broader power output. In Sec. 2.8, we conclude by summarizing the results and possible next developments.

2.4 Discrete dipole approximation

Within the discrete dipole approximation (also discrete dipole method) an object is treated as a collection of dipoles. This theory has its power in the fact that anything, if cut into small enough pieces, can be considered a collection of dipoles. This treatment is equivalent to replacing the continuous susceptibility χ of an object with a discrete sum, that is

$$\varepsilon_r(\boldsymbol{x}) - 1 = \chi(\boldsymbol{x}) \sim \sum_{n=1}^{N} \bar{\alpha}_n \delta(\boldsymbol{x} - \boldsymbol{x}_n), \tag{1}$$

where the sum runs over the N dipoles in the collection at the positions $\boldsymbol{x}_n$ with the polarizabilities $\bar{\alpha}_n$ and $\varepsilon_r(\boldsymbol{x})$ is the relative permittivity of the material. Throughout this work, we assume constant polarizabilities although frequency–dependent ones can be considered. The additional dependency would open the system to further engineering possibilities and realizations. Note that, in addition, while this dependency would hinder the calculations throughout this section, all the core results and interpretations would be preserved. Eq.(1) represents the response of the material to a field at the position $\boldsymbol{x}$. Note that this discrete sum is always valid provided the number of "pieces" N is large enough. To understand how a material with such susceptibility behaves in an electric field $\boldsymbol{E}(\boldsymbol{x})$ at a fixed frequency ω_0, we consider the dynamical Maxwell equations,

$$\boldsymbol{\nabla} \times \boldsymbol{E}(\boldsymbol{x}) = -\frac{\partial \boldsymbol{B}(\boldsymbol{x})}{\partial t} = i\omega_0 \mu_0 \boldsymbol{H}(\boldsymbol{x}) \tag{2}$$

$$\boldsymbol{\nabla} \times \boldsymbol{H}(\boldsymbol{x}) = \boldsymbol{j}(\boldsymbol{x}) + \frac{\partial \boldsymbol{D}(\boldsymbol{x})}{\partial t} = \boldsymbol{j}(\boldsymbol{x}) - i\omega_0 \varepsilon_0 \varepsilon_r(\boldsymbol{x}) \boldsymbol{E}(\boldsymbol{x}), \tag{3}$$

where we used the relations between the displacement field $\boldsymbol{D}(\boldsymbol{x})$ and the electric field $\boldsymbol{E}(\boldsymbol{x})$ in a linear, homogeneous, isotropic material and the relation between the magnetizing field $\boldsymbol{H}(\boldsymbol{x})$ and the magnetic field $\boldsymbol{B}(\boldsymbol{x})$. Here, $\boldsymbol{j}(\boldsymbol{x})$ is the current density of an external source and ε_0 is the vacuum permittivity of the material. Inserting the discretization of Eq.(1) in Eq.(3) and combining the two Maxwell equations, we obtain

$$\boldsymbol{\nabla} \times \boldsymbol{\nabla} \times \boldsymbol{E}(\boldsymbol{x}) = \omega_0^2 \mu_0 \varepsilon_0 \Big[1 + \sum_{n=1}^{N} \bar{\alpha}_n \delta(\boldsymbol{x} - \boldsymbol{x}_n)\Big] \boldsymbol{E}(\boldsymbol{x}) + i\omega_0 \mu_0 \boldsymbol{j}(\boldsymbol{x}). \tag{4}$$

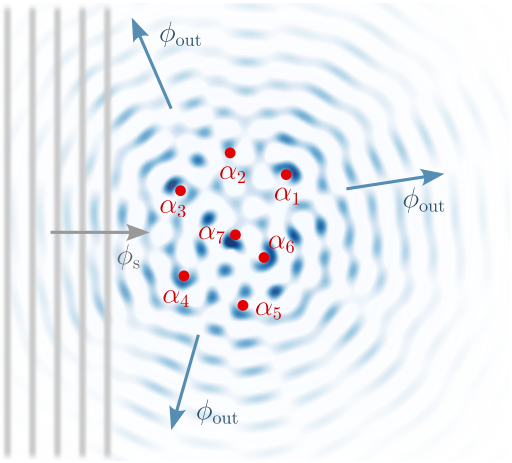

Figure 1: Schematic of a source field ϕ_{s} incident onto an array of sub–wavelength size scatterers (red dots) with polarizabilities α_n. The scatterers respond to the source field, producing an outgoing field $\phi_{\text{out}} = \sum_n \phi_n^{\text{out}}$.

We now use the vector identity $\boldsymbol{\nabla} \times \boldsymbol{\nabla} \times \boldsymbol{E}(\boldsymbol{x}) = \boldsymbol{\nabla}\big(\boldsymbol{\nabla} \cdot \boldsymbol{E}(\boldsymbol{x})\big) - \nabla^2 \boldsymbol{E}(\boldsymbol{x})$ and redefine the polarizabilities as $\tilde{\alpha}_n = -k_0^2 \bar{\alpha}_n$ with $k_0^2 = \omega_0^2/c^2 = \omega_0^2 \mu_0 \varepsilon_0$. Considering a source with zero charge density but non–zero current density $\boldsymbol{j}(\boldsymbol{x})$ (e.g. for acoustic waves), we find the vector Helmholtz equation for the electric field, the core of the discrete dipole approximation,

$$(\nabla^2 + k_0^2)\boldsymbol{E}(\boldsymbol{x}) = \sum_{n=1}^{N} \tilde{\alpha}_n \delta(\boldsymbol{x} - \boldsymbol{x}_n)\boldsymbol{E}(\boldsymbol{x}) + \mathrm{s}(\boldsymbol{x}), \tag{5}$$

where $\mathrm{s}(\boldsymbol{x}) = -i\omega_0\mu_0 \boldsymbol{j}(\boldsymbol{x})$ is the externally driven source of waves in the system.

For simplicity, we restrict our theory to scalar waves of amplitude ϕ (e.g., the pressure of an acoustic wave in a fluid or, in two dimensions, the fundamental mode of a waveguide), although there is no obstacle to adapting our theory to vector waves. A model of the system presented in the following is shown in Fig. 1. We take N scattering particles of polarizability α_n, with $n = 1, 2, \cdots, N$. Subject to an incoming wave of amplitude ϕ_{inc}, each of these particles will act as a point source s_n of strength

$$\mathrm{s}_n(\boldsymbol{x}) = \alpha_n \, \phi_{\text{inc}}(\boldsymbol{x}_n) \, \delta^{(3)}(\boldsymbol{x} - \boldsymbol{x}_n). \tag{6}$$

Note that the incoming field $\phi_{\text{inc}}(\boldsymbol{x}_n)$ is defined as the total field at position $\boldsymbol{x}_n$ (i.e. the position of the scatterer with polarizability α_n) minus the self–field of the scatterer. In this case, we use the incident field to remove the divergence of the

dipole self–field at the position $\boldsymbol{x} = \boldsymbol{x}_n$. For this reason, the polarizabilities of the scatterers are redefined as the response of the n–th dipole to the incident field. The total field $\phi(\boldsymbol{x})$ obeys the three dimensional Helmholtz equation, including the sources of scattered waves given in Eq. (6),

$$(\nabla^2 + k_0^2)\phi(\boldsymbol{x}) = \sum_{n=1}^{N} \alpha_n \, \phi_{\mathrm{inc}}(\boldsymbol{x}_n) \, \delta^{(3)}(\boldsymbol{x} - \boldsymbol{x}_n) + \mathrm{s}(\boldsymbol{x}), \tag{7}$$

where $k_0 = \omega_0/c$ is the wavenumber with ω_0 the resonant frequency, and $\mathrm{s}(\boldsymbol{x})$ is the externally driving source of waves in the system. Throughout this section, we assume $c = 1$. The solution to the Helmholtz equation (7) can be written in terms of the 3D Green's function $G(\boldsymbol{x}, \boldsymbol{x}_n) = -\exp\big(ik_0|\boldsymbol{x} - \boldsymbol{x}_n|\big)/(4\pi|\boldsymbol{x} - \boldsymbol{x}_n|)$, which is the solution to $(\nabla^2 + k_0^2)G(\boldsymbol{x}, \boldsymbol{x}_n) = \delta^{(3)}(\boldsymbol{x} - \boldsymbol{x}_n)$. Integrating the Green function against the right hand side of Eq. (7) we have the solution to Eq. (7), which takes the form

$$\phi(\boldsymbol{x}) = \sum_{n=1}^{N} \alpha_n \, G(\boldsymbol{x}, \boldsymbol{x}_n) \, \phi_{\mathrm{inc}}(\boldsymbol{x}_n) + \phi_{\mathrm{s}}(\boldsymbol{x}), \tag{8}$$

where $\phi_{\mathrm{s}}(\boldsymbol{x})$ is the integral of the Green's function over the source $\mathrm{s}(\boldsymbol{x})$. To determine the unknowns $\phi_{\mathrm{inc}}(\boldsymbol{x}_n)$, Eq. (8) is evaluated on each of the N scatterers, excluding the infinite self–field, and demanding self–consistency,

$$\phi_{\mathrm{inc}}(\boldsymbol{x}_m) = \sum_{\substack{n=1 \\ n \neq m}}^{N} \alpha_n \, G(\boldsymbol{x}_m, \boldsymbol{x}_n) \, \phi_{\mathrm{inc}}(\boldsymbol{x}_n) + \phi_{\mathrm{s}}(\boldsymbol{x}_m). \tag{9}$$

To write the problem in a more convenient form, we scale our field amplitudes by the polarizability, defining the new set of unknowns $\tilde{\phi}_{\mathrm{inc}}(\boldsymbol{x}_n) = \alpha_n \, \phi_{\mathrm{inc}}(\boldsymbol{x}_n)$. Writing Eqs. (9) in matrix form, the solution is

$$\boldsymbol{M}^{-1}\boldsymbol{\phi}_{\mathrm{s}} = \tilde{\boldsymbol{\phi}}_{\mathrm{inc}}, \tag{10}$$

where the *interaction matrix* $\boldsymbol{M}$ is given by

$$\boldsymbol{M} = \begin{pmatrix} \alpha_1^{-1} & -G(\boldsymbol{x}_1, \boldsymbol{x}_2) & -G(\boldsymbol{x}_1, \boldsymbol{x}_3) & \dots \\ -G(\boldsymbol{x}_2, \boldsymbol{x}_1) & \alpha_2^{-1} & -G(\boldsymbol{x}_2, \boldsymbol{x}_3) & \dots \\ -G(\boldsymbol{x}_3, \boldsymbol{x}_1) & -G(\boldsymbol{x}_3, \boldsymbol{x}_2) & \alpha_3^{-1} & \dots \\ \vdots & \vdots & \vdots & \ddots \end{pmatrix}, \tag{11}$$

with the source field vector $\boldsymbol{\phi}_\mathrm{s} = (\phi_\mathrm{s}(\boldsymbol{x}_1), \phi_\mathrm{s}(\boldsymbol{x}_2), \cdots, \phi_\mathrm{s}(\boldsymbol{x}_N))^T$, and the incident field vector $\tilde{\boldsymbol{\phi}}_\mathrm{inc} = (\tilde{\phi}_\mathrm{inc}(\boldsymbol{x}_1), \tilde{\phi}_\mathrm{inc}(\boldsymbol{x}_2), \cdots, \tilde{\phi}_\mathrm{inc}(\boldsymbol{x}_N))^T$. Note that, in general, the matrix $\boldsymbol{M}$ is non–Hermitian, being both complex and symmetric. In non-reciprocal systems [33], the interaction matrix is both complex and asymmetric. From Eq. (10), we can therefore find a solution for the incident fields $\tilde{\boldsymbol{\phi}}_\mathrm{inc}$ and consequently the total field $\phi(\boldsymbol{x})$ using Eq. (8). This is the discrete dipole approximation (DDA) method for solving scattering problems [26, 28, 34], reducing the entire problem to the matrix inversion $\boldsymbol{M}^{-1}$. This must be done numerically even for a small number of scatterers [27].

2.5 Graph theory interpretation of wave scattering

Graph theory is a branch of mathematics rooted in Euler's solution to the problem of the seven bridges of Königsberg [35]. From here, graph theory stemmed and evolved, finding applications to many problems in science and engineering [36].

The interaction matrix $\boldsymbol{M}$ in Eq. (11) can be represented as a graph (e.g., in panel (a) of Fig. 2), where the diagonal elements (the particles' self-interaction $1/\alpha_i$) are represented as vertices, and their interaction ($-G(\boldsymbol{x}_i, \boldsymbol{x}_j)$) as edges. Multiple scattering events between the particles can thus be represented as a path on this graph, known as a Coates digraph. This representation links interactions and objects to edges and vertices respectively, fundamental constituents of any graph.

For example, take a 4–scatterer system whose matrix $\boldsymbol{M}_4$ is the 4×4 equivalent of Eq. (11). In panel (a) of Fig. 2, we represent the matrix $\boldsymbol{M}_4$ as the complete Coates digraph $D^*(\boldsymbol{M}_4)$. Following convention [37, 38], we refer to the Coates digraph using a star superscript. The Coates digraph is constructed as follows: the scatterers are represented by vertices, the Green's function interactions take the

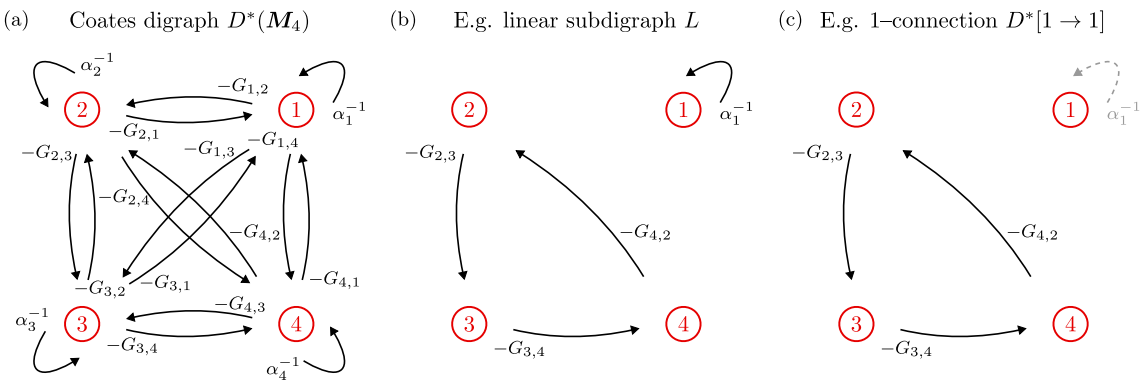

Figure 2: Example graphs used to describe the scattering system and the single scattering events. In panel (a), we show the Coates digraph $D^*(\boldsymbol{M}_4)$, representation of the matrix $\boldsymbol{M}_4$. The vertices represent the scatterers with the self–loops weighted by the inverse polarizabilities α_i^{-1} while the edges represent the interactions weighted by the Green's functions $G_{i,j} = G(\boldsymbol{x}_i, \boldsymbol{x}_j)$. Note that the labels of self–loops and edges are always placed as close as possible to the origin of the arrows they refer to. In panel (b), we show an example of linear subdigraph L of $D^*(\boldsymbol{M}_4)$, i.e., a subdigraph in which exactly one edge enters and exactly one edge leaves each vertex. Summing the weights of all the linear subdigraphs of $D^*(\boldsymbol{M}_4)$, one obtains $\det(\boldsymbol{M}_4)$. In panel (c), we show an example of 1–connection $D^*[1 \to 1]$ built from the linear subdigraph L. This is built by removing the edge $1 \to 1$, as described in the main text. Summing the weights of all the 1–connections from i to j, one obtains $\mathrm{adj}(\boldsymbol{M}_4)_{i,j}$.

role of the edges, and the intrinsic (inverse) polarizabilities of the single scatterers are identified by the vertices' self–loops. This graph earns the technical name of *vertex–labeled directed weighted simple graph permitting loops* [39, 40]. From now on, we will shorten and refer to this type of graphs as digraphs or simply graphs.

This interpretation of the interaction matrix allows us to calculate the inversion of the matrix in Eq. (10) using graph theory. To do this, we consider the usual formula for the inversion of a matrix [41],

$$\boldsymbol{M}^{-1} = \frac{\mathrm{adj}(\boldsymbol{M})}{\det(\boldsymbol{M})}, \tag{12}$$

where $\mathrm{adj}(\boldsymbol{M})$ and $\det(\boldsymbol{M})$ are the adjugate (transpose of the cofactor matrix) and the determinant of $\boldsymbol{M}$, respectively. The i,j–th element of the adjugate matrix is defined as $\mathrm{adj}(\boldsymbol{M})_{i,j} = (-1)^{i+j} \det\big(\boldsymbol{M}_{(j,i)}\big)$, where $\boldsymbol{M}_{(j,i)}$ is the minor[1] built by removing the j^{th} row and the i^{th} column from the matrix $\boldsymbol{M}$. Therefore, both

[1] In this section, we call a "minor" an $n \times n$ matrix built by removing m rows and columns from an $N \times N$ matrix, with $N = m + n$. We will refer to the determinant of such a matrix as the "determinant of a minor".

terms on the right hand side of Eq. (12) depend on determinant evaluations.

This form of inversion has a distinct interpretation in graph theory. It is thanks to this graph interpretation that we will be able to distinguish and identify different scattering events, ultimately solving for the total field of the system. In addition, using the same interpretation, we will illustrate a new visual way to build the condition to find zero eigenvalue EPs in scattering systems.

The determinant of a generic matrix $\boldsymbol{A}$ can be calculated using the Coates' determinant formula [37, 38, 42],

$$\det(\boldsymbol{A}) = (-1)^N \sum_{L \in \mathscr{L}(\boldsymbol{A})} (-1)^{c(L)} \gamma(L), \tag{13}$$

where N is the number of vertices of the Coates digraph $D^*(\boldsymbol{A})$ and L is an element in the set $\mathscr{L}(\boldsymbol{A})$ of all the possible linear subdigraphs of the Coates digraph $D^*(\boldsymbol{A})$ [37]. A linear subdigraph of the Coates digraph $D^*(\boldsymbol{A})$ is a subdigraph of $D^*(\boldsymbol{A})$ in which exactly one edge enters and exactly one edge leaves each vertex [38, 42]. The term $\gamma(L)$ is the product of the weights (see below) of the edges of L, and $c(L)$ is the number of cycles contained in L, i.e., the number of closed loops of the specific graph.

In panel (b) of Fig. (2), we show an example of a linear subdigraph L of the Coates digraph $D^*(\boldsymbol{M}_4)$ (with $N = 4$). Following the just mentioned definition, note that exactly one edge enters and leaves each vertex. The number of cycles of this graph is $c(L) = 2$, while its weight is $\gamma(L) = -\alpha_1^{-1} G_{2,3} G_{3,4} G_{4,2}$. Following the same procedure applied in this example, we obtain the determinant of the matrix $\boldsymbol{A}$ by simply adding, according to Eq. (13), the appropriately–signed weights of the linear subdigraphs of $D^*(\boldsymbol{A})$.

Using a similar construction, the expression for the adjugate of a generic matrix $\boldsymbol{A}$ is [38],

$$\mathrm{adj}(\boldsymbol{A})_{i,j} = (-1)^N \sum_{D^*[i \to j]} (-1)^{c(D^*[i \to j])+1} \gamma(D^*[i \to j]), \tag{14}$$

where the sum runs over all the possible 1–connections $D^*[i \to j]$ of the Coates digraph. A 1–connection $D^*[i \to j]$ is obtained from a linear subdigraph (containing the edge $j \to i$) by simply removing the edge $j \to i$. Note that, in the case $i = j$, this corresponds to removing the self–loop at vertex i.

An example 1–connection is shown in panel (c) of Fig. 2. Starting by considering the linear subdigraph L in panel (b), we remove the edge $j \to i$, that is, the self–loop $1 \to 1$. In this way, we obtain the corresponding 1–connection having number of cycles $c(D^*[1 \to 1]) = 1$ and weight $\gamma(D^*[1 \to 1]) = -G_{2,3}G_{3,4}G_{4,2}$. Following the same procedure applied in this example, we obtain the adjugate element i, j of the matrix $\boldsymbol{A}$ by simply adding, according to Eq. (14), the appropriately–signed weights of the 1–connections of $D^*([i \to j])$. See appendix A.1 for further examples and more formal definitions of Coates digraphs, linear subdigraphs, and 1–connections.

As a result, we can graphically represent Eqs. (14) and (13) for the matrix inversion (12), key for the evaluation of the total field of the system (8). These graph theory constructions, namely 1–connections and linear subdigraphs, give us a visual and systematic way of computing the elements of the inverse matrix $\boldsymbol{M}^{-1}$. I.e., each element $(\boldsymbol{M}^{-1})_{i,j} = \mathrm{adj}(\boldsymbol{M})_{i,j}/\det(\boldsymbol{M})$ is evaluated by dividing the weighted sum of the 1–connections from vertex i to j by the weighted sum of the linear subdigraphs of $D^*(\boldsymbol{M})$. As seen in section 2.4, this inverse allows us to solve for the total field of the system (8). Although graph theory doesn't reduce the number of calculations required to perform this inversion, it provides an intuitive representation of any scattering process in terms of a sequence of multiple scattering events. As we shall see, this allows us to give a graphical recipe for finding exceptional points in resonant scatterer arrays.

2.6 Identification of different scattering orders

Before treating the problem of exceptional points in these scatterer arrays, we show how we can use Eqs. (13) and (14) for the construction of the elements of the inverse matrix $\boldsymbol{M}^{-1}$ in the case of weak and strong interaction limits of the system. These limits are taken by controlling the order of magnitude of the distance between the scatterers (large distance between scatterers being equivalent to weak coupling and vice versa) relative to the magnitude of the wavenumber used to probe the system. This results in a change of the interaction terms in the form of Green's functions G. To show how to select the graph terms most representative of these limits, we firstly demonstrate how 1–connections and linear subdigraphs capture all the possible interaction paths of the signal in the sys-

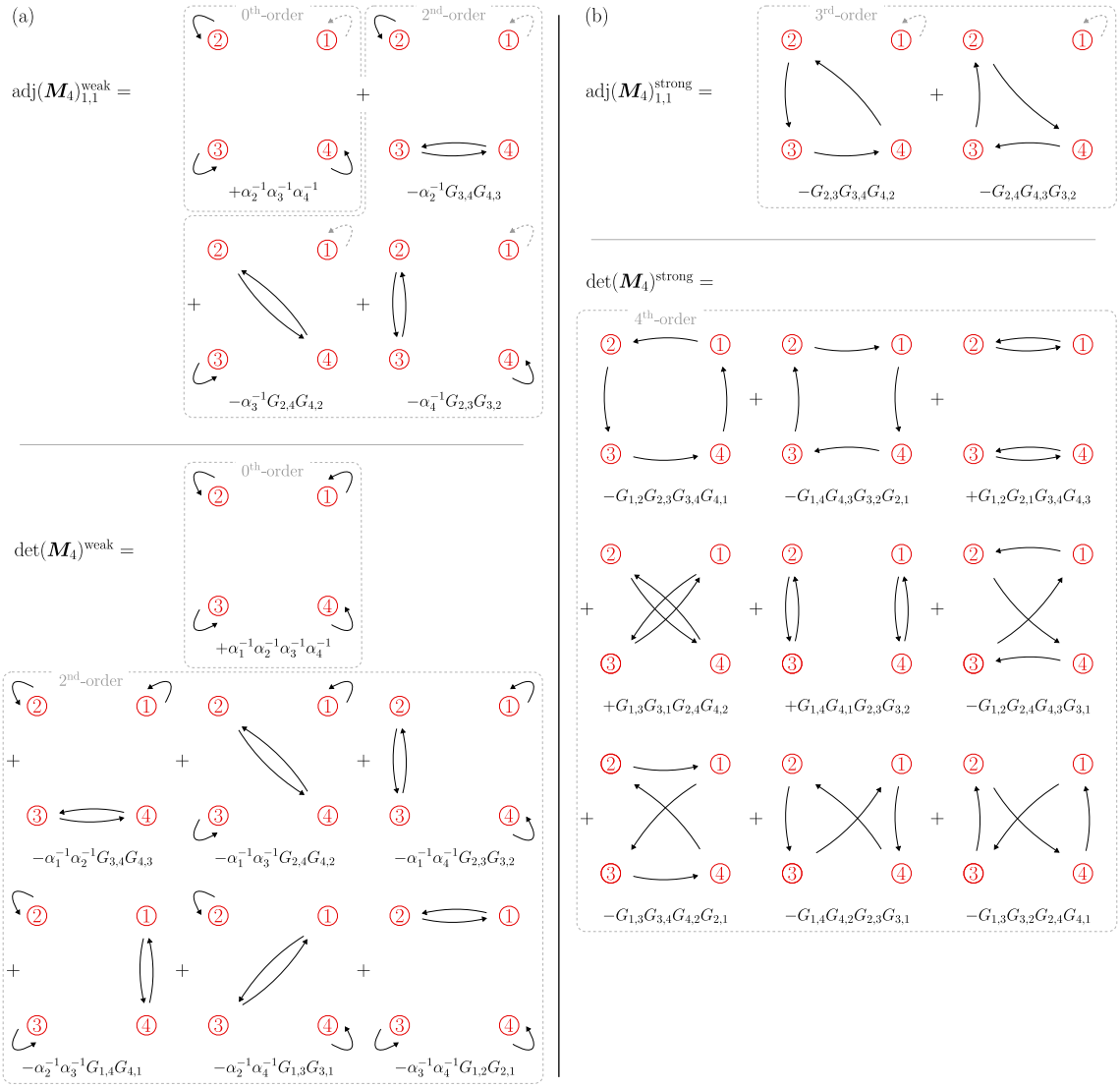

Figure 3: We show an example of construction of the element $(\boldsymbol{M}_4^{-1})_{1,1} = \mathrm{adj}(\boldsymbol{M}_4)_{1,1}/\det(\boldsymbol{M}_4)$ in the weak (panel (a)) and strong (panel (b)) approximations. While the weak approximation accounts for scattering events up to 2^{nd}–order in the interaction ($\propto G^2$), the strong approximation accounts for interactions of 4^{th} ($\propto G^4$) or the highest non–trivial order. The contributions of the single graphs are derived using Eq. (14) for the adjugate and Eq. (13) for the determinant. In the top panels, we show the 1–connections $D^*[1 \to 1]$ obtained by removing the self–loop in vertex 1 from the linear subdigraphs L that include the edge $1 \to 1$. In the bottom panels, we show the linear subdigraphs obtained from the Coates digraph $D^*(\boldsymbol{M}_4)$.

tem. This allow us to identify scattering events of different orders to represent approximations.

As a simple example, we consider a system of two scatterers characterized by polarizabilities α_1 and α_2, symmetrically interacting via the Green's function $G_{1,2}$. Now, we constructively build all the possible paths (or scattering events) of the system. To do this, we evaluate the incident field on the first scatterer, $\phi_{\text{inc}}(\boldsymbol{x}_1)$, while analogous considerations can be done for the second scatterer. The field $\phi_{\text{inc}}(\boldsymbol{x}_1)$ is the sum of all the possible paths starting from the different scatterers of the system and ending in scatterer 1. All these signals are scaled by the polarizability of the scatterer itself, α_1. We start adding the contribution of a signal generated in scatterer 1, $\phi_{\text{inc}}(\boldsymbol{x}_1) = \left[\phi_{\text{s}}(\boldsymbol{x}_1)\alpha_1 + \cdots\right]$, where the first term on the RHS is given by the source field. Proceeding in the same way, a signal propagating from the second scatterer is scaled by the polarizability of the scatterer itself, α_2, then weighted by the interaction $G_{1,2}$ connecting the two scatterers, obtaining $\phi_{\text{inc}}(\boldsymbol{x}_1) = \left[\phi_{\text{s}}(\boldsymbol{x}_1)\alpha_1 + \phi_{\text{s}}(\boldsymbol{x}_2)\alpha_2 G_{1,2}\alpha_1\right]$. While these contributions account for the "one–round trips", the signals can propagate back and forth in the systems. Considering "multiple–round trips", we obtain

$$\begin{aligned}\phi_{\text{inc}}(\boldsymbol{x}_1) = &\left[\phi_{\text{s}}(\boldsymbol{x}_1)\alpha_1 + \phi_{\text{s}}(\boldsymbol{x}_2)\alpha_2 G_{1,2}\alpha_1\right] \\ &\left[1 + \alpha_1\alpha_2 G_{1,2}^2 + (\alpha_1\alpha_2 G_{1,2}^2)^2 + \cdots\right],\end{aligned} \tag{15}$$

where the term in the second square bracket accounts for the paths of different orders and extend to an infinite number of interactions. In the case of $|\alpha_1\alpha_2 G_{1,2}^2| < 1$, this last term can be written using the closed form of the geometric series as

$$\phi_{\text{inc}}(\boldsymbol{x}_1) = \frac{\left[\phi_{\text{s}}(\boldsymbol{x}_1)\alpha_1 + \phi_{\text{s}}(\boldsymbol{x}_2)\alpha_2 G_{1,2}\alpha_1\right]}{1 - \alpha_1\alpha_2 G_{1,2}^2}. \tag{16}$$

This is the analytical solution to Eq. (10) for the incident field $\phi_{\text{inc}}(\boldsymbol{x}_1)$ in the case of a symmetric 2–scatterer system. Note that, in Eq. (16), the terms in the numerator (i.e., the adjugate terms or 1–connections) represent the single scattering events, while the denominator (i.e., the determinant or linear subdigraphs) represent the possible multiple repetitions of the single scattering events. We identify the single scattering events and multiple repetitions by their order in the interaction G. For example, in Eq. (16), the numerator is made of 0^{th} and 1^{st}–order scattering events.

In the same way, the denominator is made of 0^{th}–and 2^{nd}–order multiple repetitions. Proceeding in the same way for an arbitrary number of scatterers, we can build single scattering events and identify paths containing i^{th}–order interactions.

Now, we translate this interpretation of scattering events into the graph theory picture of Sec. 2.5 and we define different regimes of approximation. To do this, as a second example, we consider again the system described by $\boldsymbol{M}_4$. In Fig. 3, we show how to evaluate the term $(\boldsymbol{M}_4)^{-1}_{1,1} = \text{adj}(\boldsymbol{M}_4)_{1,1}/\det(\boldsymbol{M}_4)$ for the weak (panel (a)) and strong (panel (b)) coupling limits. By means of the construction shown above, in the case of weakly interacting scatterers, we restrict the sums in Eqs. (14) and (13) to those 1–connections/linear subdigraphs carrying weights γ up to second order in the interactions G (i.e., up to G^2), similar to the truncation of the Born series to second order [43]. With this approximation, we account for all those scattering processes whose graphs include no more than 2 edges (self–loops excluded), as shown in Fig. 3 panel (a). Approximating both the adjugate terms and the full determinant of the matrix $\boldsymbol{M}_4$, we can evaluate the entries of $\boldsymbol{M}_4^{-1}$, as per Eq. (12).

Unlike the Born series, which typically diverges in the limit of strong scattering, we can also take the limit of very strongly coupled particles, isolating those graphs with the largest number of edges (i.e., the highest non–trivial power of the inter–particle interaction G). Thus, we keep only the highest–order interaction terms of the sum in the adjugate terms and in the full determinant. In Fig. 3 panel (b), we see how these correspond to 1-connections of order $N-1$ for the adjugate and linear subdigraphs of order N for the determinant. Consequently, the most significant scattering event in the case of strongly interacting scatterers is represented by a signal traveling across the entire system and interacting with the highest number of scatterers[2]. Therefore, graph theory allows for a systematic way to calculate the total field $\phi(\boldsymbol{x})$ to any order in the interaction.

This graph interpretation results in a very efficient way of getting a good approximation of the total field $\phi(\boldsymbol{x})$ while only including the dominant scattering events in the weak ($0^{\text{th}}, 1^{\text{st}}, 2^{\text{nd}}$–order) and strong ($N^{\text{th}}, (N-1)^{\text{th}}$–order) cases. We show this in Fig. 4, where we evaluate the average percentage error of the absolute value of the approximated fields $|\phi(\boldsymbol{x})^{\text{weak}}|$ (in panel (a)) and $|\phi(\boldsymbol{x})^{\text{strong}}|$

[2]Note that, although these approximations select a small subset of all the possible scattering processes, their number still increases rapidly with the number of particles N.

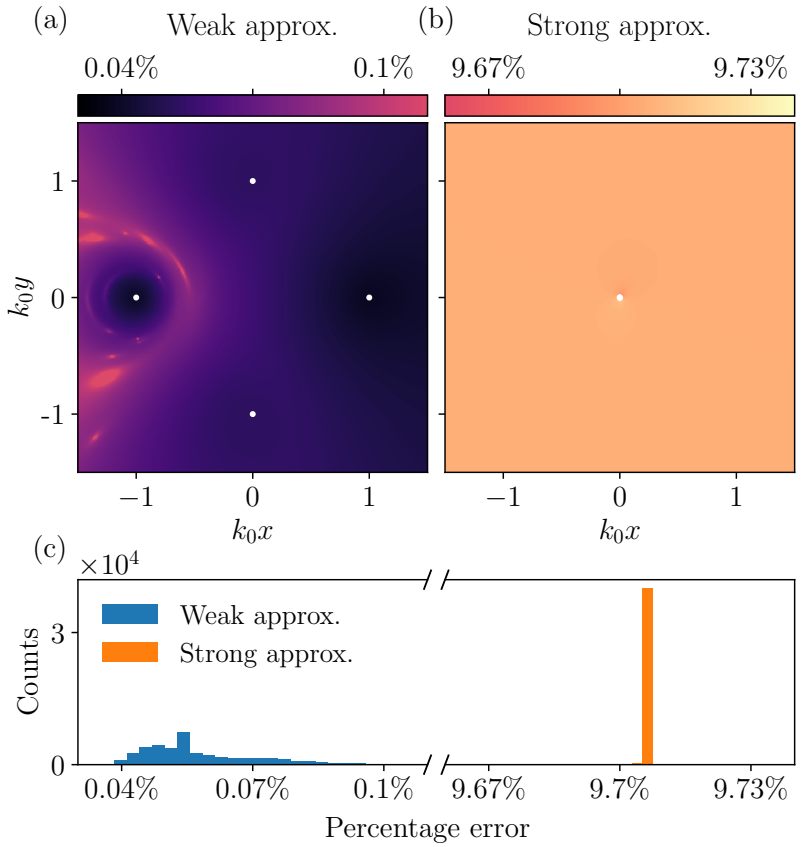

Figure 4: Percentage error of the weak (panel (a)) and strong (panel (b)) coupling approximations of the total field. This is evaluated with respect to the corresponding non–approximated total field obtained using Eq. (12). Since the interaction strengths are determined by the Green's functions, the weak and strong approximations only differ in the inter–scatterer distance, while the remaining parameters are kept unchanged. The error is averaged over 100 setups with random polarizabilities (hence the asymmetric appearance of the plot in panel (a)). The white dots identify the scatterers in the system. Given the small inter–scatterer distance of the strong coupling approximation, in panel (b), the scatterers are represented all on top of each other. In panel (c), while the strong–coupling approximation (orange) maintains a uniform percentage error in space, the weak–coupling approximation (blue) strongly depends on spatial distribution.

(in panel (b)) against the absolute value of the corresponding non–approximated field $|\phi(\boldsymbol{x})|$. The percentage error is averaged over 100 random values of scatterers' polarizations. Note that, in the case of weak coupling, we set $k_0\bar{r} \approx 1$ where $\bar{r}$ is the inter–scatterer distance, while in the case of strong coupling, we set $k_0\bar{r} \ll 1$.

2.7 N–th order exceptional points

An exceptional point (EP) of a system is a non–Hermitian degeneracy in parameter space that emerges whenever two or more eigenvectors coalesce. The order of the EP is determined by the number of coalescing eigenvectors. At the EP, the matrix of the system is not diagonalizable but still admits a Jordan form [44]. In such form, the dimension of the Jordan blocks correspond to the order of the eigenvectors' coalescence, e.g., a 2×2 Jordan block corresponds to a 2^{nd}–order coalescence and so on. Finding these non–Hermitian singularities in small–dimensional systems is straightforward and an analytical solution can be quickly determined. Both 2^{nd}–order and limited higher–order EPs have been thoroughly studied [45, 46, 47] and experimentally realized [21, 48, 49]. However, no consistent method to find N^{th}–order EPs in wave scattering systems has been presented yet. Note that we focus on those EPs with degenerate zero eigenvalue due to their clear physical implications on the total field of the system. In fact, since the total field depends on the inverse of the determinant, these eigenvalues are the cause to its highly degenerate responsiveness to parameter perturbation.

In the following, we use the transpose Frobenius companion matrix and its characteristic polynomial to explore N^{th}–order zero eigenvalue EPs [25] and we interpret the result from a graph theory perspective. Note that, in a similar fashion, companion matrices and N-th order EPs have been recently studied in a tropical geometric framework [50]. We then design an EP in a scattering setting and probe the system's response against parameter perturbations.

2.7.1 EPs conditions

We now consider a system of N scatterers and impose the condition that, at some desired resonant frequency ω_0, the interaction matrix (11) exhibits an N^{th}–order EP whose eigenvalues coalesce to zero. As the outgoing field from the

system depends on the inverse of the interaction matrix, this ought to yield a system whose power output diverges at the design frequency, and yet is also very sensitive to small perturbations (as in [21]), e.g., the scatterer positions.

We first consider the transpose Frobenius companion matrix $\boldsymbol{M}_{\text{Frob}}$ associated with the matrix $\boldsymbol{M}$ of Eq. (11) [51]. The companion matrix is defined such that it generates the same polynomial for the eigenvalues λ of $\boldsymbol{M}$, and is given by

$$\boldsymbol{M}_{\text{Frob}} = \begin{pmatrix} 0 & 1 & 0 & \cdots & 0 & 0 \\ 0 & 0 & 1 & \cdots & 0 & 0 \\ \vdots & \vdots & \vdots & \ddots & \vdots & \vdots \\ 0 & 0 & 0 & \cdots & 1 & 0 \\ 0 & 0 & 0 & \cdots & 0 & 1 \\ -c_0 & -c_1 & -c_2 & \cdots & -c_{N-2} & -c_{N-1} \end{pmatrix}, \tag{17}$$

where the c_i are the coefficients of the powers of λ in the characteristic polynomial,

$$\begin{aligned} 0 &= \det(\lambda \mathbb{1} - \boldsymbol{M}) \\ &= \det(\lambda \mathbb{1} - \boldsymbol{M}_{\text{Frob}}) \\ &= \lambda^N + (-1)^1 c_{N-1} \lambda^{N-1} + \cdots + (-1)^N c_1 \lambda + c_0. \end{aligned} \tag{18}$$

The form of the companion matrix is useful to us as it is closely related to the single $N \times N$ Jordan block matrix, $\boldsymbol{J} = \delta_{i+1,j}$ where $i, j \in [1, N]$,

$$\boldsymbol{J} = \begin{pmatrix} 0 & 1 & 0 & \cdots & 0 & 0 \\ 0 & 0 & 1 & \cdots & 0 & 0 \\ \vdots & \vdots & \vdots & \ddots & \vdots & \vdots \\ 0 & 0 & 0 & \cdots & 1 & 0 \\ 0 & 0 & 0 & \cdots & 0 & 1 \\ 0 & 0 & 0 & \cdots & 0 & 0 \end{pmatrix}. \tag{19}$$

The two matrices (17) and (19) take the same form once all the c_i in (17) are zero. We assume that the interaction matrix $\boldsymbol{M}$ in Eq. (11) differs from (17) by a similarity transformation, an assumption which holds for the cases considered

below. It is, in fact, sufficient for the interaction matrix $\boldsymbol{M}$ to have N distinct roots (in regime of no EPs) for the transformation $\boldsymbol{M}_{\text{Frob}} = \boldsymbol{T}^{-1}\boldsymbol{M}\boldsymbol{T}$ to exist [52]. The transformation matrix $\boldsymbol{T} = \boldsymbol{P}\boldsymbol{Q}^{-1}$ is derived as the product of the non-singular matrix $\boldsymbol{P}$ whose columns are the eigenvectors of $\boldsymbol{M}$ and $\boldsymbol{Q}$ whose columns are made of the set of N eigenvectors of $\boldsymbol{M}_{\text{Frob}}$, $\boldsymbol{q}_i = (1, \lambda_i, \lambda_i^2, \cdots, \lambda_i^{N-1})^T$ relative to its eigenvalues λ_i [53]. [3] For details on the derivation of such transformation $\boldsymbol{T}$ see App. A.2. With this assumption, there is an N^{th}–order non–Hermitian degeneracy in the spectrum of $\boldsymbol{M}$ when all the c_i are zero. By means of this simple requirement, we can engineer a zero eigenvalue EP of desired order by solving the set of non–linear equations given by the conditions $c_i = 0$ for $i = 0, 1, \cdots, N-1$. These coefficients c_i can be evaluated relying on the expansion of the determinant in terms of its minors. Our system of equations for an N^{th}–order EP with zero eigenvalue thus becomes

$$\begin{cases} c_0 = \det(\boldsymbol{M}) = 0 \\ c_1 = \displaystyle\sum_{I_1 \in \mathscr{S}_1([n])} \det\left(\boldsymbol{M}_{(i_1,i_1)}\right) = 0 \\ c_2 = \displaystyle\sum_{I_2 \in \mathscr{S}_2([n])} \det\left(\boldsymbol{M}_{(i_1,i_1),(i_2,i_2)}\right) = 0 \\ \vdots \\ c_{N-1} = \displaystyle\sum_{I_{N-1} \in \mathscr{S}_{N-1}([n])} \det\left(\boldsymbol{M}_{(i_1,i_1),\cdots,(i_{N-1},i_{N-1})}\right) \\ \qquad = \text{Tr}(\boldsymbol{M}) = 0, \end{cases} \tag{20}$$

where I_m is the set of indices $I_m = \{i_1, i_2, \cdots, i_m\}$ defining the minor and $\mathscr{S}_m([n])$ is the collection of size–m combinations within the set $[n] = \{1, 2, \cdots, n\}$. Therefore, $\boldsymbol{M}_{(i,i)}$ is the first minor obtained by removing the i–th row and column, $\boldsymbol{M}_{(i,i),(j,j)}$ is the second minor obtained by removing i–th and j–th rows and columns, and so on. Using this form to construct the coefficients c_i, we numerically evaluate the solution to the non–linear system, identifying the parameters for an N^{th}–order EP.

Importantly, the EP conditions (20) are given in terms of sums of minors of

[3] Note that, in case there is no similarity transformation between the matrix and its Frobenius companion matrix, it is always possible to find lower order EPs given by the block companion matrices Ref. [52].

the interaction matrix, which we have given a graph theoretic interpretation for in Eq. (13) and Eq. (14). For instance, satisfying the final condition in Eq. (20) requires a vanishing sum of the 1×1 minors, which equals the trace of the interaction matrix. From the identification shown in Fig. 2, this condition requires the vanishing sum of the self–interactions in the system. Thus, at a zero eigenvalue N^{th}–order exceptional point, we require (among others) the condition that the inverse polarizabilities α_i^{-1} sum to zero. Since the polarizabilities are complex, both the real and imaginary parts of the α will have to sum to zero, which is only possible in the presence of active scatterers, i.e., scatterers that exhibit gain. Note that, as we will show in Sec. 2.7.3, the active/passive nature of the scatterers is determined by an interplay of real and imaginary parts of the polarizabilities of the scatterers. As a result, in the presence of scatterers with real polarizabilities, a full system of active scatterers is required to find an exceptional point.

Moving up through the conditions (20), from c_{N-1} to c_{N-2} and so on, we see that all the second order interactions within the 2×2 minors must also sum to zero (equivalent to considering the 2×2 interaction matrix for every pair of particles in the system), as must the third order interactions defined within the 3×3 minors and so on. We thus reach the conclusion that an N^{th}–order exceptional point can be associated with N conditions, each requiring the vanishing sum of sub–scattering events between a fixed number of particles. Note that the latter zero trace and determinant conditions found in the scattering matrix are reminiscent of the ones found in the case of systems described by a Hamiltonian with pseudochiral symmetry [25].

In addition to the maximal N^{th}–order EP, we can also find n^{th}–order singularities with $n < N$ by requiring only the first n coefficients c_0, c_1, $\cdots$, c_{n-1} to vanish. This generates a smaller non–linear system whose solution identifies an n^{th}–order EP. This is only possible if n coefficients vanish in ascending order, starting from c_0. In fact, this condition allows one to collect a factor λ^n in the polynomial in Eq. (18), producing an n^{th}–order $\lambda = 0$ solution. This solution corresponds to the $n \times n$ Jordan block relative to the n^{th}–order EP. Any other combination of vanishing coefficients results in a diagonalizable system, without non–Hermitian singularities. Finally, note that the construction of EPs is inevitably dependent on the presence of interaction G in the system. In fact, in the case of no interaction, we would be left with a diagonalizable system.

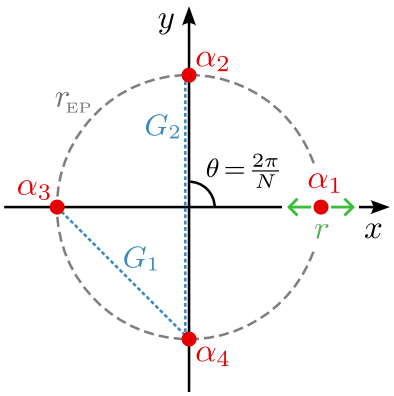

Figure 5: Example construction of a scattering system with an N^{th}–order exceptional point. The system consists of N scatterers (here $N = 4$) with polarizabilities α_n forming a cyclic polygon on a circle with radius r_{EP}. Since the scatterers are equidistantly spaced, the angle θ is uniquely determined by the number of scatterers N, $\theta = 2\pi/N$. The scatterers interact with the nearest neighbors via the Green's function G_1 and with the next–to–nearest neighbors via G_2. When probing the total field and the power output, we use the radial distance of the first scatterer r as the tunable parameter to scan through the exceptional point in parameter space.

2.7.2 Graph theory conditions for EPs

As an example, we now design a scattering configuration exhibiting a 4^{th}–order exceptional point and we interpret the condition of non-Hermitian degeneracy in terms of graphs. In the next subsection, we show how the scattered total field depends on a chosen parameter, in our case, the position of the first scatterer.

For the purpose of simplicity and readability, we now find the parameters (in our case, the polarizabilities α) that satisfy the EP conditions in a system in which the scatterers' positions are fixed. As sketched in Fig. 5, we equidistantly inscribe our scatterer array in a circle of radius r_{EP}, simplifying the interaction matrix such that it contains only $N/2$ different Green's functions G when N is even, and $(N-1)/2$ when N is odd. Given the limited number of Green's functions, this configuration is particularly convenient for an efficient search of the EPs. The

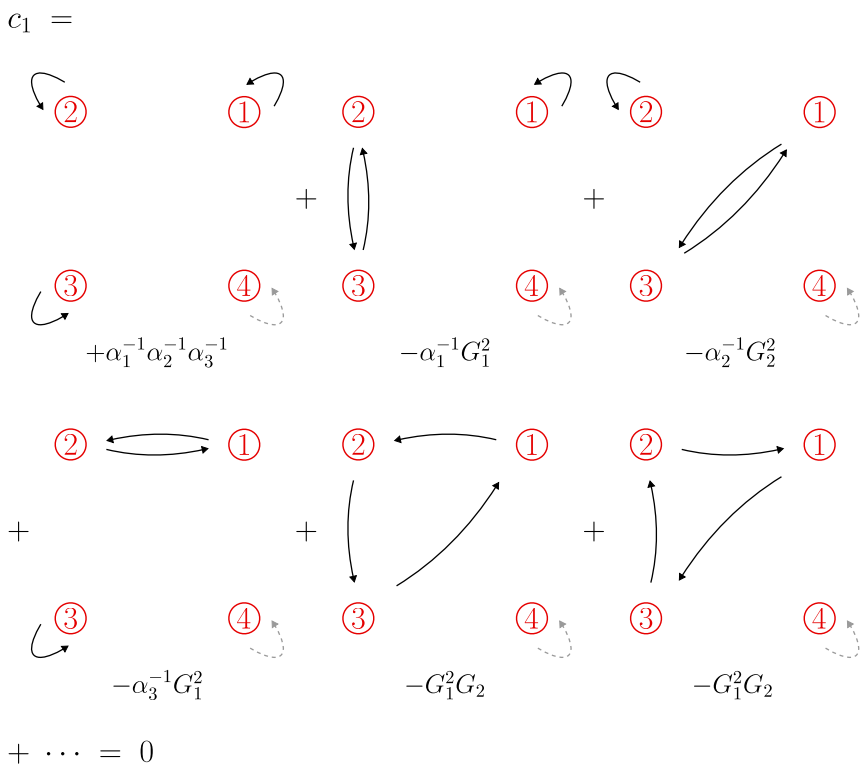

Figure 6: Example construction of the condition $c_1 = 0$ represented by the appropriate 1–connection graphs. The conditions are the graph–theory analogous of the set of non–linear equations in (20) for the interaction matrix $\boldsymbol{M}_{4,\mathrm{sym}}$ relative to Fig. 5. We show only the events $D^*[4 \to 4]$ with the 4^{th} scatterer neglected, however the condition accounts also for three analogous sets of graphs in which the other scatterers are neglected, namely $D^*[1 \to 1]$, $D^*[2 \to 2]$, and $D^*[3 \to 3]$. All the resulting scattering events have to be finally summed together to give the final condition $c_1 = \alpha_1^{-1}\alpha_2^{-1}\alpha_3^{-1} - \alpha_1^{-1}G_1^2 - \alpha_2^{-1}G_2^2 - \alpha_3^{-1}G_1^2 - 2G_1^2G_2 + \cdots = 0$.

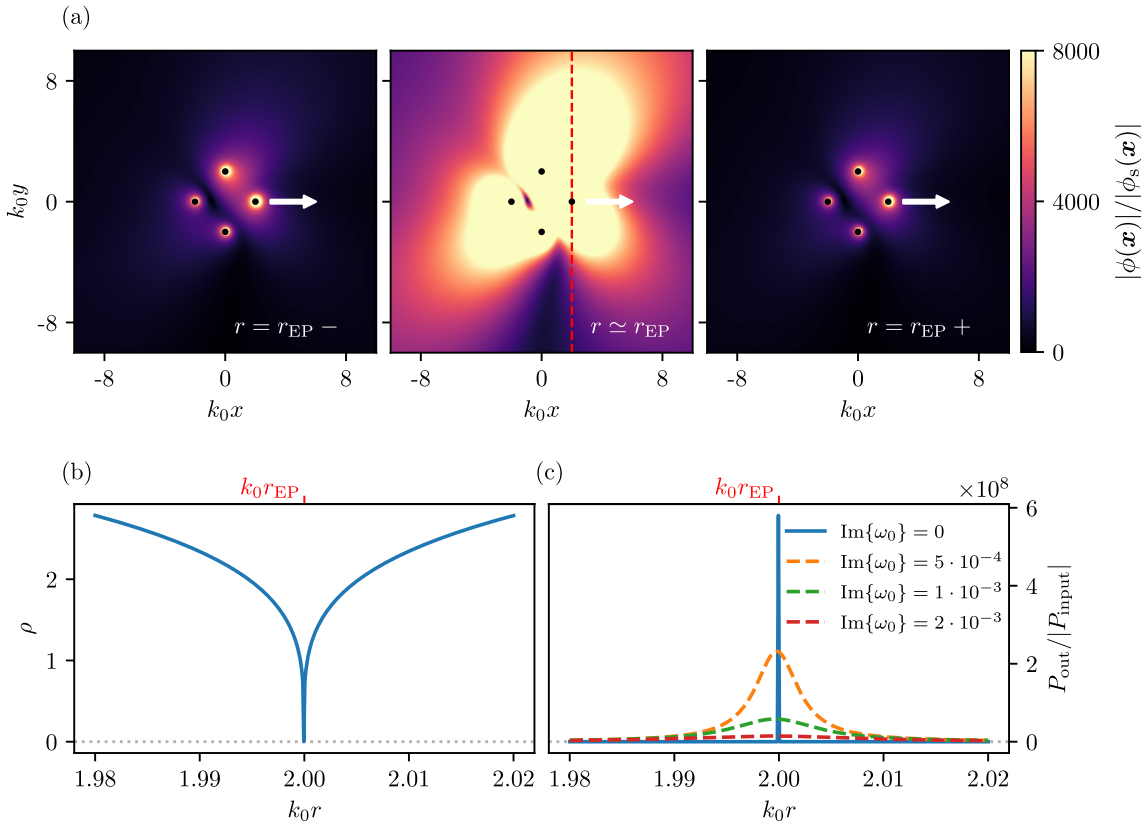

Figure 7: Effects of a 4^{th}–order exceptional point on the total field (panel (a)), global Euclidean distance (panel (b)), and power output (panel (c)) of the system in response to a change in the tuning parameter, that is, the radial distance of the first scatterer r. The latter ranges in $r \in [r_{\mathrm{EP}} - \epsilon k_0^{-1}, r_{\mathrm{EP}} + \epsilon k_0^{-1}]$, where ϵ defines a small deviation from the exceptional point. In panel (a), we show the absolute value of the total field normalized against the source field. In the scan from left to right (indicated by the white arrow), the tunable radial distance r is shifted by the amounts $\epsilon \in \{-10^{-3}, -10^{-5}, +10^{-3}\}$. Note how the total field experiences a sudden peak in the proximity of the EP (middle plot). In panel (b), we show the global Euclidean distance of the right eigenvectors (see Eq. (22)) as a function of the tuning parameter r. This measure goes to zero when $r = r_{\mathrm{EP}}$. At this point, all the right eigenvectors (and corresponding left eigenvectors) merge into a single one. In panel (c), we show the power output (see Eq. (23)) with respect to the tunable parameter r for different purely imaginary shifts of the resonant frequency, $\mathrm{Im}\{\omega_0\} \in \{0, 5 \cdot 10^{-4}, 1 \cdot 10^{-3}, 2 \cdot 10^{-3}\}$. For increasing imaginary shifts, the power response of the system broadens while the peak power at the EP reduces. Note that, given the general high gain of the system determined by the polarizabilities, the baseline power output remains of order 10^7 even for significant shifts from the ideal EP condition.

interaction matrix associated with these cyclic polygons of scattering particles is,

$$\boldsymbol{M}_{\mathrm{sym}} = \begin{pmatrix} \alpha_1^{-1} & -G_1 & -G_2 & \cdots & -G_2 & -G_1 \\ -G_1 & \alpha_2^{-1} & -G_1 & \cdots & -G_3 & -G_2 \\ -G_2 & -G_1 & \alpha_3^{-1} & \cdots & -G_4 & -G_3 \\ \vdots & \vdots & \vdots & \ddots & \vdots & \vdots \\ -G_2 & -G_3 & -G_4 & \cdots & \alpha_{N-1}^{-1} & -G_1 \\ -G_1 & -G_2 & -G_3 & \cdots & -G_1 & \alpha_N^{-1} \end{pmatrix}, \tag{21}$$

where G_1 represents the nearest–neighbor interactions, G_2 represents the next–to–nearest–neighbor interactions, and so on. The angle between two consecutive scatterers is $\theta = 2\pi/N$. In the figure, we also represent the tunable parameter, that is, the radial distance of the first scatterer r. While this parameter is not used to find the EP condition of Eq. (21) (it would indeed change the periodic–chain–like structure of the matrix in Eq. (21)), it will be needed later for the numerical analysis on the system's sensitivity to parameter perturbations.

Our system is described by the 4×4 matrix $\boldsymbol{M}_{4,\mathrm{sym}}$ with $G_1 = G(\boldsymbol{x}_1, \boldsymbol{x}_2) = G(\boldsymbol{x}_1, \boldsymbol{x}_4) = G(\boldsymbol{x}_2, \boldsymbol{x}_3) = G(\boldsymbol{x}_3, \boldsymbol{x}_4)$ and $G_2 = G(\boldsymbol{x}_1, \boldsymbol{x}_3) = G(\boldsymbol{x}_2, \boldsymbol{x}_4)$. The Frobenius companion matrix of $\boldsymbol{M}_{4,\mathrm{sym}}$ takes the form of Eq. (17) restricted to the space of 4×4 matrices, therefore including only the coefficients c_i with $i \in \{0, 1, 2, 3\}$. These coefficients can be evaluated using the determinants in Eq. (20).

Our graph theory description previously introduced illustrates the meaning of this set of vanishing sums. For example, in Fig. 6, we show the condition $c_1 = 0$ which requires all the 3^{rd}–order scattering events to sum to zero. It is worth recalling that the zero condition of the i^{th}–order coefficient is entirely independent of scattering events of any other order. This means that asking for the single coefficient c_i to be zero is equivalent to asking for all the scattering events of order $N - i$ to sum to zero. Thus, to find a 4^{th}–order EP, we need the condition $c_i = 0$ to be satisfied by the scattering events of *every* order, that is, $c_i = 0$ for $i = 0, 1, 2, 3$.

We finally note that, while a graph can be associated to the matrix of eigenvectors of the system, we could not find any particular interpretation to the coalescence of multiple eigenvectors in terms of graphs. Moreover, in the case of EPs of non–trivial order, a mathematical expression for the eigenvectors becomes highly

cumbersome and strongly dependent on the system described. The non–trivial problem of finding a general expression for the eigenvectors of high–order EPs and an associated graph theoretic interpretation is left for further studies.

2.7.3 Trading sensitivity for dissipation balance

In Sec. 2.7.2, we gave an example of a convenient system to find a 4^{th}–order EP. On this system, we interpreted the condition to find such EPs from a graph theory perspective. We now show how the presence of this high–order EP affects the total field of the system with respect to perturbations to the chosen parameter. In our case, this parameter is the position of the first scatterer r as depicted in Fig. 5.

In Fig. 7 panel (b), we show the coalescence of the eigenvectors in the range of parameter $r \in [r_{\text{EP}} - \epsilon k_0^{-1}, r_{\text{EP}} + \epsilon k_0^{-1}]$ with $\epsilon = 0.02$ by means of the vanishing total Euclidean distance. This distance is defined as

$$\rho \coloneqq \sum_{\substack{i=1 \\ j=i+1}}^{N} ||\boldsymbol{v}_i - \boldsymbol{v}_j||, \tag{22}$$

where $\boldsymbol{v}_i$ and $\boldsymbol{v}_j$ are the right eigenvectors of the matrix $\boldsymbol{M}_{4,\text{sym}}$ and the sum takes care of not double–counting terms. This quantity vanishes when $r = r_{\text{EP}}$, signaling the coalescence of all the N eigenvectors relative to the degenerate eigenvalue 0. This is the N^{th}–order exceptional point. Note that, given the high–order nature of the exceptional point, known EP measures like the phase rigidity of the eigenvectors and the condition number of the eigenvector matrix do not entirely capture the features of the singularity [54]. Note also that while the distance in Eq. 22 serves as an intuitive quantity to witness full eigenvector degeneracy, it is unable to give insight on the eigenvector scaling around the EPs. To do so, one can still access the phase rigidity's critical exponent [55, 56]. The immediate effects of the EP on the total field are shown in Fig. 7 panel (a). In this figure, we scan, from left to right, through the EP with the tunable parameter r. In proximity of the EP, the absolute value of the total field $|\phi(\boldsymbol{x})|$ rapidly increases before attenuating again, once the singularity is passed.

In the same way, we can probe the EP just obtained by measuring the power

output of our system of scatterers (see Fig. 5), which we define as

$$P_{\text{out}} \coloneqq \oint_{\text{S}} \text{Im}\{\phi(\boldsymbol{x})^* \nabla\phi(\boldsymbol{x})\} \cdot \hat{n}\, \text{d}s \tag{23}$$
$$= -\sum_{\substack{n=1 \\ n\neq m}}^{N} \text{Im}\{\alpha_n\} |\phi_{\text{inc}}(\boldsymbol{x}_n)|^2.$$

Eq. (23) is derived, after little manipulation, by integrating the LHS of Eq. (7) (multiplied from the left by the complex conjugate field $\phi(\boldsymbol{x})^*$) in a volume surrounding all the scatterers. We obtain the closed surface integral in Eq. (23) by means of the divergence theorem.

The power output, as written in Eq. (23), depends on the sum of the incident fields on the different scatterers of the system weighted by the imaginary parts of the polarizabilities. In our case, the entire dependence of the power response on the tuning parameter r is contained in the incident field. This is uniquely determined by the matrix $\boldsymbol{M}_{\text{sym}}$. It is common to express the sensitivity (in our case, in the form of power output) of the system at the EPs in terms of a perturbation to the system matrix [21, 57]. Thus, to express the power output in Puiseux series, one would need to rederive the scattering matrix in terms of a perturbation around the EP as for example $\boldsymbol{M}_{\text{sym}} = \boldsymbol{J} + \varepsilon \boldsymbol{M}'$ where $\boldsymbol{J}$ is the full Jordan matrix (19) and $\boldsymbol{M}'$ is a non trivial perturbation matrix [25]. Doing so, if the perturbation around the EP lifts the coefficient c_{N-1} such that $c_{N-1} \neq 0$, the Puiseux series $\lambda = \lambda_0 + \sum_{i=1}^{\infty} \varepsilon^{i/N} \lambda_i$ exists and refers to the N^{th}–order EP. However, in case the perturbation leaves $c_{N-1} = 0$, the perturbed eigenvalues split in k different cycles of order n_k of the form $\lambda_k = \lambda_0 + \sum_{i=1}^{\infty} \varepsilon^{i/n_k} \lambda_{k,i}$ with the various $n_k < N$ summing to N as $\sum_k n_k = N$ [25, 45, 58]. Note that, in the case of the system described in Eq. (21), a perturbation in the radial distance r indeed lifts the coefficient c_{N-1} such that $c_{N-1} \neq 0$.

Given the high order of the exceptional point, the power output of the system shows extreme sensitivity to perturbations in parameter space. In Fig. 7 panel (c), we show the power output of Eq. (23) versus the tunable parameter r for different imaginary offsets of the resonant frequency ω_0 at which the EP is found.

The introduction of an imaginary part in the design frequency has multiple functions. On the one hand, it helps to understand how possible experimental inaccuracies can affect peak and shape of the power output of the system. On the

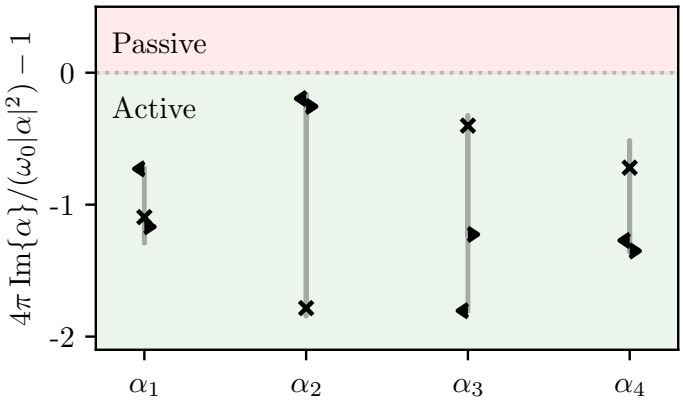

Figure 8: Results of the inequality in Eq. (24) for the polarizabilities α. The polarizabilities are the solutions to the EP conditions (20) of the system described by $\boldsymbol{M}_{4,\mathrm{sym}}$ and shown in Fig. 5. The solid lines are all the possible solutions of polarizabilities for a scan in the imaginary part of the resonant frequency, $\mathrm{Im}\{\omega_0\} \in [-1, 1]$. This has been done in a similar fashion to Ref. [18]. The "cross" marker indicates $\mathrm{Im}\{\omega_0\} = 0$ while the "left–caret" and "right–caret" indicate the end of the imaginary ranges, $\mathrm{Im}\{\omega_0\} = -1$ and $\mathrm{Im}\{\omega_0\} = 1$, respectively. The scattering elements are passive when the α lay on the positive semi–plane (red semi–plane), therefore they satisfy the inequality. In the figure, all the solutions α of the system considered are active, therefore laying on the negative semi–plane (green semi–plane). The figure shows how imaginary shifts in the resonant frequency ω_0 used to design the EP allows one to tune the distribution of the gain/loss of the system across the scatterers.

other hand, it shows how "ad–hoc" imaginary shifts in the design frequency of the system can help to adjust the distribution of gain/loss across the scatterers. Since the system is then probed with real frequencies ω_0, introducing an imaginary shift in the design frequency results in a quasi–coalescence of the eigenvectors causing a drop in the system responsiveness to the singularity. This is shown in the figure by means of the amplitude reduction and broadening of the power output curves when increasing the imaginary shift of ω_0. Note that the curve with $\mathrm{Im}\{\omega_0\} = 0$ (solid blue curve in the figure), which is set to cross the EP, is re–scaled by a factor 10^{-26} in order to fit into the graph and give some insight of the power output behavior.

We now show how we can tune the distribution of the gain/loss of the system across the scatterers in order to finely adjust possible experimental setups, where it is preferred to have a set of scatterers with the least possible gain. The presence of exceptional points inevitably depends on the scatterers' structure and, in particular, on their active nature. The condition for a scatterer j to be passive is

that its polarizability α_j satisfies the inequality [59]

$$\mathrm{Im}\{\alpha_j\} > \frac{k_0}{4\pi}|\alpha_j|^2, \tag{24}$$

obtained by asking for a negative divergence of the power output in the case of passive scatterers. Eq. (24) is derived for the case of 3D Green's function as considered in this section. As a reminder, $k_0 = \omega_0/c$ with $c = 1$ in this section. If the polarizabilty of a scatterer satisfies this inequality, the scatterer acts as a passive, lossy medium. As we have seen in Eq. (20), one requirement to obtain an N^{th}–order EP is $\mathrm{Tr}(\boldsymbol{M}) = 0$, i.e., all the scattering events of 0–th order have to sum to 0 while individually being non–vanishing. This implies having active elements in the system, i.e., scatterers with $\mathrm{Im}\{\alpha\} < 0$ which cannot satisfy Eq. (24). On the other hand, elements with $\mathrm{Im}\{\alpha\} > 0$ do not necessarily satisfy Eq. (24), thus, are not necessarily passive. By means of this inequality, we define a polarizability regime in which energy has to be injected into the system to obtain these N^{th}–order EPs.

In Fig. 8, we show this inequality test for the polarizabilities of the system described by $\boldsymbol{M}_{4,\mathrm{sym}}$. In this case, none of the polarizabilities satisfy the inequality (no polarizabilities lie on the positive half of the plane), indicating that no passive scatterers are found in the system [4]. The test consists of a scan in the imaginary shift range $\mathrm{Im}\{\omega_0\} \in [-1, 1]$, where ω_0 is the resonant frequency at which the EP is evaluated. The "cross" marker indicates $\mathrm{Im}\{\omega_0\} = 0$ while the "left–caret" and "right–caret" indicate the end of the imaginary ranges, $\mathrm{Im}\{\omega_0\} = -1$ and $\mathrm{Im}\{\omega_0\} = 1$, respectively. The semi–transparent lines represent all the intermediate α's solutions found in this range.

Note that, we already implemented this imaginary–shifted resonant frequency in order to control the spectral width of the scattering resonance of the system (see panel (c) of Fig. 7). However, in this case, one can use the imaginary shift to move the gain/loss bias on different scatterers. Therefore, an imaginary shift in the design resonant frequency allows one to fine tune the dissipation balance of the system in exchange of a broadening of the power output with respect to the EP parameter. This fine tuning capability becomes crucial in experimental setups

[4] Using our numerics, we found polarizabilities satisfying the inequality (24) in 7–scatterer systems described by the matrix (21).

that aim for the least possible gain in their set of scatterers.

2.8 Conclusion

In this section, we used graph theory to solve wave scattering problems within the discrete dipole approximation (DDA).

Firstly, we showed how to use graph theory to develop a diagrammatic method for understanding multiple scattering processes. These processes are encoded in the inverse of the interaction matrix used to find the analytical total field of the system. We interpreted single scattering events in terms of 1–connections and linear subdigraphs and used these to approximate weakly and strongly coupled systems. This is a convenient machinery to calculate the total field $\phi(\boldsymbol{x})$ when the dimensionality of the system makes finding a full analytical solution impractical.

Secondly, by exploiting the Frobenius companion matrix associated with the system, we developed a systematic procedure to find N^{th}–order zero eigenvalue exceptional points (EPs). The EPs are found by making vanish the sum of the 1–connections associated with scattering events of the same order. At a zero eigenvalue EP, the scattering becomes singular, causing the divergence of the emitted power. In our example, the perturbation coincided with a single–particle displacement from the EP configuration of the order of $1/100$ of a wavelength. Although such a sharp sensitivity is achieved in position basis, one could describe the system in terms of the directions of input and output waves. Note that, as shown in this section, one can also generate n^{th}–order zero eigenvalue EPs where $n < N$. This might be useful to trade part of the scattered field sensitivity with a reduced number of conditions in the non–linear system. This further reduces the requirement for gain, crucial in certain experimental settings. The generation of N^{th}–order zero eigenvalue EPs can be of particular interest for coherent perfect absorption (CPA) structures [60, 61]. Here, the signature of the zero eigenvalue EPs (referred to as CPA EPs) is a quartic behavior of the absorption line shape in the perfectly absorbed channel. In addition, we believe the graph theoretical approach to be a promising tool to describe EPs associated with PT symmetry breaking in scattering systems [62, 63] and the non-Hermitian skin effect in the case of non–reciprocal 1D chains of scatterers [64, 65, 66].

Finally, to control the spectral width of the exceptional points, we explored

the consequences of displacing the design resonant frequency into the complex plane. We found that it is possible to trade the required gain/loss of the single scatterers with a broadened response. This would allow one to choose the preferred dissipation balance throughout the array of elements at the expenses of a reduction in the power output of the system. It might be possible to explore this trade–off as well as the entirety of multiple scattering physics in programmable metamaterials such as those demonstrated by Cho et al. [18].

Software package

The Julia package developed for solving the wave scattering problems found in this section is available at https://github.com/mekise/graph-theory-dda.

3 Local master equations bypass the secular approximation

3.1 Statement of contribution

In the following work, I devised the idea to study exceptional points in the regime of open quantum systems. I did all the calculations to obtain the master equations' expressions, exceptional point conditions, and transformations. I have built the code, generated the results, and written the paper. The latter with a strong contribution by Luis Correa. Luis Correa also devised the idea to look for key dissimilarities between local and global master equations.

3.2 Summary

Master equations are a vital tool to model heat flow through nanoscale thermodynamic systems. Most practical devices are made up of interacting sub-systems and are often modelled using either *local* master equations (LMEs) or *global* master equations (GMEs). While the limiting cases in which either the LME or the GME breaks down are well understood, there exists a 'grey area' in which both equations capture steady-state heat currents reliably but predict very different *transient* heat flows. In such cases, which one should we trust? Here we show that, when it comes to dynamics, the local approach can be more reliable than the global one for weakly interacting open quantum systems. This is due to the fact that the *secular approximation*, which underpins the GME, can destroy key dynamical features. To illustrate this, we consider a minimal transport setup and show that its LME displays *exceptional points* (EPs). These singularities have been observed in a superconducting-circuit realisation of the model [67]. However, in stark contrast to experimental evidence, no EPs appear within the global approach. We then show that the EPs are a feature built into the Redfield equation, which is more accurate than the LME and the GME. Finally, we show that the local approach emerges as the weak-interaction limit of the Redfield equation, and that it entirely avoids the secular approximation.

3.3 Introduction

Master equations and quantum thermodynamics go hand in hand. The former have become essential tools to make sense of the 'thermodynamics' of quantum systems. But, conversely, the early works on quantum thermodynamics [68, 69, 70] focused on the study of the mathematical properties of master equations. Nowadays the field is evolving very rapidly [71], and quantum heat devices are making the transition from theory to experiments on a wide range of platforms, including trapped ions, solid-state systems, atomic gases, single-electron systems, nanoscale thermoelectrics, and superconducting circuits [72, 73, 74, 75, 76, 77, 78, 79, 80].

The Gorini–Kossakowski–Sudarshan–Lindblad (GKSL) quantum master equation [81, 82] makes it easy to draw parallels between the dissipative dynamics of a single open quantum system and the thermodynamics of macroscopic devices [83, 84, 85]. Namely, these equations can be derived from first principles in the limit of weak system–environment coupling, and may lead to *thermal equilibrium* [86]. We shall refer to such 'thermalising' GKSL equations as *global master equations* (GMEs). Furthermore, heat currents can be formally defined such that they obey the second law of (classical) thermodynamics [68, 83]. However, the underlying assumptions of the global master equation require a clean timescale separation [87], which may break down for, e.g., small multipartite quantum-thermodynamic devices that interact *weakly* among them (see, e.g.,[88, 89]) and large many-body open quantum systems [90].

Alternatively, in multipartite open quantum systems, master equations have often been built heuristically by 'adding up' GKSL terms (cf. Fig. 9). These are referred-to as *local master equations* (LMEs). While such equations do comply, by construction, with the minimum expectation of generating a completely positive dynamics, they have been criticised for their thermodynamic deficiencies [88, 91, 92, 93, 94, 95, 96, 97, 98, 99, 100, 101, 102]. Namely, unlike global master equations, LMEs fail to bring systems to thermal equilibrium, even in the limit of weak system–environment interactions [95, 98]. When applied to quantum heat devices, they entirely miss crucial physics, such as heat leaks and internal dissipation [92, 103]. They may even predict flagrant violations of the Second Law of thermodynamics, in the form of cold-to-hot stationary heat flows [93]. Surpris-

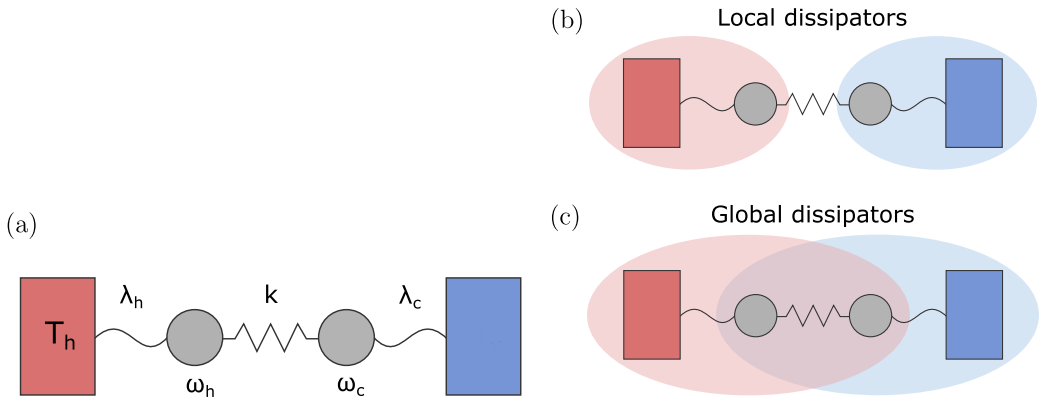

Figure 9: **Example system and local/global pictures.** Two resonators of frequencies ω_h and ω_c are coupled linearly with strength k, and connected weakly with dissipation strengths λ_h and λ_c to two independent thermal reservoirs at temperatures, T_h and T_c, respectively (panel (a)). Heat thus flows through the resonators. The key difference between the local (panel (b)) and the global (panel (c)) master equations is illustrated by the shaded regions that indicate the scope of the hot and cold dissipators, respectively.

ingly, however, the LME does prove very accurate in some cases—even more accurate than the GME [88, 89]. The aim of this section is to understand *when* and *why*. Using the most suitable master equation in each situation (see Fig. 9) can make a crucial difference when studying the thermodynamics of any nanoscale heat device.

Local master equations may be understood as a rough approximation to the true dissipative dynamics, valid in the limit of weak interactions between the subsystems. Starting from a microscopic model this may be shown in two closely related ways—either by carefully introducing a coarse-graining in the time-evolution of the open system [104, 105, 106, 107, 108, 109, 110, 111, 112], or by truncating a perturbative expansion of the master equation in the internal coupling strength [113, 114].

The disagreement between the steady-state thermodynamic predictions of GME and LME had been illustrated before [89, 94, 115]. Here, we put the spotlight on situations in which they agree in the steady state, but differ during the transient dynamics. In such cases, which master equation is correct? One that is thermodynamically sound (GME), or a truncated series expansion with limited validity and serious thermodynamic deficiencies (LME)? Strikingly, our answer is that *we should always trust the latter* within its error bars, which assume weak internal couplings. This holds for any multipartite quantum heat device which uses

frequency filters to couple to the environment [116], e.g., a qubit or a harmonic oscillator.

For illustration, we focus on the specific model of two coupled resonators that connect two thermal reservoirs. We find that the LME exhibits a family of *exceptional points* [117] (EPs) in its dynamics, while the corresponding GME does not. Yet, EPs have indeed been found experimentally in a superconducting circuit described by the same model [67]. In addition, at weak internal couplings, the transient heat currents obtained from the LME agree with the much more accurate Redfield equation [118] while *not* with the global approach. The reason for the failures of the GME is that it is underpinned by the (somewhat crude) secular approximation, which misses relevant physics. In contrast, the LME can be obtained directly from the Redfield equation, bypassing the secular approximation. Our results thus add much needed clarity to the long-standing 'local-versus-global' debate, and explain various previously reported features of both the global and the local approach.

This section is structured as follows: We begin by giving an overview of open-system dynamics within the global and local approach in Sec. 3.4 and then, describing the details of the example model in Sec. 3.5. In Sec. 3.6 we introduce the concept of *exceptional points* and discuss how to search for them, given the equations of motion of a linear open quantum system. We then illustrate the different exceptional-point structure in parameter space according to the local, global, and Redfield approaches (Sec. 3.7). Finally, in Sec. 3.7.4, we show that, at resonance, the local approach succeeds at capturing the correct heat-flow dynamics, while the global master equation fails. In Sec. 3.8 we summarise and conclude.

3.4 Open-system dynamics

3.4.1 The global master equation

The Hamiltonian of a *generic* multipartite open system connected to various independent bosonic heat baths reads

$$\boldsymbol{H} = \boldsymbol{H}_S + \boldsymbol{H}_B + \boldsymbol{H}_{SB}, \tag{25}$$

where $\boldsymbol{H}_S$ is the Hamiltonian of the system, $\boldsymbol{H}_B$ the Hamiltonian of the baths, each made of infinitely many uncoupled harmonic oscillators, and $\boldsymbol{H}_{SB}$ stands for the interaction between system and baths. Specifically, let

$$\boldsymbol{H}_S = \sum\nolimits_i \boldsymbol{H}_i^{(\mathrm{loc})} + k\boldsymbol{V}, \tag{26}$$

where $\boldsymbol{H}_i^{(\mathrm{loc})}$ is the local Hamiltonian of each sub-system and $\boldsymbol{V}$ denotes the interactions between them. Possibly incurring in some redundancy, we will indicate the sub-system Hamiltonians with the superscript "(loc)" in the hope for clarity when comparing the global with the local approach. The parameter k controls the magnitude of the latter. Every sub-system couples to its own independent bath, i.e.

$$\boldsymbol{H}_{SB} = \sum\nolimits_\alpha \lambda_\alpha \boldsymbol{S}_\alpha \otimes \boldsymbol{B}_\alpha, \tag{27}$$

where $\boldsymbol{B}_\alpha$ is a generic bath operator and $\boldsymbol{S}_\alpha$ is a system operator which does not commute with $\boldsymbol{H}_S$, thus allowing for energy *dissipation* as well as *decoherence*. Here, λ_α controls the strength of the interaction with bath α.

The effective equation of motion for any arbitrary system observable $\boldsymbol{O}$ can be cast in the standard GKSL form [81, 82]. Although its microscopic derivation is textbook material [87], we provide it in Appendix B.1, making as few assumptions as possible. Essentially, these are:

(i) that the dissipation strengths are small,

(ii) that system and bath start uncorrelated,

(iii) that the bath correlation functions are short-lived,

(iv) and that there is a clear-cut timescale separation between (fast) coherent and (slow) dissipative processes.

The so-called (partial) Redfield equation [118] (cf. Appendix B.1) follows from these assumptions,

$$\frac{\mathrm{d}\boldsymbol{O}}{\mathrm{d}t} = i[\boldsymbol{H}_S, \boldsymbol{O}] + \sum\nolimits_\alpha \mathscr{R}_\alpha^\dagger(\boldsymbol{O}) + \mathcal{O}(\lambda_\alpha^3). \tag{28}$$

The super-operator $\mathscr{R}_\alpha^\dagger(\boldsymbol{O})$ associated to bath α is given by

$$\mathscr{R}_\alpha^\dagger(\boldsymbol{O}) = \frac{1}{2}\sum_{\omega_i\times\omega_j<0}\gamma_{\omega_i}^{(\alpha)}\left(\boldsymbol{A}_{\omega_i}^{(\alpha)\dagger}\boldsymbol{O}\boldsymbol{A}_{\omega_j}^{(\alpha)} - \boldsymbol{A}_{\omega_j}^{(\alpha)}\boldsymbol{A}_{\omega_i}^{(\alpha)\dagger}\boldsymbol{O}\right) + \text{h.c.} \tag{29}$$

where the summation $\omega_i \times \omega_j < 0$ runs over the frequencies ω_i and ω_j of all *open decay channels* [87] with different sign. The decay rates $\gamma_\omega^{(\alpha)}$ are

$$\gamma_\omega^{(\alpha)} = 2\,\lambda_\alpha^2\,\mathrm{Re}\int_0^\infty \mathrm{d}s\, e^{i\omega s}\,\langle \boldsymbol{B}_\alpha(s)\boldsymbol{B}_\alpha(0)\rangle, \tag{30}$$

where the notation $\langle\cdot\rangle$ indicates thermal averaging at temperature T_α. Finally, $\boldsymbol{A}_\omega^{(\alpha)}$ is the 'jump' operator of the decay channel at frequency ω from bath α. These satisfy

$$[\boldsymbol{H}_S, \boldsymbol{A}_\omega^{(\alpha)}] = -\omega\,\boldsymbol{A}_\omega^{(\alpha)}, \tag{31a}$$

$$\boldsymbol{S}_\alpha = \sum\nolimits_\omega \boldsymbol{A}_\omega^{(\alpha)}, \tag{31b}$$

$$\boldsymbol{A}_\omega^{(\alpha)\,\dagger} = \boldsymbol{A}_{-\omega}^{(\alpha)}. \tag{31c}$$

In particular, Eq. (30) implies that $\mathscr{R}_\alpha^\dagger$ is $\mathcal{O}(\lambda_\alpha^2)$. Note as well that, to make sense of (28) and all the following adjoint master equations, we must always take expectation values, as we do in Eqs. (57), (70a) and (72a).

Pushing (iv) to its last consequences justifies the (full) *secular approximation*, and allows to bring Eq. (28) to the simpler GKSL form,

$$\frac{\mathrm{d}\boldsymbol{O}}{\mathrm{d}t} = i[\boldsymbol{H}_S, \boldsymbol{O}] + \sum\nolimits_\alpha \mathscr{G}_\alpha^\dagger(\boldsymbol{O}) + \mathcal{O}(\lambda_\alpha^3), \tag{32}$$

where the super-operators $\mathscr{G}_\alpha^\dagger(\boldsymbol{O})$ are given by

$$\mathscr{G}_\alpha^\dagger(\boldsymbol{O}) = \sum\nolimits_\omega \gamma_\omega^{(\alpha)}\left(\boldsymbol{A}_\omega^{(\alpha)\,\dagger}\boldsymbol{O}\boldsymbol{A}_\omega^{(\alpha)} - \frac{1}{2}\{\boldsymbol{A}_\omega^{(\alpha)\,\dagger}\boldsymbol{A}_\omega^{(\alpha)}, \boldsymbol{O}\}_+\right). \tag{33}$$

Here, $\{\cdot,\cdot\}_+$ stands for the anti-commutator. Eq. (32) is a *global* master equation. The name tag highlights the fact that the $\boldsymbol{A}_\omega^{(\alpha)}$ enable jumps between eigenstates of the full multipartite $\boldsymbol{H}_S$, rather than between states of each sub-system $\boldsymbol{H}_\alpha^{(\mathrm{loc})}$ (see Fig. 9).

Since full diagonalisation of $\boldsymbol{H}_S$ is needed to construct these jump operators, setting up Eq. (32) may become computationally unworkable; especially,

when one wishes to scale up a many-body open quantum system. Furthermore, the GME suffers from another important issue, especially when applied to systems with a *dense* energy spectrum. In such cases, assumption (iv) from the list above is likely to break down [90], which could invalidate the GME's predictions [88, 89, 119]. On the 'plus side', constructing jump operators that fulfil Eqs. (31) is guaranteed to bring the system into a state of thermodynamic equilibrium whenever all temperatures coincide, i.e., $T_\alpha = T\ \forall\alpha$. This is analogous to the Zeroth Law of thermodynamics [120]. Since, in addition, the dynamical map resulting from (32) is *completely positive* [69], it can be shown that

$$\sum\nolimits_\alpha \frac{\dot{\mathcal{Q}}_\alpha}{T_\alpha} \leq 0, \tag{34a}$$

$$\text{for}\quad \dot{\mathcal{Q}}_\alpha \coloneqq \langle \mathscr{G}_\alpha^\dagger(\boldsymbol{H}_S)\rangle_\infty, \tag{34b}$$

where the steady-state heat currents $\dot{\mathcal{Q}}_\alpha$ account for the stationary rate of energy influx from bath α (i.e., $\langle\cdot\rangle_\infty$ denotes here *stationary* average). Eq. (34) is interpreted as the Second Law of thermodynamics, since it is formally identical to the statement of Clausius' theorem [68, 83]. Therefore, the global GKSL equation is particularly well suited to study the thermodynamics of (weakly dissipative) open quantum systems.

3.4.2 The local master equation

Another type of quantum master equation may be built by simply *adding up* dissipators that act locally on a specific part of the system

$$\frac{\mathrm{d}\boldsymbol{O}}{\mathrm{d}t} = i[\boldsymbol{H}_S, \boldsymbol{O}] + \sum\nolimits_\alpha \mathscr{L}_\alpha^\dagger(\boldsymbol{O}), \tag{35}$$

where $\mathscr{L}_\alpha^\dagger(\boldsymbol{O})$ takes the form

$$\mathscr{L}_\alpha^\dagger(\boldsymbol{O}) = \sum\nolimits_{\omega'} \gamma_{\omega'}^{(\alpha)} \left(\boldsymbol{L}_{\omega'}^{(\alpha)\,\dagger} \boldsymbol{O} \boldsymbol{L}_{\omega'}^{(\alpha)} - \frac{1}{2}\{\boldsymbol{L}_{\omega'}^{(\alpha)\,\dagger}\boldsymbol{L}_{\omega'}^{(\alpha)}, \boldsymbol{O}\}_+ \right). \tag{36}$$

Here, the non-hermitian operators $\boldsymbol{L}_{\omega'}^{(\alpha)}$ have the properties,

$$[\boldsymbol{H}_{\alpha}^{(\mathrm{loc})}, \boldsymbol{L}_{\omega'}^{(\alpha)}] = -\omega' \boldsymbol{L}_{\omega'}^{(\alpha)}, \tag{37a}$$

$$\boldsymbol{S}_{\alpha} = \sum\nolimits_{\omega'} \boldsymbol{L}_{\omega'}^{(\alpha)}, \tag{37b}$$

$$\boldsymbol{L}_{\omega'}^{(\alpha)\,\dagger} = \boldsymbol{L}_{-\omega'}^{(\alpha)}. \tag{37c}$$

in place of Eqs. (31). Note that the sum does not run over the Bohr frequencies ω of $\boldsymbol{H}_S$, but over those of $\sum_\alpha \boldsymbol{H}_\alpha^{(\mathrm{loc})}$; hence the notation ω'.

Such local equation is easily *scalable*, as the resonators must be diagonalised individually when searching for the operators $\boldsymbol{L}_{\omega'}^{(\alpha)}$. It also shares with the global master equation its GKSL form, which means that the resulting dynamics is, again, completely positive.

'Completely positive' is often equated identically to 'physical' because at least it produces positive probabilities. We remark, however, that (completely positive) LMEs violate the Zeroth Law by construction [95]. Indeed, due to Eq. (37a), the dissipators $\mathscr{L}_\alpha^\dagger$ 'try' to pull the system towards the local thermal state $\propto \exp\Big\{(-\sum_\alpha \boldsymbol{H}_\alpha^{(\mathrm{loc})}/T_\alpha)\Big\}$, which does not commute with the full $\boldsymbol{H}_S$ appearing in the 'coherent-evolution' term of Eq. (35). Hence, according to the LME, the system would never thermalise, even if all temperatures T_α are identical. As a result, also the Second Law as stated in Eq. (34), may be violated. In fact, in our example model of Eq. (39), the local approach invariably predicts unphysical cold-to-hot heat currents whenever $\omega_c/T_c < \omega_h/T_h$ [93]. This, however, would cease to be an issue if the environments were *active*, i.e., able to exchange both heat and work with the system [121].

3.4.3 Comparing local and global approach

A local master equation can be motivated physically beyond merely "adding up dissipators". For instance, we may obtain the LME directly from a formal collisional model, in the limit of instantaneous collisions [122, 123]. However, in this case, the thermodynamics of the LME needs to be reassessed to account for the 'cost' of those collisions with bath 'units' [121, 124]. On the other hand, for microscopic Hamiltonian models, the general Markovian weak-coupling master equation can be simplified by *coarse-graining* over a relevant time-scale [104,

105, 106, 107, 108, 109, 110, 111, 112]. Depending on how this averaging is done, both the LME and the GME can emerge naturally [105, 106].

The LME (35) can be alternatively viewed as the lowest order in an expansion of the GME (32) [113, 114]. Namely, applying perturbation theory to the eigenstates and eigenvalues of $\boldsymbol{H}_S$ for small k and following the procedure to obtain a GME [87, 113], gives

$$\mathscr{G}_\alpha^\dagger = \mathscr{G}_\alpha^{\dagger\,(0)} + k\,\mathscr{G}_\alpha^{\dagger\,(1)} + k^2\,\mathscr{G}_\alpha^{\dagger\,(2)} + \cdots . \tag{38}$$

Whenever $\mathscr{G}_\alpha^{\dagger\,(0)} = \mathscr{L}_\alpha^\dagger$, one can claim that the LME becomes equivalent to truncating the expansion at zeroth order in k. Since all terms $\mathscr{G}^{\dagger\,(n)}$ are $\mathcal{O}(\lambda^2)$, the LME would thus be accurate within $k\lambda^2$-sized 'error bars'. If k is weak enough, this may be acceptable when compared with the intrinsic error of the GME, set at $\mathcal{O}(\lambda^3)$ (cf. Eq. (32)). In light of this interpretation, the unphysical cold-to-hot heat flows predicted by the local approach may be thought-of as a mere artifact of the truncated expansion [113].

However, if the degeneracy of $\boldsymbol{H}_S$ changes depending on whether $k = 0$ or $k \neq 0$, the zeroth order of the global dissipator does not coincide with the local one (i.e., $\mathscr{G}_\alpha^{\dagger\,(0)} \neq \mathscr{L}_\alpha^\dagger$) [113]. As we will see, this is precisely what happens to our example model (39) when $\omega_c = \omega_h = \omega$ [88, 89, 105, 125]. Instead, we find that it is the zeroth order of the *Redfield* dissipator that coincides with the local one (i.e., $\mathscr{R}_\alpha^{\dagger\,(0)} = \mathscr{L}_\alpha^\dagger$) [105].

3.5 The system

The system considered in what follows is sketched in Fig. 9. It is comprised of two coupled resonators with frequencies ω_c and ω_h, which we model as

$$\boldsymbol{H}_S = \sum\nolimits_{\alpha\in\{c,h\}} \left(\frac{1}{2}\omega_\alpha^2 \boldsymbol{x}_\alpha^2 + \frac{\boldsymbol{p}_\alpha^2}{2}\right) + k\,\boldsymbol{x}_c\,\boldsymbol{x}_h \tag{39}$$

where $\boldsymbol{x}_\alpha$ and $\boldsymbol{p}_\alpha$ are the corresponding quadratures, and k denotes the inter-resonator coupling strength. We also set the masses to $m_\alpha = 1$. From now on, we work in units of $\hbar = k_B = 1$. This model can describe the two capacitively coupled superconducting resonators studied experimentally in Ref. [67] in search

for exceptional points[5].

Each resonator is weakly connected to a local heat bath $\alpha \in \{c, h\}$ ('c' for cold and 'h' for hot) with equilibrium temperatures $T_c < T_h$. The resonator–bath couplings are

$$\boldsymbol{H}_{SB} = \lambda_c \boldsymbol{x}_c \otimes \boldsymbol{B}_c + \lambda_h \boldsymbol{x}_h \otimes \boldsymbol{B}_h, \tag{40}$$

where the bath operators $\boldsymbol{B}_\alpha$ are

$$\boldsymbol{B}_\alpha = \sum\nolimits_\nu g_\nu^{(\alpha)} \mathbf{q}_\nu^{(\alpha)}, \tag{41}$$

and $\mathbf{q}_\nu^{(\alpha)}$ stands for the coordinate of the environmental mode of bath α at frequency ω_ν. Note that $\boldsymbol{H}_{SB}$ is linear in the dissipation strengths λ_h and λ_c. The couplings $g_\nu^{(\alpha)}$ can be collected into the *spectral densities*

$$J_\alpha(\omega) := \pi \lambda_\alpha^2 \sum\nolimits_\nu \frac{g_\nu^{(\alpha)\,2}}{2\omega_\nu} \delta(\omega - \omega_\nu), \tag{42}$$

where $\delta(\omega - \omega_\nu)$ stand for Dirac deltas. In the following we will work with the standard Ohmic–algebraic spectral densities

$$J_\alpha(\omega) = \lambda_\alpha^2 \, \omega \frac{\Lambda^2}{\omega^2 + \Lambda^2} \tag{43}$$

with $\alpha \in \{c, h\}$. Here, the phenomenological parameter Λ sets an 'ultraviolet' cut-off on the spectrum of the bath. We note that the precise analytical form of the spectral density does not play an active role in our problem, as long as Λ is large when compared with all other relevant energy scales. Given the spectral densities, the decay rates $\gamma_\omega^{(\alpha)}$ of Eq. (30) take the form,

$$\gamma_\omega^{(\alpha)} = 2 J_\alpha(\omega) \left(1 + \frac{1}{e^{\omega/T_\alpha} - 1} \right). \tag{44}$$

[5]More precisely, the Hamiltonian considered in the analysis of the experiment, i.e.,

$$\boldsymbol{H}'_S = \omega_c \boldsymbol{a}_c^\dagger \boldsymbol{a}_c + \omega_h \boldsymbol{a}_h^\dagger \boldsymbol{a}_h + \kappa (\boldsymbol{a}_c^\dagger \boldsymbol{a}_h + \boldsymbol{a}_c \boldsymbol{a}_h^\dagger),$$

follows directly from our Eq. (39) after performing the *rotating-wave approximation* (also referred-to as pre-tracing secular approximation [126]), discarding the zero-point energy terms, and defining $k := 2\kappa\sqrt{\omega_c \, \omega_h}$. Since we focus on the resonant case $\omega_h = \omega_c$, using either $\boldsymbol{H}_S$ or $\boldsymbol{H}'_S$ does not make any difference, as we have verified.

3.6 Exceptional points

We now formally introduce the concept of exceptional points (EPs), before drawing the link to open-system dynamics. EPs are branch-point singularities which appear under variation of parameters of non-Hermitian matrices, such as those describing the dynamics of quantum dissipative systems. EPs have been used as resource for applications such as sensitivity amplification in micro-resonators [127, 128], laser-mode selectivity [129], and topological chirality [130, 131]. More recently, a gain in signal-to-noise-ratio has been shown in EP sensors [132] highlighting the practical relevance of exceptional points.

3.6.1 Formal definition and witnesses

Let $\mathsf{M}(k) \in \mathbb{C}^{N\times N}$ be an $N \times N$ matrix dependent on some parameter (or set of parameters) k. We denote the right eigenvectors of this matrix by $\{|v_j\rangle\}_{j=1,\cdots,N}$; i.e.,

$$\mathsf{M}(k)\,|v_j\rangle = \mu_j\,|v_j\rangle\,. \tag{45}$$

The corresponding *left* eigenvectors $\{(v_j|\}_{j=1,\cdots,N}$ are defined instead by

$$\mathsf{M}(k)^{\mathsf{T}}(v_j|^\dagger = \mu_j(v_j|^\dagger. \tag{46}$$

Notice that $(v_j|^\dagger$ is a *column* vector (like $|v_j\rangle$) due to the Hermitian conjugation. These two indexed families of vectors form a *bi-orthogonal* set [133]; that is,

$$\begin{aligned}(v_i|v_j\rangle &= 0 \quad \text{for } i \neq j,\\ (v_i|v_i\rangle &\leq 1,\end{aligned} \tag{47}$$

with $(v_i|v_i\rangle = 1$ being fulfilled only if $\mathsf{M}(k)$ is Hermitian. Note that, in general, $(v_i|v_i\rangle$ can be negative. We say that the matrix $\mathsf{M}(k)$ has an exceptional point for those parameter choices k resulting in $(v_i|v_i\rangle = 0$ for two or more of the indices $i \in \{1,\cdots,N\}$. This phenomenon is called *self-orthogonality* and it is the hallmark of the coalescence of two or more right eigenvectors [134].

In order to locate the exceptional points of $\mathsf{M}(k)$ we could search for zeros of the *phase rigidities* $\phi_i(k) \coloneqq |(v_i|v_i\rangle|$ for $i \in \{1,\cdots,N\}$ as a function of k. However, analysing the behaviour of every single eigenvector can be time-consuming for

large N. Luckily, we shall only be interested in finding *where* in parameter space an EP of $\mathsf{M}(k)$ is located, and not in *which* or *how many* eigenvectors coalesce. We can thus exploit the fact that, at an EP, the set $\{|v_i\rangle\}_{i=1,\cdots,N}$ does not form a complete basis. Therefore, the matrix $\mathsf{V}_k = (|v_1\rangle, \cdots, |v_N\rangle)$ features a singularity and the norm of its inverse diverges. Consequently, the *condition number* of V_k, denoted $\kappa(\mathsf{V}_k)$, could be a suitable witness for an EP. Namely,

$$\kappa(\mathsf{V}_k) \coloneqq \|\mathsf{V}_k\| \, \|\mathsf{V}_k^{-1}\|, \tag{48}$$

where the operator norm $\|\cdot\|$ is defined as

$$\|\mathsf{O}\| \coloneqq \max_{\mathsf{x}} \frac{\|\mathsf{O}\,\mathsf{x}\|_p}{\|\mathsf{x}\|_p}, \tag{49}$$

x is an arbitrary non-zero vector, and $\|\cdot\|_p$ stands for the p-norm

$$\|\mathsf{x}\|_p \coloneqq \big(\sum\nolimits_i |\mathsf{x}_i|^p\big)^{1/p}. \tag{50}$$

Here, the parameter p could take on any real value $p \geq 1$. In our numerical calculations, we use the 2-norm. Regardless of p, $\kappa(\mathsf{V}_k)$ diverges *iff* there is an EP at position k in parameter space. Also, note that $\|\mathsf{V}_k^{-1}\|$ can be alternatively cast as $\|\mathsf{V}_k^{-1}\| = \max_{\mathsf{x}} \|\mathsf{x}\| / \|\mathsf{V}_k\,\mathsf{x}\|$, which resolves the issue of inverting a singular matrix.

3.6.2 EPs in open quantum systems

In many cases of practical interest, an open system may be fully described by choosing a set of observables $\boldsymbol{\vartheta} = (\vartheta_1, \cdots, \vartheta_m)^{\mathsf{T}}$ and applying the corresponding *adjoint* quantum master equation to each of them; i.e.,

$$\frac{\mathrm{d}\vartheta_i}{\mathrm{d}t} = i[\boldsymbol{H}_S, \vartheta_i] + \sum\nolimits_\alpha \mathscr{D}_\alpha^\dagger(\vartheta_i), \tag{51}$$

where the dissipators $\mathscr{D}_\alpha^\dagger$ can take, e.g., the global $\mathscr{G}_\alpha^\dagger$, local $\mathscr{L}_\alpha^\dagger$, or Redfield $\mathscr{R}_\alpha^\dagger$ form (cf. (33), (36), and (B.15)).

The aim is to pick observables ϑ_j so that (51) becomes a *closed* set of equa-

tions [135]. This can then be expressed in compact form as

$$\frac{\mathrm{d}\langle \boldsymbol{\theta} \rangle}{\mathrm{d}t} = \mathsf{M}_{\mathscr{D}} \langle \boldsymbol{\theta} \rangle, \tag{52}$$

were the resulting matrix of coefficients $\mathsf{M}_{\mathscr{D}} \in \mathbb{C}^{m \times m}$ is generally non-Hermitian. At an EP, $\mathsf{M}_{\mathscr{D}}$ stops being diagonalizable, which has a detectable impact on the dynamics and thermodynamics of the open system [135, 136, 137]. Practical examples of which are the exploitation of the fastest channels of dissipation for superconducting qubits resetting [67] and an enhanced sensitivity of optical microcavities [128].

Specifically, in continuous-variable settings with linear $\boldsymbol{H}_S$—as our example model—it is always possible to write a set of equations like (52). For instance, we can build a 14-element $\boldsymbol{\theta}$ by grouping the four position and momentum operators

$$\mathbf{q} \coloneqq (\boldsymbol{x}_h, \boldsymbol{p}_h, \boldsymbol{x}_c, \boldsymbol{p}_c)^{\mathsf{T}}, \tag{53}$$

together with the 10 distinct combinations

$$\mathbf{C}_{ij} \coloneqq \frac{1}{2}\{\mathbf{q}_i, \mathbf{q}_j\}_+, \tag{54}$$

e.g., $\mathbf{C}_{33} = \boldsymbol{x}_c^2$, $\mathbf{C}_{12} = \mathbf{C}_{21} = \frac{1}{2}\{\boldsymbol{x}_h, \boldsymbol{p}_h\}_+$, or $\mathbf{C}_{32} = \mathbf{C}_{23} = \boldsymbol{x}_c \boldsymbol{p}_h$. Note that other choices of $\boldsymbol{\theta}$ are possible. Ordering the observables so that $\boldsymbol{x}_h$, $\boldsymbol{p}_h$, $\boldsymbol{x}_c$, and $\boldsymbol{p}_c$ are the first elements of $\boldsymbol{\theta}$ results in the 14×14 coefficient matrix $\mathsf{M}_{\mathscr{D}}$

$$\mathsf{M}_{\mathscr{D}} = \left(\begin{array}{c|c} \mathsf{M}_{\mathscr{D},1} & 0 \\ \hline 0 & \mathsf{M}_{\mathscr{D},2} \end{array}\right). \tag{55}$$

That is, for the Hamiltonian $\boldsymbol{H}_S$, one finds that $\mathsf{M}_{\mathscr{D}}$ is the direct sum of sub-matrices $\mathsf{M}_{\mathscr{D},1} \in \mathbb{C}^{4\times 4}$ and $\mathsf{M}_{\mathscr{D},2} \in \mathbb{C}^{10\times 10}$. Looking back at Eq. (52), we thus see that the dynamics of the first-order moments $\langle \mathbf{q}_i \rangle$ decouples from that of the second-order moments $\langle \mathbf{C}_{ij} \rangle$. Note that the same block-diagonal structure is found for the local ($\mathscr{L}$), the global ($\mathscr{G}$), and Redfield ($\mathscr{R}$) equations. Since the exceptional points are properties of the dissipator [137], it seems reasonable that their signatures appear both in $\mathsf{M}_{\mathscr{D},1}$ and $\mathsf{M}_{\mathscr{D},2}$. In Sec. 3.7 below, we focus on the appearance of EPs in the sub-matrices $\mathsf{M}_{\mathscr{D},1}$ while the discussion about $\mathsf{M}_{\mathscr{D},2}$ has

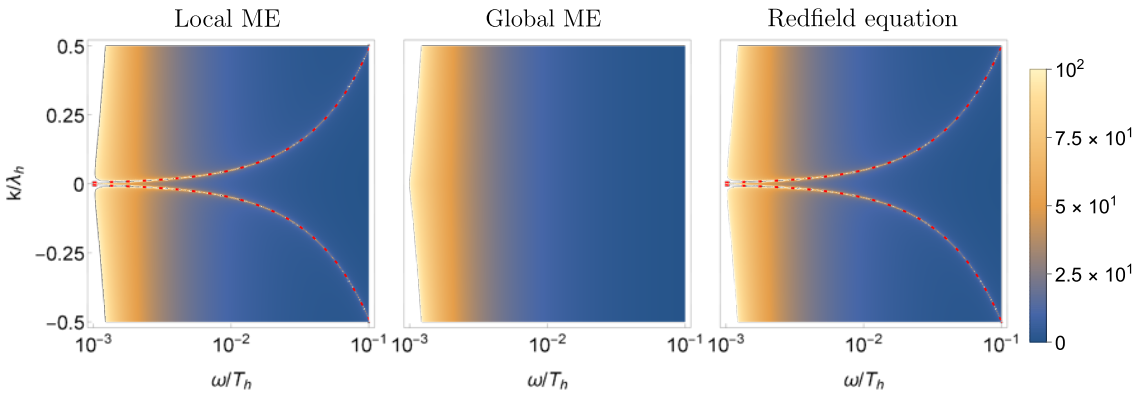

Figure 10: **EPs in the dynamics of first-order moments.** Condition number κ (cf. (48)) of the matrix of eigenvectors of $\mathrm{M}_{\mathscr{L},1}$ **(left)**, $\mathrm{M}_{\mathscr{G},1}$ **(centre)**, and $\mathrm{M}_{\mathscr{R},1}$ **(right)**, as a function of the frequency of the resonators $\omega_h = \omega_c = \omega$ and the strength of their capacitive coupling k (see Eqs. (58), (70b), and (72b)). These are the coefficient matrices of the equations of motion for the first-order moments $\langle \mathbf{q} \rangle$ of the coupled-resonator system, according to the local, global, and Redfield master equation, respectively. A diverging condition number is the distinct signature of an exceptional point. The EPs predicted by the Redfield equation (right) are lost as a result of the secular approximation and thus, entirely missed by the global approach (middle). They are, however, captured by the local master equation (left). Note that the EPs appear exactly along the 'exceptional lines' (61), superimposed in dashed red. The parameters chosen are $T_h = 10$, $T_c = 5$, $\lambda_h^2 = 10^{-8}$, $\lambda_c^2 = 10^{-4}$, and $\Lambda = 10^3$ ($\hbar = k_B = 1$).

been deferred to Appendix B.2.

3.7 Results and discussion

3.7.1 Local master equation

In order to obtain the equations of motion for the first-order moments $\langle \mathbf{q} \rangle$ of the system according to the LME, we need to know the Bohr frequencies involved, and the corresponding jump operators. From now on, we work in the regime of resonant oscillators, i.e. $\omega_h = \omega_c = \omega$, which is a necessary condition for the appearance of the exceptional points in the example model considered, as shown in Appendix B.3.

The Bohr frequencies in Eq. (36) thus become $\{\omega'\} = \{\pm\omega\}$, and the local jump operators of (37a) become

$$\boldsymbol{L}_{\omega}^{(\alpha)} = \frac{\boldsymbol{a}_\alpha}{\sqrt{2\omega}}, \tag{56}$$

where we call $\boldsymbol{L}_{-\omega}^{(\alpha)} = \boldsymbol{L}_{\omega}^{(\alpha)\dagger}$ and $\boldsymbol{a}_\alpha$ is an annihilation operator, so that $\boldsymbol{x}_\alpha = \boldsymbol{L}_{\omega}^{(\alpha)} +$

$\boldsymbol{L}_{-\omega}^{(\alpha)} = (\boldsymbol{a}_\alpha + \boldsymbol{a}_\alpha^\dagger)/\sqrt{2\omega}$. Replacing these into the LME (36) gives

$$\frac{\mathrm{d}\langle \mathbf{q} \rangle}{\mathrm{d}t} = \mathsf{M}_{\mathscr{L},1} \langle \mathbf{q} \rangle, \tag{57}$$

with local coefficient matrix $\mathsf{M}_{\mathscr{L},1}$

$$\mathsf{M}_{\mathscr{L},1} = \frac{1}{2} \begin{pmatrix} \Delta_\omega^{(h)} & 2 & 0 & 0 \\ -2\omega^2 & \Delta_\omega^{(h)} & -2k & 0 \\ 0 & 0 & \Delta_\omega^{(c)} & 2 \\ -2k & 0 & -2\omega^2 & \Delta_\omega^{(c)} \end{pmatrix}, \tag{58}$$

where we have introduced the notation

$$\Delta_\omega^{(\alpha)} := \frac{\gamma_{-\omega}^{(\alpha)} - \gamma_\omega^{(\alpha)}}{2\omega}. \tag{59}$$

Since $\mathsf{M}_{\mathscr{L},1}$ is simple enough, one can obtain an analytic expression for the exceptional points in parameter space. Looking at its eigenvalues, we see that degeneracy appears, provided that

$$4k^2 - \left(\Delta_\omega^{(h)} - \Delta_\omega^{(c)}\right)^2 \omega^2 = 0 \implies k = \pm \frac{\omega}{2} \left|\Delta_\omega^{(h)} - \Delta_\omega^{(c)}\right|. \tag{60}$$

Further replacing the expressions of the decay rates $\gamma_{\pm\omega}^{(\alpha)}$ into the coefficients Δ_α for our choice of spectral density (cf. Eqs. (43) and (44)) results in the remarkably simple expression

$$k = \pm \frac{\omega}{2} \left|\lambda_h^2 - \lambda_c^2\right|. \tag{61}$$

Resorting now to the condition number of the eigenvector matrix of $\mathsf{M}_{\mathscr{L},1}$, we confirm that whole family of exceptional points does lie along (61) (see leftmost panel Fig. 10). That is, adjusting resonance frequency and internal couplings, it is always possible to tune the system into an EP. Interestingly, for exceptional points to appear in this system, dissipation must be asymmetric and the oscillators *resonant* (see Appendix B.3). Note as well that, at resonance, the LME cannot give rise to unphysical cold-to-hot heat currents [93]. Moreover, in a recent experiment with coupled superconducting resonators, signatures of precisely the EPs in (61) have been indeed detected [67].

3.7.2 Global master equation

In order to find the jump operators $\boldsymbol{A}_{\omega}^{(\alpha)}$ within the global dissipators $\mathscr{G}_{\alpha}^{\dagger}$ (cf. (33) and Eqs. (31)), we must rotate our system into its normal-mode quadratures $\mathbf{Q} = (\boldsymbol{\eta}_1, \boldsymbol{\Pi}_1, \boldsymbol{\eta}_2, \boldsymbol{\Pi}_2)^{\mathsf{T}}$, so that

$$\boldsymbol{H}_S = \sum_{j=1}^{2} \left(\frac{\boldsymbol{\Pi}_j^2}{2} + \frac{1}{2}\Omega_j^2 \boldsymbol{\eta}_j^2 \right). \tag{62}$$

At resonance, the orthogonal transformation $(\boldsymbol{x}_h, \boldsymbol{x}_c)^{\mathsf{T}} = \mathsf{P}\,(\boldsymbol{\eta}_1, \boldsymbol{\eta}_2)^{\mathsf{T}}$ between local and global modes has the form

$$\mathsf{P} = \frac{1}{\sqrt{2}} \begin{pmatrix} 1 & 1 \\ 1 & -1 \end{pmatrix}, \tag{63}$$

and the normal-mode frequencies are

$$\Omega_{1,2} = \sqrt{\omega^2 \pm k}. \tag{64}$$

We must decompose the system's coupling operators $\boldsymbol{x}_\alpha$ (cf. Eq. (40)) in eigenoperators of $\boldsymbol{H}_S$. Taking, for instance, $\boldsymbol{x}_h$, one can see that

$$\boldsymbol{x}_h = \frac{\boldsymbol{\eta}_1 + \boldsymbol{\eta}_2}{\sqrt{2}} = \frac{\boldsymbol{b}_1}{2\sqrt{\Omega_1}} + \frac{\boldsymbol{b}_2}{2\sqrt{\Omega_2}} + \text{h.c.}, \tag{65}$$

where $\boldsymbol{b}_j$ is the annihilation operator associated with $\boldsymbol{\eta}_j$. Hence,

$$\boldsymbol{A}_{\Omega_j}^{(h)} = \frac{\mathsf{P}_{1j}}{\sqrt{2\Omega_j}}\,\boldsymbol{b}_j = \frac{\mathsf{P}_{1j}}{2}\left(\boldsymbol{\eta}_j + \frac{i}{\Omega_j}\,\boldsymbol{\Pi}_j\right), \tag{66}$$

$$\boldsymbol{A}_{\Omega_j}^{(c)} = \frac{\mathsf{P}_{2j}}{\sqrt{2\Omega_j}}\,\boldsymbol{b}_j = \frac{\mathsf{P}_{2j}}{2}\left(\boldsymbol{\eta}_j + \frac{i}{\Omega_j}\,\boldsymbol{\Pi}_j\right). \tag{67}$$

Also note that, unlike in the local approach, now there are two open decay channels into each bath, at frequencies Ω_1 and Ω_2, respectively.

We can obtain the equations of motion for the normal-mode variables $\langle \mathbf{Q} \rangle$ from (33);

namely,

$$\frac{\mathrm{d}\langle \mathbf{Q} \rangle}{\mathrm{d}t} = \mathsf{M}'_{\mathscr{G},1} \langle \mathbf{Q} \rangle,$$
$$\mathsf{M}'_{\mathscr{G},1} = \bigoplus_{j=1}^{2} \begin{pmatrix} \tilde{\Delta}_j/2 & 1 \\ -\Omega_j^2 & \tilde{\Delta}_j/2 \end{pmatrix}, \tag{68}$$

where we have introduced the new coefficients

$$\tilde{\Delta}_j \coloneqq \frac{1}{2} \sum\nolimits_{\alpha} \Delta_{\Omega_j}^{(\alpha)}. \tag{69}$$

For completeness, we can rotate Eq. (68) back to the original coordinates $\mathbf{q}$, which gives

$$\frac{\mathrm{d}\langle \mathbf{q} \rangle}{\mathrm{d}t} = \mathsf{M}_{\mathscr{G},1} \langle \mathbf{q} \rangle, \tag{70a}$$
$$\mathsf{M}_{\mathscr{G},1} = \frac{1}{2} \begin{pmatrix} \frac{1}{2}(\tilde{\Delta}_1 + \tilde{\Delta}_2) & 2 & \frac{1}{2}(\tilde{\Delta}_1 - \tilde{\Delta}_2) & 0 \\ -2\omega^2 & \frac{1}{2}(\tilde{\Delta}_1 + \tilde{\Delta}_2) & -2k & \frac{1}{2}(\tilde{\Delta}_1 - \tilde{\Delta}_2) \\ \frac{1}{2}(\tilde{\Delta}_1 - \tilde{\Delta}_2) & 0 & \frac{1}{2}(\tilde{\Delta}_1 + \tilde{\Delta}_2) & 2 \\ -2k & \frac{1}{2}(\tilde{\Delta}_1 - \tilde{\Delta}_2) & -2\omega^2 & \frac{1}{2}(\tilde{\Delta}_1 + \tilde{\Delta}_2) \end{pmatrix}. \tag{70b}$$

The coefficient matrices $\mathsf{M}'_{\mathscr{G},1}$ and $\mathsf{M}_{\mathscr{G},1}$ have the same condition number κ, since they are connected via an orthogonal transformation. As a result, they also have the same EPs, since the norms involved in the calculation of κ remain unaffected (see Eq. (48)).

As seen in the middle panel of Fig. 10, the 'exceptional lines' of diverging condition number in the frequency–coupling space *disappear completely*, according to the global master equation.

One may question the *validity* of the GME for such parameters. Namely, in Fig. 10 we set $k \sim \lambda_\alpha^2$ whereas, to be on the safe side when it comes to the secular approximation, we should ensure instead that $k \gg \max_\alpha \lambda_\alpha^2$ [88]. However, as we show in Sec. 3.7.4, the GME does lead to the correct steady-state properties at all plotted points save for the fringe $|k| \lessapprox 0.1\,\lambda_h^2$. Hence the disappearance of the EPs cannot be simply attributed to the global approach breaking down.

Thinking of the local coefficient matrix $\mathsf{M}_{\mathscr{L},1}$ as the lowest order $\mathsf{M}_{\mathscr{G},1}^{(0)}$ of a

perturbative expansion in k of the dissipative contributions to $\mathsf{M}_{\mathscr{G},1}$, i.e.

$$\mathsf{M}_{\mathscr{G},1} = \mathsf{M}^{(0)}_{\mathscr{G},1} + k\,\mathsf{M}^{(1)}_{\mathscr{G},1} + \cdots ,$$

it would even be tempting to disregard the EP singularities predicted by the LME as mathematical artifacts, and trust instead the *a priori* more physical (given its microscopical derivation, see App. B.1) GME. However, as advanced in Sec. 3.4.3, this interpretation is *not* valid here. To see why, we only need to calculate $\mathsf{M}^{(0)}_{\mathscr{G},1}$ from Eq. (70b) and show that it differs from $\mathsf{M}_{\mathscr{L},1}$ in Eq. (58). Namely, we must set $k = 0$ in all terms arising from the global dissipators $\mathscr{G}^{\dagger}_{\alpha}$ (33), while keeping those from the commutator part of Eq. (32) intact [113]. This is achieved by replacing all coefficients $\tilde{\Delta}_j$ in $\mathsf{M}_{\mathscr{G},1}$ by $(\Delta^{(h)}_{\omega} + \Delta^{(c)}_{\omega})/2$, i.e.,

$$\mathsf{M}^{(0)}_{\mathscr{G},1} = \frac{1}{2}\begin{pmatrix} \frac{1}{2}(\Delta^{(h)}_{\omega} + \Delta^{(c)}_{\omega}) & 2 & 0 & 0 \\ -2\omega^2 & \frac{1}{2}(\Delta^{(h)}_{\omega} + \Delta^{(c)}_{\omega}) & -2k & 0 \\ 0 & 0 & \frac{1}{2}(\Delta^{(h)}_{\omega} + \Delta^{(c)}_{\omega}) & 2 \\ -2k & 0 & -2\omega^2 & \frac{1}{2}(\Delta^{(h)}_{\omega} + \Delta^{(c)}_{\omega}) \end{pmatrix} \neq \mathsf{M}_{\mathscr{L},1}. \tag{71}$$

That is, even in the limit $k = 0$, each heat bath continues to act globally on *both* resonators, rather than on the resonator directly coupled to it. This is a side-effect of the secular approximation, which introduces a 'heat leak' channel. And that is why the GME predicts steady-state heat flows in the resonant case even at vanishing coupling, as noted in Refs. [88, 89].

Eq. (71) confronts us with the fact that the LME is *not*, in general, a limiting case of the GME. But then, *what is it?* What we are after is a *microscopic justification* of the local equation (57) capable of explaining why it succeeds in capturing the EPs detected experimentally in [67], while the global equation (70a) fails.

3.7.3 Redfield equation

We now resort to the Redfield equation, as introduced in Eqs. (28) and (29), to shed light on the nature of the LME. As outlined in Sec. 3.4.1, this equation is the last step in the derivation of the GME, before forcing the GKSL form by means of the (full) secular approximation. Consequently, in the regime of positivity, the Redfield equation is *always* more accurate than the GME. In the context of quan-

tum thermodynamics, however, the main shortcoming of the Redfield equation is its lack of GKSL structure. Without it, it may fail to generate a completely positive dynamics [138, 139]. Nonetheless, if used with caution, the Redfield equation can still yield thermodynamically sound results [140, 141, 142].

To be more precise, (28) is a *partial Redfield equation* [88, 100, 105, 140]. That is, a simplified version of the equation in which its most rapidly oscillating terms—but *not all* oscillating terms—are averaged out under a coarse graining of time. Below, we also discard the *Lamb shifts*, defined in Appendix B.1. These terms introduce an effective renormalization of the energy levels of the open system leaving untouched its steady–state properties [143]. This approximation has been verified to lead to excellent approximations of steady–state and long–time dynamics [144]. The resulting system is

$$\frac{\mathrm{d}\langle \mathbf{q} \rangle}{\mathrm{d}t} = \mathsf{M}_{\mathscr{R},1}\,\langle \mathbf{q} \rangle, \tag{72a}$$

$$\mathsf{M}_{\mathscr{R},1} = \frac{1}{2}\begin{pmatrix} [\mathsf{M}_{\mathscr{R},1}]_{11} & 2 & [\mathsf{M}_{\mathscr{R},1}]_{13} & 0 \\ -2\omega^2 & \bar{\Delta}_h & -2k & \delta_h \\ [\mathsf{M}_{\mathscr{R},1}]_{31} & 0 & [\mathsf{M}_{\mathscr{R},1}]_{33} & 2 \\ -2\omega^2 & \delta_c & -2\omega^2 & \bar{\Delta}_c \end{pmatrix}, \tag{72b}$$

where $\delta_\alpha \coloneqq \frac{1}{2}(\Delta_1^{(\alpha)} - \Delta_2^{(\alpha)})$, $\bar{\Delta}_\alpha \coloneqq \frac{1}{2}(\Delta_1^{(\alpha)} + \Delta_2^{(\alpha)})$, and

$$\begin{aligned}
[\mathsf{M}_{\mathscr{R},1}]_{11} &= \frac{\Omega_2 - \Omega_1}{4}\left(\frac{\Delta_1^{(c)}}{\Omega_2} - \frac{\Delta_2^{(c)}}{\Omega_1}\right) + \frac{\Omega_2 + \Omega_1}{4}\left(\frac{\Delta_1^{(h)}}{\Omega_2} + \frac{\Delta_2^{(h)}}{\Omega_1}\right) \\
[\mathsf{M}_{\mathscr{R},1}]_{13} &= \frac{\Omega_2 - \Omega_1}{4}\left(\frac{\Delta_1^{(c)}}{\Omega_2} + \frac{\Delta_2^{(c)}}{\Omega_1}\right) + \frac{\Omega_2 + \Omega_1}{4}\left(\frac{\Delta_1^{(h)}}{\Omega_2} - \frac{\Delta_2^{(h)}}{\Omega_1}\right) \\
[\mathsf{M}_{\mathscr{R},1}]_{31} &= \frac{\Omega_2 + \Omega_1}{4}\left(\frac{\Delta_1^{(c)}}{\Omega_2} - \frac{\Delta_2^{(c)}}{\Omega_1}\right) + \frac{\Omega_2 - \Omega_1}{4}\left(\frac{\Delta_1^{(h)}}{\Omega_2} - \frac{\Delta_2^{(h)}}{\Omega_1}\right) \\
[\mathsf{M}_{\mathscr{R},1}]_{33} &= \frac{\Omega_2 + \Omega_1}{4}\left(\frac{\Delta_1^{(c)}}{\Omega_2} + \frac{\Delta_2^{(c)}}{\Omega_1}\right) + \frac{\Omega_2 - \Omega_1}{4}\left(\frac{\Delta_1^{(h)}}{\Omega_2} + \frac{\Delta_2^{(h)}}{\Omega_1}\right).
\end{aligned} \tag{72c}$$

In spite of the cumbersome expressions, one can see that the zeroth order term $\mathsf{M}_{\mathscr{R},1}^{(0)}$ of the k-expansion of the dissipative part of $\mathsf{M}_{\mathscr{R},1}$,

$$\mathsf{M}_{\mathscr{R},1} = \mathsf{M}_{\mathscr{R},1}^{(0)} + k\,\mathsf{M}_{\mathscr{R},1}^{(1)} + k^2\,\mathsf{M}_{\mathscr{R},1}^{(2)} \cdots, \tag{73}$$

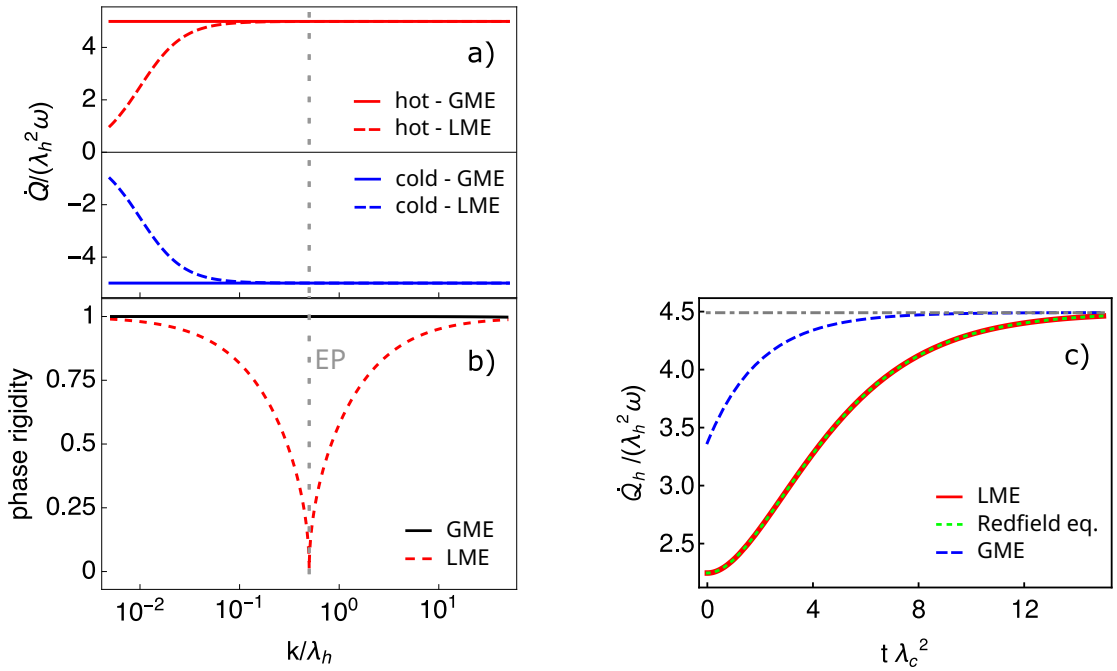

Figure 11: **Heat currents at an exceptional point. a)** Steady-state heat currents from the hot bath (red) and the cold bath (blue) as a function of k, according to the GME (solid) and the LME (dashed). **b)** Phase rigidity calculated according to the LME (dashed red) for the two coalescing eigenvectors, and according to the GME (solid black), for which no eigenvectors coalesce. Note that the phase rigidity seems to converge to unity (solid black) away from the EP. Recall from Sec. 3.6.1 that $\Phi_i = 1$ only for Hermitian systems. In fact, evaluating the behaviour of Φ_i in the range of parameters shown in the plot, we see that the phase rigidity remains $\Phi_i < 1$, albeit by a very small amount ($\sim 10^{-5}$). The position of the EP according to (61) is indicated by the dotted grey line across **a)** and **b)**. **c)** Transient of the hot heat current $\dot{\mathcal{Q}}_h(t)$ according to the LME (solid red), the GME (dashed blue), and the Redfield equation (dotted green). The steady-state value is indicated by the dot-dashed grey line. The global approach thus deviates from the true heat-flow dynamics, set by the Redfield equation. On the contrary, the local approach remains accurate throughout. Parameters are as in Fig. 10, except for $\omega = 1$. As initial state, we take the tensor product of the thermal state of each oscillator at its local bath's temperature.

is identical to $\mathrm{M}_{\mathscr{L},1}$ in Eq. (58) (or, equivalently, $\mathscr{R}_\alpha^{\dagger\,(0)} = \mathscr{L}_\alpha^\dagger$, see Appendix B.4). One only needs to set $k = 0$ in all dissipative contributions of Eq. (28), which is equivalent to setting $k = 0$ in the $\bar{\Delta}_\alpha$ and δ_α terms, as well as in the four matrix elements written out in Eqs. (72c).

We have thus shown that, at resonance, *the LME is the low-k limit of the Redfield equation; not of the GME*. In fact, it is easy to see that $\mathscr{R}_\alpha^{\dagger\,(0)} = \mathscr{L}_\alpha^\dagger$ holds as well out of resonance for *any* multipartite model, as long as the coupling to the heat baths is mediated by 'frequency filters'. More precisely, these are multipartite systems in which the coupling $\boldsymbol{H}_{SB}$ is of the form, e.g., $\boldsymbol{a}_\alpha \otimes \boldsymbol{B}_\alpha + \text{h.c.}$ or $|\epsilon_i\rangle\langle\epsilon_j| \otimes \boldsymbol{B}_\alpha + \text{h.c.}$, where $|\epsilon_i\rangle$ are eigenstates of the local Hamiltonian $\boldsymbol{H}_\alpha^{(\text{loc})}$ (see Appendix B.4 for details). In such settings, the LME emerges *directly* from the Redfield equation. This is why $\mathrm{M}_{\mathscr{R},1}$ and $\mathrm{M}_{\mathscr{L},1}$ share the same pattern of EPs in parameter space (cf. Fig. 10).

Crucially, unlike the Redfield approach, the LME is guaranteed to generate a completely positive dissipative dynamics [111]. In addition, this explains the unlikely success of the LME over the GME at low k, when the secular approximation breaks down [88, 89]. In this new light, we see that the LME simply *bypasses* the secular approximation. This is one of the main results of this section.

Furthermore, note from Eq. (63) that the eigenstates of $\boldsymbol{H}_S$ do *not* depend on k. It then becomes clear why the local approach remains accurate even at larger couplings at resonance [89]: A small-k approximation of the dissipators $\mathscr{R}_\alpha^\dagger$ (or $\mathscr{G}_\alpha^\dagger$) is valid over a wider range of couplings if the expansion affects only the Bohr frequencies ω, but not the jump operators $\boldsymbol{A}_\omega^{(\alpha)}$. Conversely, out of resonance, the LME loses validity at non-zero couplings, since the eigenstates of $\boldsymbol{H}_S$ are then explicitly dependent on k (see Appendix B.4). We note as well that EPs can be studied exploiting the stochastic unraveling of GKSL master equations to define an effective non-Hermitian Hamiltonian, as shown in [137].

The failure of the GME at capturing the correct dynamics is precisely due to the fact that the secular approximation—required by the GME—'washes away' relevant *dynamical* features. We have just illustrated this with the disappearance of the EPs. Next, we show that, even when the LME and GME do agree in their steady-state predictions, the local approach can generate more accurate heat-flow dynamics.

3.7.4 Heat currents

The *instantaneous* rate of heat flow into the system from each of the baths can be obtained by generalising Eq. (34b) to

$$\dot{\mathcal{Q}}_{\alpha,\mathscr{D}}(t) \coloneqq \langle \mathscr{D}_\alpha^\dagger(\boldsymbol{H}_S)\rangle_t, \tag{74}$$

where the transient heat currents $\dot{\mathcal{Q}}_\alpha(t)$ generally *do not* sum up to zero, nor obey the Clausius-like inequality (34a); they only do so at very long times, $t \to \infty$. Directly applying this definition using the local, global, and Redfield dissipators gives

$$\begin{aligned}
\dot{\mathcal{Q}}_{\alpha,\mathscr{L}} &= \frac{\Delta_\omega^{(\alpha)}}{2}\big(\langle \boldsymbol{p}_\alpha^2\rangle + \omega^2\langle \boldsymbol{x}_\alpha^2\rangle + k\langle \boldsymbol{x}_h\boldsymbol{x}_c\rangle\big) + \frac{\Sigma_\omega^{(\alpha)}}{2},\\
\dot{\mathcal{Q}}_{\alpha,\mathscr{G}} &= \frac{1}{4}\sum\nolimits_j \big[\Delta_{\Omega_j}^{(\alpha)}\big(\langle \boldsymbol{\Pi}_j^2\rangle + \Omega_j^2\langle \boldsymbol{\eta}_j^2\rangle\big) + \Sigma_{\Omega_j}^{(\alpha)}\big],\\
\dot{\mathcal{Q}}_{\alpha,\mathscr{R}} &= \dot{\mathcal{Q}}_{\alpha,\mathscr{G}} + \frac{\Delta_1^{(\alpha)} + \Delta_2^{(\alpha)}}{4}\big(\Omega_1\Omega_2\langle \boldsymbol{\eta}_1\boldsymbol{\eta}_2\rangle + \langle \boldsymbol{\Pi}_1\boldsymbol{\Pi}_2\rangle\big),
\end{aligned} \tag{75}$$

where $\Sigma_\omega^{(\alpha)} \coloneqq \frac{1}{2\omega}(\gamma_{-\omega}^{(\alpha)} + \gamma_\omega^{(\alpha)})$, and $\langle \boldsymbol{\eta}_i\boldsymbol{\eta}_j\rangle$ and $\langle \boldsymbol{\Pi}_i\boldsymbol{\Pi}_j\rangle$ are second-order moments. Therefore, in order to evaluate Eqs. (75) we must set up and solve the corresponding linear system of 10 equations with coefficient matrices $\mathsf{M}_{2,\mathscr{D}}$ from Eq. (55). This is a rather tedious but, otherwise, straightforward process. As it turns out, the 10×10 matrices $\mathsf{M}_{\mathscr{L},2}$ and $\mathsf{M}_{\mathscr{R},2}$ have the same exceptional points than their 4×4 first-order counterparts $\mathsf{M}_{\mathscr{L},1}$ and $\mathsf{M}_{\mathscr{R},1}$. We defer details to Appendix B.2.

In Fig. 11 we tune the parameters to be at an exceptional point of the system according to Eq. (61), and plot both steady-state and transient heat currents. For the chosen parameters, LME and GME agree in their steady-state predictions to a very good approximation, see panel a) and b) of Fig. 11. However, local and global dynamics do differ significantly at finite time. In contrast, the Redfield equation agrees with the LME at all times, see panel c) of Fig. 11. This suggests that, within its error bars, *the local approach can be superior to the global one when studying the thermodynamics of multipartite systems with weak internal couplings*.

3.8 Conclusion

We have analysed one of the central problems in quantum thermodynamics. Namely, the modelling of heat flows across open systems with quantum master equations. We have shown that the two most common approaches—the local and the global master equations—can make very different predictions. Firstly, our results illustrate that the local approach succeeds at capturing dynamical features, in the form of exceptional points, that escape the global master equation. Secondly, we have found that, when considering degenerate multipartite open quantum systems with weak internal coupling, the LME also yields much more accurate heat-flow dynamics than the GME, even when both agree in the steady-state.

Furthermore, we have shown that the LME follows directly from the more accurate Redfield equation, and is generally *not* a weak-coupling limit of the GME. This is always the case for any multipartite weakly-interacting open quantum system that couples to the environment(s) via single-frequency contacts, such as a qubit or a harmonic oscillator. Therefore, for such systems, the LME emerges as an accurate and computationally efficient alternative to the Redfield equation. It proves to be superior to the GME and, in contrast to the Redfield equation, it does guarantee positivity.

These results have profound consequences for quantum thermodynamics. Namely, modelling heat flow in a quantum thermal machine with the local approach instead of the global one, could make a sizeable difference in the predicted heat transfer in, e.g., any thermalising stroke of a finite-time thermodynamic cycle. This could result in a radically different assessment of both performance and power output. However, it is important to remember that the local approach has a limited range of validity. Specifically, it is unsuitable for open systems with *strong* internal couplings (i.e., large k), and it can lead to unphysical results at odds with thermodynamics. Finding an accurate and scalable master equation for such scenarios still remains an open challenge.

Code availability

The code used to produce the figures is available upon reasonable request to s.scali@exeter.ac.uk.

4 Quantum–classical correspondence in spin–boson equilibrium states at arbitrary coupling

4.1 Statement of contribution

In the following work, I generalized the theory developed in Ref. [145] to anisotropic baths and produced all the classical results in the section. Among these, I discovered the third key result we present in this section. This is the presence of a classical counterpart to quantum coherences in equilibrium induced by the coupling to the environment. To do so, I rebuilt and generalized the existing code for the stochastic simulations. I checked the results for the ultrastrong coupling, evaluated the limit of the classical steady state at zero temperature and within this, calculated the reorganization energy result. Finally, I participated in generating the figures, text and reviewing the manuscript. Janet Anders devised the original idea of the quantum–classical correspondence of the large spin limit at all coupling strengths.

4.2 Summary

The equilibrium properties of nanoscale systems can deviate significantly from standard thermodynamics due to their coupling to an environment. For the θ-angled spin-boson model, we first derive a compact and general form of the classical equilibrium state including environmental corrections to all orders. Secondly, for the quantum spin-boson model we prove, by carefully taking a large spin limit, that Bohr's quantum-classical correspondence persists at all coupling strengths. This correspondence gives insight into the conditions for a coupled quantum spin to be well-approximated by a coupled classical spin-vector. Thirdly, we demonstrate that previously identified environment-induced 'coherences' in the equilibrium state of weakly coupled quantum spins, do *not* disappear in the classical case. Finally, we provide the first classification of the coupling parameter regimes for the spin-boson model, from weak to ultrastrong, both for the quantum case and the classical setting. Our results shed light on the interplay of quantum and mean force corrections in equilibrium states of the spin-boson model, and will help draw the quantum to classical boundary in a range of fields, such as magnetism and

exciton dynamics.

4.3 Introduction

Bohr's correspondence principle [146] played an essential role in the early development of quantum mechanics. Since then, a variety of interpretations and applications of the correspondence principle have been explored [147, 148, 149, 150, 151, 152, 153, 154]. One form asks if the statistical properties of a quantum system approach those of its classical counterpart in the limit of large quantum numbers [149, 150]. This question was answered affirmatively by Millard and Leff, and Lieb for a quantum spin system [147, 148]. They proved that the system's thermodynamic partition function $Z_{\mathrm{S}}^{\mathrm{qu}}$ associated with the Gibbs state, converges to the corresponding classical partition function $Z_{\mathrm{S}}^{\mathrm{cl}}$, in the limit of large spins. Such correspondence gives insight into the conditions for a quantum thermodynamic system to be well-approximated by its classical counterpart [153, 154]. While $Z_{\mathrm{S}}^{\mathrm{qu}}$ is computationally tough to evaluate for many systems, $Z_{\mathrm{S}}^{\mathrm{cl}}$ offers tractable expressions with which thermodynamic properties, such as free energies, susceptibilities and correlation functions, can readily be computed [147, 148]. Similarly, many dynamical approaches solve a classical problem rather than the much harder quantum problem. For example, sophisticated atomistic simulations of the magnetisation dynamics in magnetic materials [155, 156, 157, 158, 159] solve the evolution of millions of interacting classical spins. A corresponding quantum simulation [160] would require no less than a full–blown quantum computer as its hardware.

Meanwhile, in the field of quantum thermodynamics, extensive progress has recently been made in constructing a comprehensive framework of "strong coupling thermodynamics" for classical [161, 162, 163, 164, 165, 166] and quantum [167, 168, 169, 170, 171, 172, 173, 174, 175, 176, 177] systems. This framework extends standard thermodynamic relations to systems whose coupling to a thermal environment can not be neglected. The equilibrium state is then no longer the quantum or classical Gibbs state, but must be replaced with the environment-corrected mean force (Gibbs) state [176, 177, 178]. These modifications bring into question the validity of the correspondence principle when the environment-coupling is no longer negligible. Mathematically, the challenge is that in addition

to tracing over the system, one must also evaluate the trace over the environment.

Strong coupling contributions are present for both classical and quantum systems. However, a quantitative characterisation of the difference between these two predictions, in various coupling regimes, is missing. For example, apart from temperature, what are the parameters controlling the deviations between the quantum and classical spin expectation values? Do coherences, found to persist in the mean force equilibrium state of a quantum system [179], decohere when taking the classical limit? How strong does the environmental coupling need to be for the spin-boson model to be well-described by weak or ultrastrong coupling approximations? In this section, we answer these questions for the particular case of a spin S_0 coupled to a one-dimensional bosonic environment such that both dephasing and detuning can occur (θ-angled spin-boson model).

4.4 Setting

This generalised version of the spin-boson model [180, 181] describes a vast range of physical contexts, including excitation energy transfer processes in molecular aggregates described by the Frenkel exciton Hamiltonian [182, 183, 184, 185, 186, 187, 188], the electronic occupation of a double quantum dot whose electronic dipole moment couples to the substrate phonons in a semi-conductor [179], an electronic, nuclear or effective spin exposed to a magnetic field and interacting with an (anisotropic) phononic, electronic or magnonic environment [145, 189, 190, 191, 192], and a plethora of other aspects of quantum dots, ultracold atomic impurities, and superconducting circuits [193, 194, 195, 196]. In all these contexts, an effective "spin" S interacts with an environment, where S is a vector of operators (with units of angular momentum) whose components fulfil the angular momentum commutation relations $[S_j, S_k] = i\hbar \sum_l \epsilon_{jkl} S_l$ with $j, k, l \in \{x, y, z\}$. We will consider spins of any length S_0, i.e. $\mathrm{S}^2 = S_0(S_0+\hbar)\mathbf{1}$. The system Hamiltonian is

$$H_{\mathrm{S}} = -\omega_{\mathrm{L}} S_z, \tag{76}$$

where the system energy level spacing is $\hbar\omega_{\mathrm{L}} > 0$ and the energy axis is in the $-z$-direction without loss of generality. For a double quantum dot, the frequency ω_{L} is determined by the energetic detuning and the tunneling between the dots [179]. For an electron spin with $S_0 = \hbar/2$, the energy gap is set by a gyromagnetic ratio γ

and an external magnetic field $\mathbf{B}_{\rm ext} = -B_{\rm ext}\hat{\mathbf{z}}$, such that $\omega_{\rm L} = \gamma B_{\rm ext}$ is the Larmor frequency.

The spin system is in contact with a bosonic reservoir, which is responsible for the dissipation and equilibration of the system. Typically, this environment will consist of phononic modes or an electromagnetic field [177, 197]. The bare Hamiltonian of the reservoir is

$$H_{\rm R} = \frac{1}{2}\int_0^\infty \mathrm{d}\omega \, \left(P_\omega^2 + \omega^2 X_\omega^2\right), \tag{77}$$

where X_ω and P_ω are the position and momentum operators of the reservoir mode at frequency ω which satisfy the canonical commutation relations $[X_\omega, P_{\omega'}] = i\hbar\,\delta(\omega - \omega')$. With the identifications made in (76) and (77), the system-reservoir Hamiltonian is

$$H_{\rm tot} = H_{\rm S} + H_{\rm R} + H_{\rm int}, \tag{78}$$

which contains a system-reservoir coupling $H_{\rm int}$. Physically, the coupling can often be approximated to be linear in the canonical reservoir operators [177], and is then modelled as [179, 197, 198]

$$H_{\rm int} = S_\theta \int_0^\infty \mathrm{d}\omega \, C_\omega X_\omega, \tag{79}$$

where the coupling function C_ω determines the interaction strength between the system and each reservoir mode ω. C_ω is related to the reservoir spectral density J_ω via $J_\omega = C_\omega^2/(2\omega)$. It is important to note that the coupling is via the spin (component) operator $S_\theta = S_z\cos\theta - S_x\sin\theta$ which is at an angle θ with respect to the system's bare energy axis, see Fig. 12. For example, for a double quantum dot [179], the angle θ is determined by the ratio of detuning and tunnelling parameters.

In what follows, we will need an integrated form of the spectral density, namely

$$Q = \int_0^\infty \mathrm{d}\omega \, \frac{J_\omega}{\omega} = \int_0^\infty \mathrm{d}\omega \, \frac{C_\omega^2}{2\omega^2}. \tag{80}$$

This quantity is a measure of the strength of the system–environment coupling and it is sometimes called "reorganization energy" [178, 199, 200, 201]. The analytical results discussed below are valid for arbitrary coupling functions C_ω (or re-

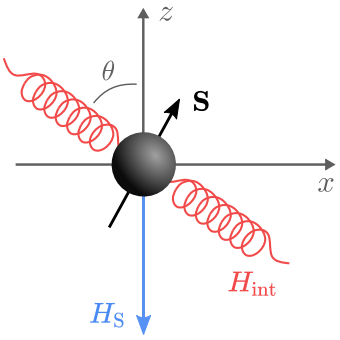

Figure 12: **Illustration of bare and interaction energy axes.** A spin operator (vector) S with system Hamiltonian $H_{\rm S}$ with energy axis in the $-z$-direction is coupled in θ-direction to a harmonic environment via $H_{\rm int}$.

organisation energies Q). The plots assume Lorentzians $J_\omega = (2\Gamma\, Q/\pi)\,\omega_0^2\omega/((\omega_0^2-\omega^2)^2+\Gamma^2\omega^2)$, where ω_0 is the resonant frequency of the Lorentzian [145] and Γ the peak width.

We will model $H_{\rm tot}$ (Eq. (78)) either fully quantum mechanically as detailed above, or fully classically. To obtain the classical case, the spin S operator will be replaced by a three-dimensional vector of length S_0, and the reservoir operators X_ω and P_ω will be replaced by classical phase–space coordinates. Below, we evaluate the spin's so-called mean force (Gibbs) states, CMF and QMF, for the classical and quantum case, respectively. The mean force approach postulates [177] that the equilibrium state of a system in contact with a reservoir at temperature T is the mean force (MF) state, defined as

$$\tau_{\rm MF} := \mathrm{tr}_{\rm R}[\tau_{\rm tot}] = \mathrm{tr}_{\rm R}\left[\frac{e^{-\beta H_{\rm tot}}}{Z_{\rm tot}}\right]. \tag{81}$$

That is, $\tau_{\rm MF}$ is the reduced system state of the global Gibbs state $\tau_{\rm tot}$, where $\beta = 1/k_{\rm B}T$ is the inverse temperature with $k_{\rm B}$ the Boltzmann constant, and $Z_{\rm tot}$ is the global partition function. Quantum mechanically, $\mathrm{tr}_{\rm R}$ stands for the operator trace over the reservoir space while classically, "tracing" is done by integrating over the reservoir degrees of freedom. Further detail on classical and quantum tracing for the spin and the reservoir, respectively, is given in Appendix C.1.

While the formal definition of $\tau_{\rm MF}$ is deceptively simple, carrying out the trace over the reservoir – to obtain a quantum expression of $\tau_{\rm MF}$ in terms of system operators alone – is notoriously difficult. Often, expansions for weak coupling are

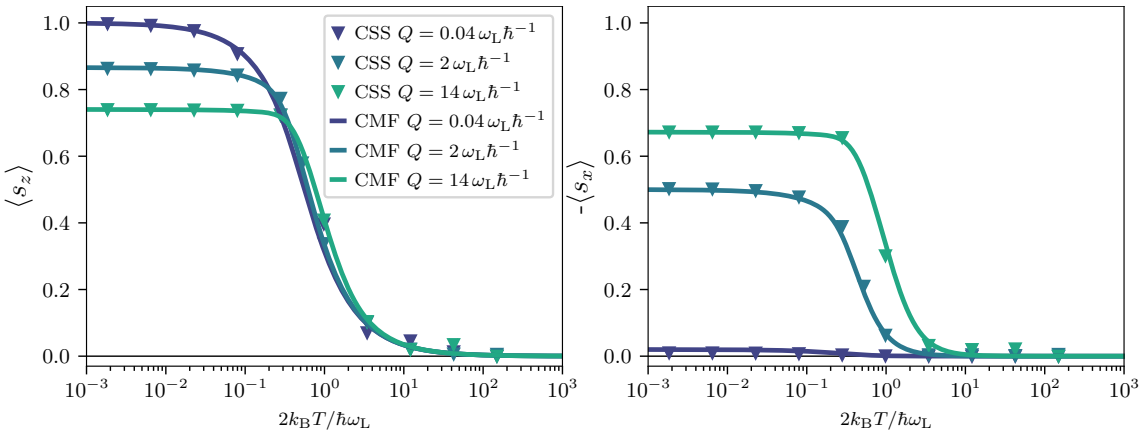

Figure 13: **Classical mean force and steady–state spin expectation values.** Normalised expectation values of the classical spin components $\langle s_z \rangle$ **(left)** and $\langle s_x \rangle$ **(right)** as a function of temperature. These are obtained with: (CSS) the long time average of the dynamical evolution of the spin, $\langle s_k \rangle = \langle S_k \rangle_{\rm CSS} / S_0$; and (CMF) the classical MF state (Eq. (82)), $\langle s_k \rangle = \langle S_k \rangle_{\rm MF} / S_0$. These are shown for three different coupling strengths $Q = 0.04\,\omega_{\rm L}\hbar^{-1}, 2\,\omega_{\rm L}\hbar^{-1}, 14\,\omega_{\rm L}\hbar^{-1}$, that range from the weak to the strong coupling regimes. In all three cases, we see that the MF predictions are fully consistent with the results of the dynamics. All plots are for Lorentzian coupling with $\omega_0 = 7\omega_{\rm L}$, $\Gamma = 5\omega_{\rm L}$, and coupling angle $\theta = 45°$. The temperature scale shown corresponds to a spin $S_0 = \hbar/2$.

made [167, 179]. For a general quantum system (i.e. not necessarily a spin), an expression of $\tau_{\rm MF}$ has recently been derived in this limit [178]. Furthermore, recent progress has been made on expressions of the quantum $\tau_{\rm MF}$ in the limit of ultrastrong coupling [178], and for large but finite coupling [176, 177, 202]. Moreover, high temperature expansions have been derived that are also valid at intermediate coupling strengths [188]. However, the low and intermediate temperature form of the quantum $\tau_{\rm MF}$ for intermediate coupling is not known, neither in general nor for the θ–angled spin boson model [203].

4.5 Classical MF state at arbitrary coupling

In contrast, here we establish that the analogous problem of a *classical* spin vector of arbitrary length S_0, coupled to a harmonic reservoir via Eq. (79), is tractable for arbitrary coupling function C_ω and arbitrary temperature. By carrying out the (classical) partial trace over the reservoir, i.e. $\mathrm{tr}_{\rm R}^{\rm cl}[\tau_{\rm tot}]$, we uncover a rather com-

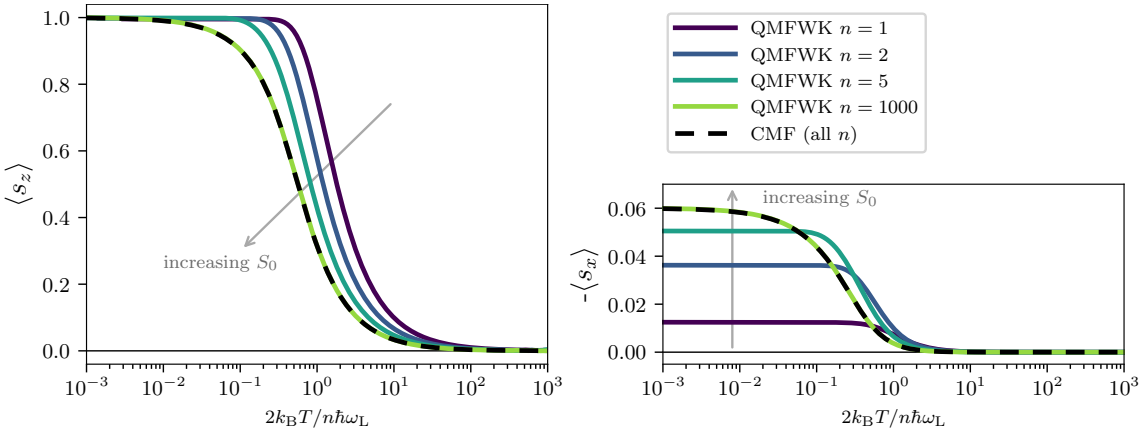

Figure 14: **Classical and quantum mean force spin components.** Normalised expectation values of the spin components $\langle s_z \rangle$ **(left)** and $\langle s_x \rangle$ **(right)** obtained with: (QMFWK) the quantum MF partition function $\tilde{Z}_{\mathrm{S}}^{\mathrm{qu}}$ in the weak coupling limit for a spin of length $S_0 = n\hbar/2$ ($n = 1, 2, 5, 1000$); (CMF) the classical MF partition function $\tilde{Z}_{\mathrm{S}}^{\mathrm{cl}}$ given in (82). As the length S_0 of the quantum spin is increased, the quantum mean force prediction QMFWK converges to that corresponding to the CMF state. Non-zero s_x **(right)** indicate "coherences" with respect to the system's bare energy axis (z). These arise entirely due to the spin-reservoir interaction. Such coherences have been discussed for the quantum case [179]. Here we find that they also arise in the classical CMF and, comparing like with like for the same spin length $S_0 = \hbar/2$, the classical "coherences" are *larger* than those of the quantum spin. All plots are for a weak coupling strength, $\alpha = 0.06$, and $\theta = \pi/4$.

pact expression for the spin's CMF state τ_{MF} and the CMF partition function $\tilde{Z}_{\mathrm{S}}^{\mathrm{cl}}$:

$$\tau_{\mathrm{MF}} = \frac{e^{-\beta(H_{\mathrm{S}} - QS_\theta^2)}}{\tilde{Z}_{\mathrm{S}}^{\mathrm{cl}}}, \qquad (82)$$

$$\text{with} \quad \tilde{Z}_{\mathrm{S}}^{\mathrm{cl}} = \mathrm{tr}_{\mathrm{S}}^{\mathrm{cl}}[e^{-\beta(H_{\mathrm{S}} - QS_\theta^2)}].$$

The state τ_{MF} clearly differs from the standard Gibbs state by the presence of the reorganisation energy term $-QS_\theta^2$. The quadratic dependence on S_θ changes the character of the distribution, from a standard exponential to an exponential with a positive quadratic term, altering significantly the state whenever the system–reservoir coupling is non-negligible.

Throughout this section, we will consider that the MF state is the equilibrium state reached by a system in contact with a thermal bath. While this is widely thought to be the case, some open questions remain about formal proofs showing the convergence of the dynamics towards the steady state predicted by the MF state [170, 171, 172, 177, 179, 204, 205, 206, 207, 208, 209]. For example, for quantum systems, this convergence has only been proven in the weak [167] and ultrastrong limits [176], while for intermediate coupling strengths there is nu-

merical evidence for the validity of the MF state [181]. Here, we numerically verify the convergence of the dynamics towards the MF state for the case of the classical spin at arbitrary coupling strength. This is possible thanks to the numerical method proposed in [145]. Fig. 13 shows the long time average of the spin components once the dynamics has reached steady state (CSS, triangles), together with the expectation values predicted by the static MF state (CMF, solid lines), for a wide range of coupling strengths going from weak to strong coupling [6]. We find that both predictions are in excellent agreement, providing strong evidence for the convergence of the dynamics towards the MF. The compact expression (82) for the CMF state, as well as the numerical verification that the dynamical steady state matches the CMF state, are the first result of this section.

4.6 Quantum–classical correspondence

We now demonstrate that the quantum partition function $\tilde{Z}_{\rm S}^{\rm qu}$, which includes arbitrarily large mean force corrections, converges to the classical one, $\tilde{Z}_{\rm S}^{\rm cl}$ in Eq. (82).

A well-known classical limit of a quantum spin is to increase the quantum spin's length, $S_0 \to \infty$. This is because, when S_0 increases, the quantised angular momentum level spacing relative to S_0 decreases, approaching a continuum of states that can be described in terms of a classical vector [146]. Taking the large spin limit for a spin-S_0 system can be achieved following an approach used by Fisher when treating an uncoupled spin with Hamiltonian $H_{\rm S}$ [210]. This involves introducing a rescaling of the spin operators via $s_j = S_j/S_0$ so that the commutation rule becomes $[s_j, s_k] = i\hbar\,\epsilon_{jkl}\,s_l/S_0$. Hence, in the limit of $S_0 \to \infty$, the scaled operators will commute, so in that regard they can be considered as classical quantities [210]. Millard & Leff [147] take this further and prove, for any spin Hamiltonian H in the spin Hilbert space $\mathscr{H}_S$, the identity

$$\lim_{S_0\to\infty} \frac{\hbar}{2S_0+\hbar}\,\mathrm{tr}_{\rm S}^{\rm qu}\left[e^{-\beta H}\right] = \lim_{S_0\to\infty}\frac{1}{4\pi}\int_0^{2\pi} d\varphi \int_0^{\pi} d\vartheta\,\sin\vartheta\, e^{-\beta H(S_0,\vartheta,\varphi)}, \tag{83}$$

provided the limit on the right hand side exists [7]. Here $H(S_0,\vartheta,\varphi)$ is the classical

[6] See later discussions where the different regimes of coupling strength are thoroughly characterised.

[7] The factor of $\hbar/(2S_0+\hbar)$ guarantees that the sides of (83) are equal for $\beta = 0$. For a fixed value of S_0, this pre-factor is un-important as it immediately cancels in any calculation of expectation values, i.e. for a quantum system, the expressions $\frac{\hbar}{2S_0+\hbar}Z_{\rm S}^{\rm qu}(\beta,S_0)$ and $Z_{\rm S}^{\rm qu}(\beta,S_0)$ give the same expectation values.

spin-S_0 Hamiltonian, where the spin-vector S is parametrised by two angles, φ and ϑ, such that $S_x = S_0 \sin\vartheta\cos\varphi, S_y = S_0 \sin\vartheta \sin\varphi$ and $S_z = S_0\cos\vartheta$. Eq. (83) was further confirmed by Lieb who provides a rigorous argument based on the properties of spin-coherent states [148].

Note, though, if one simply takes the $S_0 \to \infty$ limit in (83), with H being the system Hamiltonian $H_{\rm S} \propto S_0$, that would have the same effect as sending $\beta \to \infty$; namely, all population will go to the ground state. Instead, maintaining a non-trivial temperature dependence after taking the S_0-limit requires a further rescaling step. One approach involves a rescaling of the physical parameters of the Hamiltonian H, as followed, e.g., by Fisher [210]. A second approach is to rescale the inverse temperature via $\beta S_0 = \beta'$, and take the limit $S_0 \to \infty$ with β' held fixed. This is the limit we will take here. The effect of this constrained limit can readily be seen for the thermal states of the uncoupled classical or quantum spin. The classical partition function $Z_{\rm S}^{\rm cl}(\beta S_0) = \sinh(\beta S_0\omega_{\rm L})/\beta S_0\omega_{\rm L}$ is left invariant because β and S_0 always appear together in $Z_{\rm S}^{\rm cl}$. In contrast, the quantum partition function $Z_{\rm S}^{\rm qu}(\beta, S_0) = \sinh\big(\beta(S_0+\hbar/2)\omega_{\rm L}\big)/\sinh\big(\beta\hbar\omega_{\rm L}/2\big)$ is altered in the constrained limit, since $Z_{\rm S}^{\rm qu}$ separately depends on β and S_0. Eq. (83) then expresses the convergence of the partition functions [147, 148, 210], i.e. $\frac{\hbar}{2S_0+\hbar}\, Z_{\rm S}^{\rm qu}(\beta, S_0) \to Z_{\rm S}^{\rm cl}(\beta S_0)$.

We now take a step further and extend this result to the case of a spin *coupled to a reservoir*. The first step is to consider that the relevant Hilbert space is now the tensor product space of spin and reservoir degrees of freedom, $\mathscr{H}_S \otimes \mathscr{H}_B$. It was argued by Lieb [148] that (83) remains valid in this case, i.e. even when $H \in \mathscr{H}_S \otimes \mathscr{H}_B$. This means we can replace H in (83) with our $H_{\rm tot}$. But note that the trace is still only over the system Hilbert space $\mathscr{H}_S$. Thus, formally one obtains an operator valued identity for operators on $\mathscr{H}_B$. The second step is then to evaluate the trace over the reservoir degrees of freedom. To do so, we start by writing the total unnormalised Gibbs state as

$$e^{-\beta H_{\rm tot}} = \exp\left[-\beta'\left(-\omega_{\rm L}s_z + \frac{H_{\rm R}}{S_0} + s_\theta \int_0^\infty {\rm d}\omega\, C_\omega X_\omega\right)\right], \tag{84}$$

with the rescaled inverse temperature $\beta' = \beta S_0$. Since β' is constant as the limit $S_0 \to \infty$ is taken, doing so rescales the spin operators, as required. But it also rescales $H_{\rm R}$ to $h_{\rm R} = H_{\rm R}/S_0$, which can be expressed in terms of rescaled reservoir operators, p_ω and x_ω where $p_\omega = P_\omega/\sqrt{S_0}$ and $x_\omega = X_\omega/\sqrt{S_0}$. The com-

mutation relations are then $[x_\omega, p_{\omega'}] = i\hbar\,\delta(\omega-\omega')/S_0$, so in the limit of $S_0 \to \infty$, these two operators commute [211]. Thus, the classical limit of the spin induces a limit for the reservoir. That is, the quantum nature of the reservoir is inevitably stripped away, so that the result eventually obtained is that of a classical spin coupled to a classical reservoir.

Written in terms of these rescaled reservoir operators, one now has,

$$e^{-\beta H_{\rm tot}} = \exp\left[-\beta'\left(-\omega_{\rm L}s_z + h_R + s_\theta\int_0^\infty \mathrm{d}\omega\, C_\omega\sqrt{S_0}\,x_\omega\right)\right]. \tag{85}$$

If one were to naively take the S_0-limit, then the interaction term dominates and the dependence on the bare system energy $-\omega_{\rm L}s_z$ drops out. To maintain a non-trivial dependence on both, bare and interaction energies, one needs to make an assumption on the scaling of the coupling function C_ω with spin-length S_0. We choose to keep the relative energy scales of the bare and interaction Hamiltonians the same throughout the S_0 limit. Eq. (85) shows that this requires a scaling of $C_\omega \propto 1/\sqrt{S_0}$. This implies a reorganisation energy (80) scaling of

$$Q = \alpha\frac{\omega_{\rm L}}{S_0}, \tag{86}$$

where α is a unit-free constant independent of S_0 and β. Inserted in the classical MF state (82) this shows that both, the system energy $H_{\rm S}$ as well as the correction that comes from the reservoir interaction, scale as S_0. The combined scaling of Q with S_0 (Eq. (86)), and the rescaling of the inverse temperature, $\beta S_0 = \beta' = \mathrm{const}$, then leaves the CMF state (82) invariant under variation of S_0.

Crucially, given the same scaling, the QMF state defined by Eq. (81) will not be invariant under variation of S_0. Returning to the unnormalised total Gibbs state (85), taking the quantum trace over the spin, and using Eq. (83), one obtains an identity that still contains the bath operators in contrast to the uncoupled spin. Finally taking the quantum trace over the reservoir on both sides, one finds

$$\lim_{S_0\to\infty}\frac{\hbar}{2S_0+\hbar}\frac{Z^{\rm qu}_{\rm SR}(\beta,S_0,\alpha)}{Z^{\rm qu}_{\rm R}(\beta)} = \lim_{S_0\to\infty}\frac{\hbar}{2S_0+\hbar}\tilde{Z}^{\rm qu}_{\rm S}(\beta,S_0,\alpha) = \tilde{Z}^{\rm cl}_{\rm S}(\beta S_0,\alpha). \tag{87}$$

Here it was used that the fraction of the total quantum partition function divided by the bare quantum reservoir partition function is the quantum mean force partition

function (see Appendix C.4) [212, 213]. In contrast to the quantum-classical correspondence established by Millard & Leff, and Lieb, for the standard Gibbs state partition functions, there now is a dependence on the spin-environment coupling strength α. For the classical case, one has $\tilde{Z}_{\mathrm{S}}^{\mathrm{cl}}(\beta S_0, \alpha) = \mathrm{tr}_{\mathrm{S}}^{\mathrm{cl}}[e^{-\beta S_0 (H_{\mathrm{S}}/S_0 - \alpha\, \omega_{\mathrm{L}} S_\theta^2/S_0^2)}]$.

While we derived Eq. (87) assuming a constant ratio between bare and interaction energy, i.e. $C_\omega \propto 1/\sqrt{S_0}$, the quantum-classical correspondence also holds for other scalings. Indeed, when $C_\omega \propto 1/\sqrt{S_0^p}$ with $p > 1$, the bare energy will grow much more rapidly than the interaction term in the limit $S_0 \to \infty$. This immediately leads to the ultraweak coupling limit where the known quantum-classical correspondence (83) applies. On the other hand, when $C_\omega \propto 1/\sqrt{S_0^p}$ with $0 \leq p < 1$, the interaction term will grow much more rapidly than the bare energy. As we show in Appendix C.7, in this ultrastrong limit [178], the quantum and classical mean force partition functions turn out to be identical. In this ultrastrong limit, the partition function loses all dependence on the coupling strength α. Thus, while (87) is valid for $p > 1$ and $0 \leq p < 1$, these scalings give a trivial correspondence, independent of α. Only for the scaling (86) is a dependence of the mean force partition functions on the coupling strength retained.

The results presented here show the quantum-classical correspondence of the equilibrium states of the spin-boson model for the first time. The proof of this correspondence, valid at all coupling strengths, is the second result of the section.

We remark that, in the above proof, it was assumed that α is independent of β. Physically this is not entirely accurate because the coupling C_ω is usually a function of temperature [214], albeit often a rather weak one. For the same limiting process to apply, a weak dependence on β would need to be compensated by an equally weak additional dependence of Q on S_0.

To visually illustrate the quantum to classical convergence, we choose a weak coupling strength, $\alpha = 0.06$, for which an analytical form of the quantum $\tilde{Z}_{\mathrm{S}}^{\mathrm{qu}}$ is known [178]. Mean force spin component expectation values $\langle s_k \rangle = \langle S_k \rangle_{\mathrm{MF}} / S_0$ for $k = x, z$ can then readily be computed from the partition functions $\tilde{Z}_{\mathrm{S}}^{\mathrm{qu}}$ and $\tilde{Z}_{\mathrm{S}}^{\mathrm{cl}}$, respectively. Fig. 14 shows $\langle s_z \rangle$ and $\langle s_x \rangle$ for various spin lengths, $S_0 = n\hbar/2$ with $n = 1, 2, 5, 1000$ for the quantum case (QMFWK, purple to green) and the classical case (CMF, dashed black). Note, that the x-axis is a correspondingly rescaled temperature, $2k_{\mathrm{B}}T/n\hbar\omega_{\mathrm{L}}$, a scaling under which the CMF remains invariant. The numerical results illustrate that the quantum $\langle s_z \rangle$ and $\langle s_x \rangle$ change with spin length

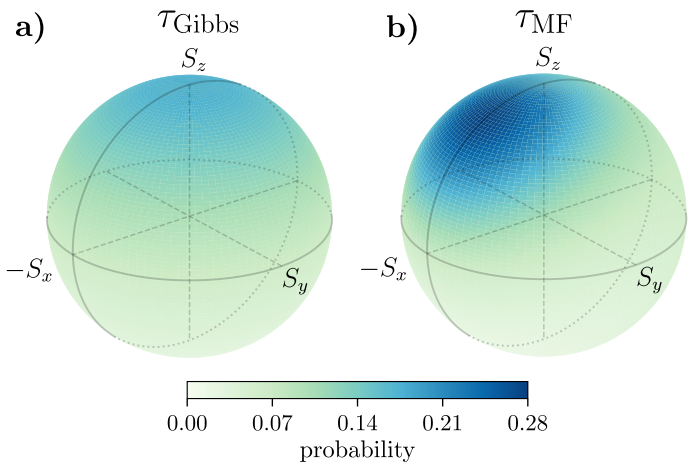

Figure 15: **Coherences and inhomogeneous probabilities.** Spin vector probability distributions (blue = high probability, white = low probability) as a function of three spin components on a sphere of radius S_0. **a)** The classical Gibbs state τ_{Gibbs} is a homogeneous function of H_{S}, i.e. it is constant over the energy shells of H_{S} which are fixed by the value of S_z. **b)** The classical mean force probability distribution τ_{MF} given in (82), peaks in a direction with positive components in $-S_x$ and S_z directions. This makes τ_{MF} an inhomogeneous probability distribution over the energy shells of H_{S}. Parameters for the plots: $\theta = \pi/4$, $k_{\mathrm{B}}T = S_0\omega_{\mathrm{L}}$, and $Q = \omega_{\mathrm{L}}/S_0$.

$S_0 = n\hbar/2$, and indeed converge to the classical prediction in the large spin limit, $n \to \infty$.

4.7 Coherences

As seen in Fig. 14 (right panel), the $\langle s_x \rangle$ spin-component in the quantum mean force state (solid purple line for spin-1/2) is non-zero at low temperatures, despite the fact that the bare system energy scale is set along the z-direction, see (76). Such non-zero $\langle s_x \rangle$ implies the presence of energetic "coherences" in the system's equilibrium state, as recently discussed in [179, 215] for a quantum spin-1/2. Considering the quantum–classical correspondence discussed above, a natural question is whether in the classical limit one can observe "decoherence", in the sense of vanishing coherences. However, comparing like with like, we see in Fig. 14 that "coherences" are also present for a classical spin with length $S_0 = \hbar/2$ (dashed black). Indeed, maybe surprisingly, classical "coherences" can be even larger in magnitude than those of a quantum spin with corresponding length S_0.

This observation reveals that the mechanism that gives rise to these coherences is not an intrinsically quantum one. Indeed, when we plot our CMF state (82)

in Fig. 15b), one can immediately see that the classical spin alignment in equilibrium tilts towards the $-S_x$ direction compared to the Gibbs state shown in Fig. 15a). Such 'inhomogenity' of a classical distribution has recently been identified by A. Smith, K. Sinha, C. Jarzynski [216] as the classical analogue to quantum coherences in the context of thermodynamic work extraction [217, 218]. Here we uncover that the mechanism of producing such classical coherences can be due to the nature of the environmental coupling, which is asymmetric with respect to the bare Hamiltonian, see Fig. 12. This third finding, that coherences can be present even in classical equilibrium states, will have implications on a variety of fields, including quantum thermodynamics and quantum biology, which have so far interpreted a non-zero value of $\langle s_x \rangle$ as a 'quantum signature'.

4.8 Coupling regimes

Finally, we now classify the interaction strength necessary for the spin-boson model to fall in various coupling regimes, from ultra-weak to ultra-strong. To quantify the relative strength of coupling we use the dimensionless parameter

$$\zeta = \frac{QS_0}{\omega_{\rm L}}, \tag{88}$$

which is the ratio of interaction and bare energy terms, see also Eq. (82). For the scaling choice (86), one has $\zeta = \alpha$. It's important to note that temperature sets another scale in this problem – higher temperatures will allow higher coupling values ζ to still fall within the "weak" coupling regime [178, 223]. Thus, we will first characterise various coupling regimes at $T = 0$ K, where the coupling has the most significant effect on the system equilibrium state, and then proceed to study finite temperatures.

Fig. 16a) and 16b) show the spin components $\langle s_z \rangle$ and $\langle s_x \rangle$ in the quantum MF state (QMF, solid dark blue) at $T = 0$ K. These expressions are evaluated numerically using the reaction coordinate method [219, 220, 221, 222] for $S_0 = \hbar/2$ and angle $\theta = \pi/4$. Also shown are the spin components for the quantum Gibbs state (QG, dashed green), for the quantum MF state in the weak coupling limit (QMFWK, dashed turquoise), and for the quantum MF state in the ultrastrong coupling limit (QMFUS, dashed grey) [178].

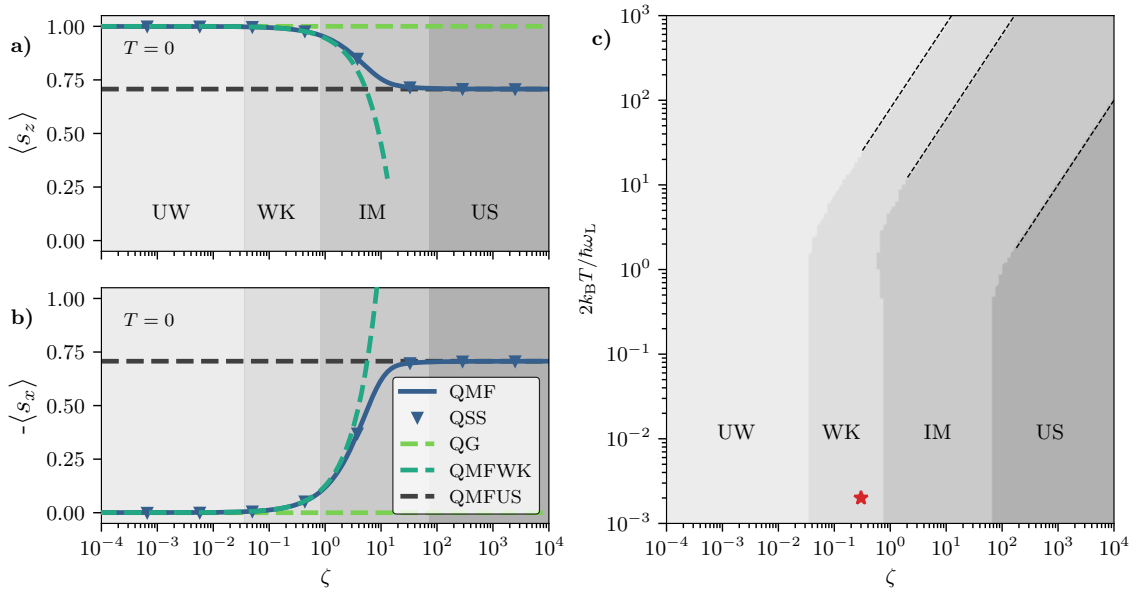

Figure 16: **Quantum coupling regimes at $T = 0$ and $T > 0$.** Panels **a)** and **b)**: Spin expectation values $\langle s_z \rangle$ and $-\langle s_x \rangle$ for the MF state (81) at $T = 0$ for the total Hamiltonian (78) with $S_0 = \hbar/2$, $\theta = \pi/4$ and different coupling strengths as quantified by the dimensionless parameter ζ, see (88). We identify four coupling regimes for the numerically exact QMF state (solid dark blue): Ultraweak coupling (UW), where the spin expectation values are consistent with the Gibbs state (QG, dashed light green); Weak coupling (WK), where the expectation values are well approximated by a second order expansion in ζ (QMFWK, dashed turquoise) [179]; Ultrastrong coupling (US), where the asymptotic limit of infinitely strong coupling $\zeta \to \infty$ is valid (QMFUS, dashed grey) [178], and Intermediate coupling (IM) where the QMF state is not approximated by any known analytical expression. The dynamical steady state of the quantum spin (QSS, dark blue triangles) is also computed using the reaction coordinate technique [219, 220, 221, 222]. Excellent agreement between the QSS and the QMF prediction is seen for all ζ. Panel **c)**: Coupling regimes as a function of temperature T and coupling strength ζ. With increasing temperature, the boundaries shift towards higher coupling ζ. At large temperatures, all three boundaries follow a linear relation $T \propto \zeta$ (dashed lines). The red star functions as a comparison with Fig. 17 and it is treated in its caption.

By comparing the analytical results (dashed lines) to the numerically exact result (solid line), and requiring the relative error to be at most $4 \cdot 10^{-3}$, we can clearly identify four regimes: For $\zeta < 4 \cdot 10^{-2}$, equilibrium is well-described by the quantum Gibbs state and this parameter regime can thus can be considered as ultraweak coupling (UW) [177]. For $4 \cdot 10^{-2} \leq \zeta < 8 \cdot 10^{-1}$, equilibrium is well-described by the weak coupling state QMFWK, which includes second order coupling corrections [178]. Thus, this regime is identified as the weak coupling regime (WK). At the other extreme, for $7 \cdot 10^{1} \leq \zeta$, the equilibrium state converges to the ultrastrong coupling state QMFUS which was derived in [178]. Thus, this

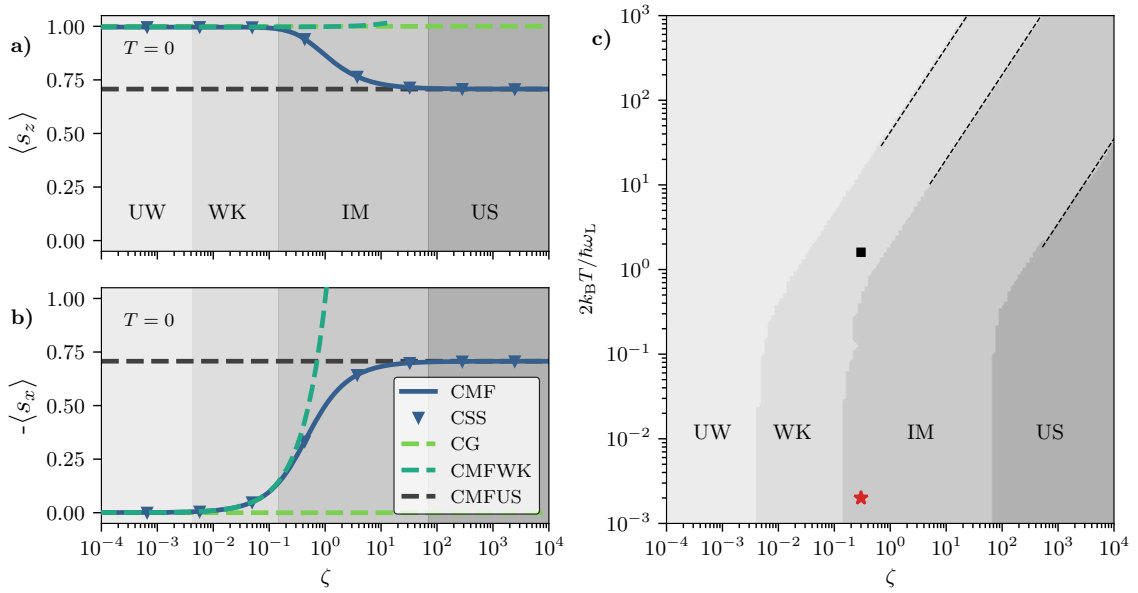

Figure 17: **Classical coupling regimes at $T = 0$ and $T > 0$.** Same plot as Fig. 16, but here for the equilibrium state of a *classical* spin vector $\mathbf{S}$ with Hamiltonian Eq. (78). A particular (T, ζ)-pair (red star) is identified for which the classical spin falls in the intermediate regime. For the same parameter pair, the *quantum* spin falls in the weak coupling regime, see red star in Fig. 16c). Moving the classical red star upwards in temperature until it reaches a point (black square) in the weak coupling regime that is laterally distanced from the boundaries similar to the quantum star, Fig. 16c), gives an effective temperature shift of $\Delta T = 1.6 \cdot 2\hbar\omega_{\mathrm{L}}/k_{\mathrm{B}}$. This example evidences significant differences between the environmental impact on quantum and classical equilibrium states.

regime is identified as the ultrastrong coupling regime (US). Finally, for the parameter regime $8 \cdot 10^{-1} \leq \zeta < 7 \cdot 10^{1}$ the exact QMF shows variation with ζ that is not captured by neither weak nor ultrastrong coupling approximation. This is the intermediate coupling regime (IM), which is highly relevant from an experimental point of view, but there are no known analytical expressions that approximate the numerically exact QMF [203].

Beyond the zero temperature case, we compute $\langle s_x \rangle$ and $\langle s_z \rangle$ with the numerically exact QMF state over a wide range of coupling strengths and temperatures, and compare the results with those of the UW, WK, and US approximations allowing an error of $4 \cdot 10^{-3}$, as above. Fig. 16c) shows how pairs of ζ and T fall into various coupling regimes. One can see that, at elevated temperatures, the coupling regime boundaries shift towards higher coupling ζ. Thus at higher temperatures, $2k_{\mathrm{B}}T/\hbar\omega_{\mathrm{L}} \gtrsim 10$, the UW and WK approximations are valid at much higher coupling strengths ζ than at $T = 0$. At higher temperatures we also observe an emerging linear relation, $2k_{\mathrm{B}}T/\hbar\omega_{\mathrm{L}} \propto \zeta$, for all three regime boundaries.

The temperature dependence of the border between the weak and intermediate coupling regime has previously been identified to be linear by C. Latune [223].

The quantum coupling regimes can now be compared to the corresponding regimes for a classical spin vector, shown in Fig. 17a-c). Perhaps surprisingly, we find that the classical regime boundary values for ζ differ significantly from those for the quantum spin, e.g., by a factor of 10 for the WK approximation. This shift is exemplified by the red star, which indicates the same parameter pair (T, ζ) in both figures, Figs. 16c) and 17c). While the open quantum spin lies in the weak coupling regime, the classical one requires an intermediate coupling treatment. We suspect this quantum-classical distinctness comes from the fact that, while for a classical spin at zero temperature there is no noise induced by the bath, in the quantum case noise is present even at $T = 0$ K due to the bath's zero-point-fluctuations [145]. One may qualitatively interpret this additional noise as an effective temperature shift with respect to the classical case, by ca. $\Delta T = 1.6 \cdot 2\hbar\omega_{\mathrm{L}}/k_{\mathrm{B}}$, as indicated by the black square in Fig. 17c).

To conclude, for any given coupling value ζ and temperature T, the two plots Fig. 16c) and Fig. 17c) provide a tool to judge whether a "weak coupling" approximation is valid for the spin-boson model or not. We emphasise that, interestingly, the answer depends on whether one considers a quantum or a classical spin.

4.9 Conclusion

In this section we have characterised the equilibrium properties of the θ–angled spin-boson model, in the quantum and classical regime.

Firstly, for the classical case, we have derived a compact analytical expression for the equilibrium state of the spin, that is valid for arbitrary coupling to the harmonic reservoir. This is of great practical relevance as it allows one to analytically obtain all equilibrium properties of the spin at any coupling strength. It remains an open question [177] to find a similarly general analytical expressions for the quantum case.

Secondly, we have proved that the quantum MF partition function, including environmental terms, converges to its classical counterpart in the large-spin limit at all coupling strengths. Our results provide direct insight into the difference between quantum and classical states of a spin coupled to a noisy environment.

Apart from being of purely fundamental interest, this will constitute key information for many quantum technologies [224], and ultimately links to the quantum supremacy debate.

Third, a large and growing body of literature identifies coherences as quantum signatures and attributes speed-ups (e.g. in quantum computing and quantum biology) or efficiency gains (e.g. in quantum thermodynamics) to quantum coherences. Here, we demonstrated that even the equilibrium states of classical open spins host 'coherences' when the environment couples asymmetrically. Thus, measures other than 'coherences' may be required to certify the quantum origin of certain speed-ups or efficiency improvements in the future.

Finally, we presented the first quantitative characterisation of the coupling parameter values that put the spin-boson model in the ultraweak, weak, intermediate, or ultrastrong coupling regime, both for the quantum case as well as the classical setting. This classification will be important in many future studies of the spin-boson model, quantum or classical, for which it provides the tool to chose the correct approximation for a specific parameter set.

Code availability

The code to obtain the classical steady–state curves is available online in the form of official Julia package at https://github.com/quantum-exeter/SpiDy.jl. This is also the subject of the next section. The code used to produce Fig. 16 and Fig. 17 is publicly available online at https://github.com/quantum-exeter/SpinMFGS. It can be used to make analogous plots for a desired coupling angle θ and spin length S_0.

5 SpiDy.jl: open–source Julia package for the study of non–Markovian stochastic dynamics

5.1 Statement of contribution

In the following work, I devised the idea for a standalone Julia package rebuilding and extending the code written for the work in Ref. [145]. I have written this package together with Federico Cerisola. Federico had several clever ideas to boost the code efficiency. The entire coding process has been a symbiotic work, while often I would take the burden of writing some trivial but necessary lines. I have written the Julia notebook to guide the user through the pieces of the code and the brief paper for the package. Federico contributed and polished both notebooks and paper. The entire code and git history is available on GitHub at https://github.com/quantum-exeter/SpiDy.jl.

5.2 Summary

SpiDy.jl solves the non–Markovian stochastic dynamics of interacting classical spin lattices and harmonic oscillators networks. The methods implemented allow the user to include arbitrary memory effects and colored noise spectra. We provide the user with Julia notebooks to guide them through the various mathematical constructions and simulations. The field of applicability for SpiDy.jl is vast, allowing for the study of multi–dimensional anisotropic system-bath interactions, spectral densities, noise, and temperature effects. Some examples range from atomistic spin dynamics to ultrafast magnetism and anisotropic materials.

5.3 Introduction

Modeling the dynamics of spins at low temperatures and at short timescales is a fundamental task to address many open questions in the field of magnetism and magnetic material modeling [225]. State-of-the-art tools such as those developed for atomistic spin dynamics simulations are based on solving the Landau–Lifshitz–Gilbert (LLG) equation [155]. Despite their massive success, these tools run into shortcomings in accurately modeling systems at low temperatures and for short timescales where environment memory effects have been observed

[190, 226]. Recent work has focused on developing a comprehensive quantum thermodynamically consistent framework suitable to model the dynamics of spins in magnetic materials while addressing these shortcomings [145]. This framework includes strong coupling effects to the environment such as non-Markovian memory, colored noise, and quantum-like fluctuations. At its core, SpiDy.jl implements the theoretical framework introduced in Ref. [145], allowing for the study of environment memory effects and anisotropic system-environment coupling. SpiDy.jl can be readily adopted for atomistic spin dynamics simulations [155, 157], ultrafast magnetism [227], and ferromagnetic and semiconductive systems exhibiting anisotropic damping [228]. A further set of applications stems from the extension of SpiDy.jl to handle the non-Markovian stochastic dynamics of harmonic oscillators. This model might be of interest in the field of quantum thermodynamics where harmonic oscillators play a key role in the environment modelling. The package is written in pure Julia to take advantage of the language performance.

The software package has seen a wide range of applications to date. Firstly, the convenience of three independent environments in SpiDy.jl finds application in the microscopic modelling of spins affected by noise due to vibrations of the material lattice [145]. SpiDy.jl also found application in the demonstration of the quantum-to-classical correspondence at all coupling strengths between a spin and an external environment [229]. Here, the temperature dependence of the spin steady-state magnetization obtained with SpiDy.jl is successfully compared with the classical mean force state of the system. In Ref. [230], the authors take advantage of the customizable coupling tensor in SpiDy.jl to explore the anisotropic effects of the environment onto the system. In Ref. [231], SpiDy.jl is used as a sub-routine to build quantum-improved atomistic spin dynamics simulations. In the paper, the authors take advantage of the customizable power spectrum to implement ad-hoc simulations matching known experimental results. Lastly, with an eye to the harmonic oscillator side, SpiDy.jl is used to match the quantum harmonic oscillator dynamics with its stochastic counterpart [232]. Here, the authors exploit the recent implementation of harmonic oscillator dynamics.

5.4 Overview

To model a system of interacting classical spin vectors, SpiDy.jl solves the generalized stochastic LLG equation [145]

$$\frac{\mathrm{d}\mathbf{S}_n(t)}{\mathrm{d}t} = \frac{1}{2}\mathbf{S}_n(t) \times \left[\sum_{m \neq n} J_{n,m}\mathbf{S}_m(t) + \mathbf{B} + \mathbf{b}_n(t) + \int_{t_0}^{t} \mathrm{d}t' K_n(t-t')\mathbf{S}_n(t') \right], \quad (89)$$

where $\mathbf{S}_n(t)$ represents the n-th spin vector, the interaction matrix $J_{n,m}$ sets the interaction strength between the n-th and m-th spins, $\mathbf{B}$ is the external field, which determines the natural precession direction and frequency of the spins in the absence of interaction, and $b_n(t)$ is the time-dependent stochastic field interacting with the spin. Finally, the last integral term in Eq. (89) takes care of the spin dissipation due to the environment, including non-Markovian effects accounted for by the memory kernel matrix $K_n(t)$. Note that, while the term $b_n(t)$ reflects the color of the noise and eventual zero–point fluctuations, the integral term introduces the damping on the spins and the geometry of their coupling to the environment. Here, we allow each spin to interact with three independent sources of noise, so that in general $K_n(t) = C_n k_n(t)$, where $k_n(t)$ is a time dependent function and C_n is a 3×3 matrix that determines how each of the n-th spin components couples to each of the three noise sources. To efficiently simulate the non-Markovian effects, we follow the methods explained in [145] and restrict ourselves to the case where the memory kernel $k(t)$ comes from a Lorentzian spectral density of the bath $\mathscr{J}(\omega) = \alpha\Gamma/((\omega_0^2 - \omega^2)^2 + \Gamma^2\omega^2)$ with peak frequency ω_0, peak width Γ and amplitude α, so that $k(t) = \Theta(t)\,\alpha\, e^{-\Gamma t/2}\sin(\omega_1 t)/\omega_1$, where $\omega_1^2 = \omega_0^2 - \Gamma^2/4$. In the code, the stochastic noise $b_n(t)$ is generated so that it satisfies the fluctuation-dissipation relation (FDR) (see Ref. [145]). That is, the power spectral density of the stochastic noise satisfies $P(\omega, T) = \mathscr{J}(\omega)\eta(T)$ where $\mathscr{J}(\omega)$ is the Lorentzian spectral density and $\eta(T)$ defines the temperature dependence on the bath. Here, the user can choose, among others, a classical or quantum-like temperature dependence, namely $\eta_{\mathrm{cl}}(T) = k_{\mathrm{B}}T/2\hbar\omega$ and $\eta_{\mathrm{qu}}(T) = \coth(2\hbar\omega/k_{\mathrm{B}}T)$ respectively.

In addition, SpiDy.jl also allows one to study the stochastic dynamics of coupled harmonic oscillator networks. In the same way, as for the spin case, the harmonic oscillators can be coupled together with a user-defined system-system

interaction. The equations of motion solved in this case are

$$\frac{\mathrm{d}^2\mathbf{X}_n(t)}{\mathrm{d}t^2} = \sum_{m\neq n} J_{n,m}\mathbf{X}_m(t) - \Omega^2\mathbf{X}_n(t) + \mathbf{b}_n(t) + \int_{t_0}^{t} \mathrm{d}t' K_n(t-t')\mathbf{X}_n(t'), \tag{90}$$

where $\mathbf{X}_n(t)$ represents the position vector of the n-th harmonic oscillator, the interaction matrix $J_{n,m}$ sets the interaction strength between the n-th and m-th harmonic oscillators, and Ω is the bare frequency of the harmonic oscillators (we consider identical oscillators). All other terms have the same role as in the spin case (see Eq. (89)).

In conclusion, SpiDy.jl implements the stochastic dynamics of coupled integro-differential equations to model systems of interacting spins or harmonic oscillator networks subject to environment noise. Among other, some of the key features of the package include:

- Coloured stochastic noise that satisfies the FDR and accounts for both classical and quantum bath statistics.
- Simulation of non-Markovian system dynamics due to the coloured noise.
- Custom system-environment coupling tensors, allowing for isotropic or anisotropic couplings. Both amplitudes and geometry of the coupling can be specified.
- Choice between local environments, i.e. distinct baths acting on the single sub-system, or a single common environment.
- System-system coupling for the interactions between sub-systems.

5.5 Example

Now, we show an example code to generate a run of SpiDy.jl for the spin dynamics case. Given the stochastic nature of the problem solved, we will be dealing with different dynamical trajectories. In the following code, we set the parameters needed to build these trajectories, solutions to the stochastic set of equations and plot a single one of them as an example. The entire code is commented throughout for a better understanding of the single elements of the run. We show the results of the dynamics averaged over the full set (10000) of trajectories in Fig. 18.

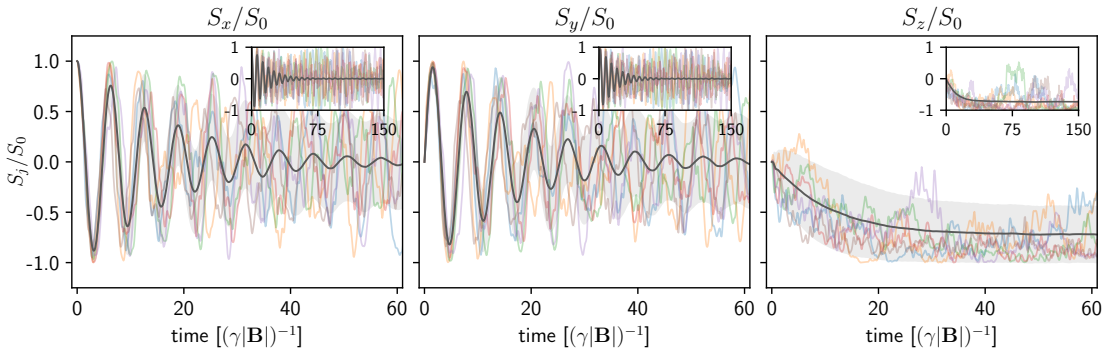

Figure 18: **Simulation results for the single-spin dynamics.** Dynamics of the x, y, and z components of the spin. The components are normalized against the total spin length S_0. We show an example set of 5 stochastic trajectories of the spin dynamics (colored semi-transparent lines) together with their stochastic average (gray solid line). Note that, while we show only 5 trajectories for clarity, the average dynamics is obtained from 10000 trajectories. We also represent the area of dynamics included within a standard deviation of the average dynamics (gray-shaded area). In the inset, we show the convergence of the same dynamics towards the steady state at longer times. This example is obtained using the Lorentzian parameters "set 1" found in Ref. [145]. The code used to generate the stochastic trajectories is shown in the main text.

Note that both the average and the standard deviation of the set of trajectories are not evaluated with the following code but are nonetheless represented in the figure for clarity.

```
### importing SpiDy ###
using SpiDy

### setting the parameters ###
Δt = 0.1 # time step for the dynamics evaluation
Tend = 150 # final time of the dynamics
N = round(Int, Tend/Δt) # number of total steps
tspan = (0, N*Δt) # tuple of initial and final time
saveat = (0:1:N)*Δt # vector of times at which the solution is saved
α = 10 # Lorentzian coupling amplitude
ω0 = 7 # Lorentzian resonant frequency
Γ = 5 # Lorentzian width
Jsd = LorentzianSD(α, ω0, Γ) # Lorentzian spectral density
Cw = IsoCoupling(1) # isotropic coupling tensor
# the resulting coupling tensor is equivalent to the following
# Cw = AnisoCoupling([1 0 0
```

```
#                       0 1 0
#                       0 0 1]);
T = 0.8 # temperature at which the dynamics takes place
noise = ClassicalNoise(T) # noise profile for the stochastic field
s0 = [1.0; 0.0; 0.0] # initial conditions of the spin vector for the
    dynamics
ntraj = 10000 # number of trajectories (stochastic realizations)

### running the dynamics ###
sols = zeros(ntraj, 3, length(saveat)) # solution matrix
for i in 1:ntraj # iterations through the number of trajectories
    # we use the Lorentzian spectral density Jsd to generate the
       stochastic
    # field. This assures the field obeys the FDR as noted in the main
       text
    local bfields = [bfield(N, Δt, Jsd, noise),
                     bfield(N, Δt, Jsd, noise), # vector of independent
                     bfield(N, Δt, Jsd, noise)] # stochastic fields
    # diffeqsolver (below) solves the system for the single trajectory
    local sol = diffeqsolver(s0, tspan, Jsd, bfields, Cw; saveat=saveat)
    sols[i,:,:] = sol[:,:] # store the trajectory into the matrix of
       solutions
end

### example plot ###
# use Plots.jl pkg to plot a single trajectory of the dynamics over time
using Plots
plot(xlabel="time", ylabel="spin components")
# sols[i,j,k] with i: trajectory index, j: spin component, k: solution
    at
# the k-th time point
plot!(saveat, sols[1,1,:], label="x-component")
plot!(saveat, sols[1,2,:], label="y-component")
plot!(saveat, sols[1,3,:], label="z-component")
savefig("example_run.pdf")
```

6 Discussion

In this thesis, we have journeyed through some aspects of open systems, quantum and classical. To do so, we have touched fields going from classical wave scattering theories, to quantum master equations and beyond-LLG theories. We have adopted tools of increasing popularity like graph theory to explore the exceptional points of classical systems. We have uncovered the caveats of approximations in quantum master equations, again, exploiting physical features in the form of EPs. We have expanded theories to go beyond the prediction of the LLG equation to explain the spin dynamics at low temperature. In the process, we have developed an entire package to explore the stochastic equations of the spin-boson model and harmonic oscillators.

Here, I recap on a few key points about the conclusions drawn in the previous sections and propose a few possible further research directions.

Graph theory approach to exceptional points in wave scattering

- In section 2, I developed a diagrammatic method to understand multiple scattering processes using graph theory and used this to find the exceptional points of the system.
- The scattering events are understood via 1–connections and subdigraphs, allowing for approximation in weakly and strongly coupled systems.
- The Frobenius companion matrix gives a general formula to find the zero eigenvalue exceptional points (EPs) of the system considered.
- It is possible to control the spectral width of the power response at an EP, indicating an interplay between the gain/loss of the scatterers and the power output.

Several future directions and possible studies can stem from here. First of all, linking graph theory with wave scattering systems allows to port numerical tools from one world to the other. For example, this might help in the development of alternative and more efficient search routines in parameter space. Another interesting direction would be to explore less approximated theories (in this case, the discrete dipole approximation), considering scatterers with a non–trivial form

factor and see if any diagrammatic interpretation remains. It would also be interesting to expand the graph theoretical treatment of wave scattering events to find EPs not associated to zero eigenvalues. To do so, one would need to study the EPs conditions derived from the block companion matrices rather then the full Frobenius matrix [52]. In addition, one could represent the companion matrices themselves via Coates digraphs in search for even more insightful interpretations for the EPs conditions [38]. On a more experimental side, it would be possible to explore the implication of these findings in settings relevant for coherent perfect absorption (CPA) [60, 61], in which zero eigenvalue EPs play a crucial role.

Local master equations bypass the secular approximation

- In section 3, I focused on modeling the dynamics and heat flows across two coupled harmonic oscillators interacting with external baths using quantum master equations.
- The local and global master equations, two common approaches, can yield very different predictions.
- The local master equation (LME) captured dynamical features that the global master equation (GME) missed. We identified the breakdown of the GME predictive capabilities in the secular approximation.
- The LME directly derives from the Redfield equation in the limit of vanishing inter–node coupling. In this regime, the LME bypasses the secular approximation and maintains its predictive accuracy.
- The LME can be superior to the GME in the presence of weak internal coupling and offers a computationally less demanding alternative to the Redfield equation.
- In a regime where both LME and GME are valid, modeling using the local approach can also make a significant difference in the prediction of heat transfer in quantum thermal machines.

From these findings, one might be interested in the understanding of discrete rather than continuous variable systems in the direction of Ref. [233]. Would this lack of physicality of the global master equation remain valid in the discrete case?

In fact, nowadays, a deeper understanding of the limiting cases of approximation and applicability of the local and global master equation remains desirable. As we have seen in this section, performing approximations, e.g. the secular approximation, have profound consequences on the thermodynamics of the system. It would be key to know if other physical features, other than the EPs, are affected by such approximations.

Quantum-classical correspondence in spin-boson equilibrium states at arbitrary coupling

- In section 4, I explored the equilibrium properties of the θ-angled spin-boson model in both quantum and classical regimes.
- A compact analytical expression was derived for the equilibrium state of the spin in the classical case, which is universally applicable for any coupling strength.
- A comparison between quantum and classical states of a spin coupled to a noisy environment was discussed, providing insights into the quantum vs. classical debate.
- Even classical open spins at equilibrium can showcase an equivalent of quantum coherences when the environment is coupled asymmetrically. This suggests the need for alternative measures of quantum coherences to certify the quantum origin of certain speed-ups or efficiencies.
- A quantitative characterization of the coupling parameter values was presented, which will be a benchmark for future studies of the spin-boson model.

Different possible directions can emerge from this work. First of all, while we have found an analytical expression for the equilibrium state of the spin at arbitrary coupling with the environment, a quantum equivalent is yet to be derived [177]. From a quantum thermodynamic perspective, these contributions are of interest for the development of quantum hardware and technologies [224]. In fact, a link can be further drawn between the thermodynamics of a qubit and its quickest channel of dissipation to the environment. This happens at an EP and it is crucial

for qubit resetting in quantum computing [67]. It would also be interesting to explore further the link between the quantum coherences at zero temperature and their classical equivalent found in the case of asymmetric coupling to the environment.

SpiDy.jl: open–source Julia package for the study of non–Markovian stochastic dynamics

- In section 5, I have introduced SpiDy.jl, a comprehensive Julia package designed to simulate the stochastic dynamics of the spin-boson model and harmonic oscillators.
- A key feature is the possibility to choose a noise power spectrum between classical, quantum, and quantum without zero–point fluctuations. This allows for reasonable comparison with predictions obtained from semi–classical and quantum models.
- The package offers the possibility to tune the noise distribution profile by supporting external packages like Distributions.jl.
- An explicit and customizable coupling tensor allows the user to study specific configurations and geometries of the system–bath coupling.
- The addition of a system–system coupling matrix further enhance the exploration capabilities.
- The design of the package ensures modularity and extensibility, allowing it to adapt to various physical models and experimental setups.

SpiDy.jl provides a robust computational addition for the spin dynamics community and for the study of non–trivial systems of harmonic oscillator. Crucial here is the possibility to tune a non–Markovian colored stochastic noise. Given its flexibility and adaptability, future work could involve extending its capabilities to handle more specialized spectral densities or introducing more efficient algorithms for larger scale simulations. A collaborative effort with experimentalists could also improve the prediction capabilities of the package, optimizing it based on feedback and real-world testing.

To conclude, we have seen how opening the (quantum or classical) system to an external environment hides dynamical and thermodynamic peculiarities and unexpected behaviours. As hinted in this conclusive section, the subject is so vast that every little contribution to the field generates a plethora of further topics one could explore. There is still extensive work to be done but open system theory has unparalleled potential for multidisciplinarity, thus the fun is unlikely to end soon.

A Graph theory in wave scattering

A.1 Graph theory fundamentals

"A graph $\mathscr{G}$ is an ordered pair of disjoint sets $(\mathscr{V}, \mathscr{E})$, such that $\mathscr{E}$ is a subset of unordered pairs of $\mathscr{V}$" [40]. The set $\mathscr{V}$ defines the vertices of the graph, i.e., the interacting elements of a structure we consider. The interactions between these elements are defined by the edges in the set $\mathscr{E}$. In the case of interacting discrete scatterers, the set of vertices $\mathscr{V}$ represents the set of scatterers and the set of edges $\mathscr{E}$ correspond to the set of interactions between the scatterers. Note that, in general, these interactions are not symmetric. By means of these fundamental blocks, we can translate every matrix $\boldsymbol{M}$ of the form Eq. (11) into a graph of the form 5. The resulting graph will represent the polarizabilities α as self–loops (or self–edges) and the Green's functions $G(\boldsymbol{x}_i, \boldsymbol{x}_j)$ as edges starting from the vertex i and ending in the vertex j. This directed edges, from i to j, promote the graph to a directed–graph or digraph. As mentioned in the main text, this graph is the Coates digraph $D^*(\boldsymbol{M})$ associated with the matrix $\boldsymbol{M}$. Note that the asterisk superscript takes care of the historical definition of the Coates digraph, i.e., the digraph associated with the transpose of the matrix we intend to represent [37, 38]. In the main text, we refer to this kind of graphs as *vertex–labeled directed weighted simple graph permitting loops*. "Vertex–labeled", as the name suggests, indicates that the scatterers are distinguishable, "directed" means that interactions between scatterers are not necessarily symmetric, "weighted" indicates a non–unit interaction, "simple" indicates the presence of a single directional interaction between edges, while "permitting loops" identifies a graph that allows for self–interaction, in our case, the polarizabilities.

A.1.1 Linear subdigraphs

Consider the Coates' determinant formula in Eq. (13), expression for the construction of determinants by means of graphs. We report the expression here for convenience,

$$\det(\boldsymbol{A}) = (-1)^N \sum_{L \in \mathscr{L}(\boldsymbol{A})} (-1)^{c(L)} \gamma(L). \tag{A.1}$$

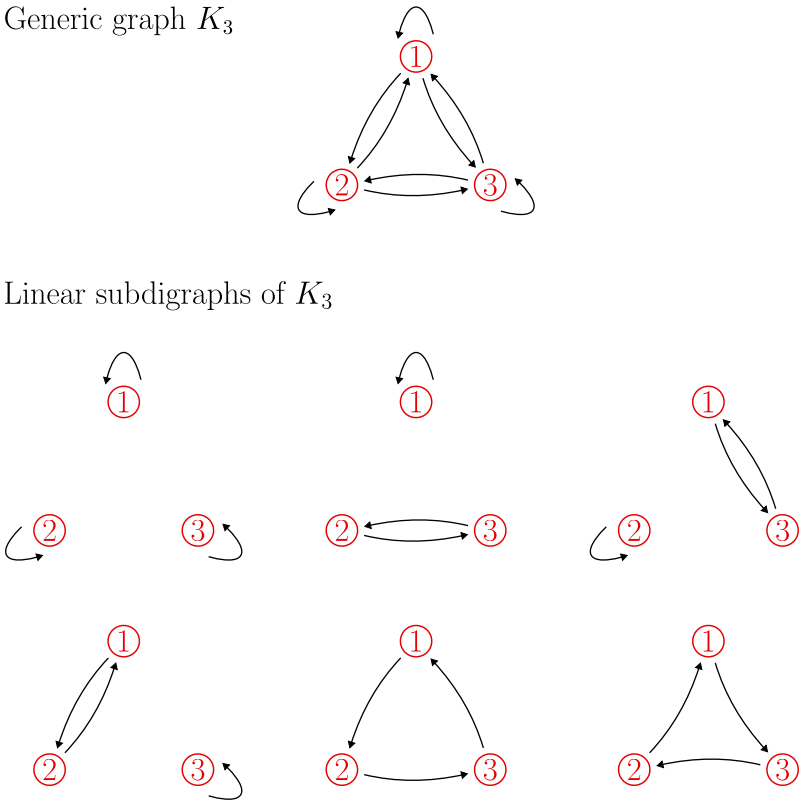

Figure 19: Example of linear subdigraphs associated with the graph K_3. For the example graph K_3, there are 6 linear subdigraphs in total. Note that, given that we deal with directed graphs, we distinguish between subdigraphs with edges linking the same nodes but in opposite directions as in the case of the last and second–to–last subdigraphs in the figure.

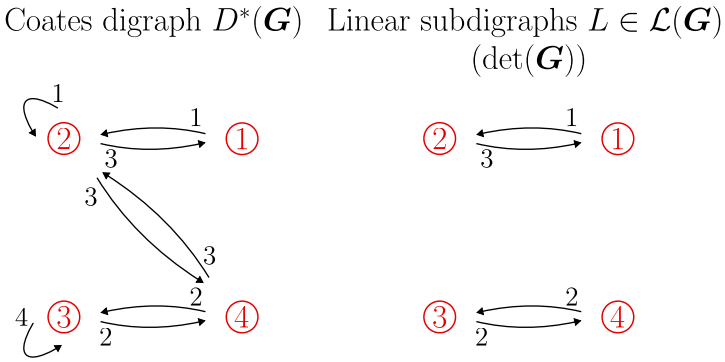

Figure 20: Construction of the determinant of the matrix $\boldsymbol{G}$. On the left, the Coates digraph of the matrix $\boldsymbol{G}$. On the right, the linear subdigraphs of the matrix $\boldsymbol{G}$ which define the determinant as per Eq. (13).

As a reminder, N is the dimension of a generic matrix $\boldsymbol{A}$ whose determinant we want to evaluate, $c(L)$ is the number of cycles in L, $\gamma(L)$ is the weight of the linear subdigraph L, and $\mathscr{L}(\boldsymbol{A})$ is the set of all possible linear subdigraphs of the Coates digraph $D^*(\boldsymbol{A})$. We now show what a linear subdigraphs is and how to construct it.

A subdigraph is a digraph with $\mathscr{V}' \subset \mathscr{V}$ vertices and $\mathscr{E}' \subset \mathscr{E}$ edges. In addition, to earn the name of linear subdigraph, the vertices in V' must have in–degree and out–degree equal to 1, i.e., every vertex must have exactly one edge entering and one edge leaving. In Fig. 19, we report the entire set of linear subdigraphs for an example digraph $\mathscr{K}_3$. In the main text, we use these set of graphs to construct the determinants in the adjugate inversion formula. We now show how we use these linear subdigraph constructions for the determinant evaluation. Consider the sparse matrix $\boldsymbol{G}$,

$$\boldsymbol{G} = \begin{pmatrix} 0 & 1 & 0 & 0 \\ 3 & 1 & 0 & 3 \\ 0 & 0 & 4 & 2 \\ 0 & 3 & 2 & 0 \end{pmatrix}. \tag{A.2}$$

We can work out the digraph associated with the matrix $\boldsymbol{G}$ and its linear subdigraphs to evaluate the determinant. To do this, we use Eq. (13), i.e., we search for all the subdigraphs whose vertices have in–degree and out–degree equal to 1. We show the results in Fig. 20, where on the LHS we find the digraph $D^*(\boldsymbol{G})$ associated with the matrix $\boldsymbol{G}$ and on the RHS we find the determinant of $\boldsymbol{G}$, consisting of the only linear subdigraph of the graph $D^*(\boldsymbol{G})$. Summing the weights of the edges of the subdigraph, we obtain the determinant, $\det(\boldsymbol{G}) = (-1)^4(-1)^2(1 \cdot 3 \cdot 2 \cdot 2) = 12$, where the first term accounts for the factor $(-1)^N$, the second term accounts for the number of cycles $(-1)^{c(L)}$, and the last accounts for the weights of the subdigraphs $\gamma(L)$.

A.1.2 1–connections

Consider the adjugate expression in Eq. (14), expression for the construction of adjugate terms by means of graphs. We report the expression here for conve-

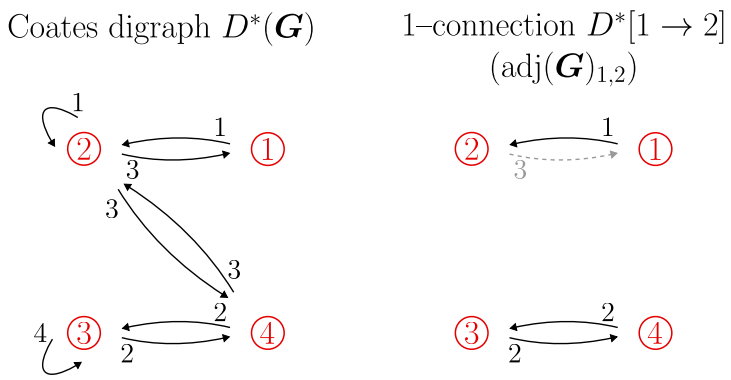

Figure 21: Construction of the adjugate element $\mathrm{adj}(\boldsymbol{G})_{1,2}$, built using the off–diagonal 1–connections from vertex 1 to vertex 2. On the left, again the Coates digraph of the matrix $\boldsymbol{G}$. On the right, the 1–connections of the matrix $\boldsymbol{G}$ which define the adjugate term $\mathrm{adj}(\boldsymbol{G})_{1,2}$ as per Eq. (14). The latter is built by the corresponding linear subdigraphs by removing the edge $2 \to 1$ as described in the text.

nience,

$$\mathrm{adj}(\boldsymbol{A})_{i,j} = (-1)^N \sum_{D^*[i \to j]} (-1)^{c(D^*[i \to j])+1} \gamma(D^*[i \to j]). \tag{A.3}$$

In this expression, the terms $D^*[i \to j]$ are the 1–connections from vertex i to vertex j while all the other elements of the equation have an analogous meaning as in the determinant expression. The 1–connection $D^*[i \to j]$ is obtained from the corresponding linear subdigraph $L_{\ni i \to j}$ (linear subdigraph that includes the edge $i \to j$) by simply removing the edge $j \to i$. Note that, in the case $i = j$, this corresponds to removing the self–loop at vertex i. This definition leads to the following relation between the number of cycles in a linear subdigraph $L_{\ni i \to j}$ and the relative 1–connection $D^*[i \to j]$ [38],

$$c(L_{\ni i \to j}) = c(D^*[i \to j]) + 1, \tag{A.4}$$

which justifies the "$+1$" in the adjugate expression. More formally, following the definition of a 1–connection reported in Ref. [38], we call 1–connection from vertex i to vertex j, the spanning subdigraph $D^*[i \to j]$ such that,

- for $i \neq j$, all vertices k with $k \neq i, j$ must have in–degree and out–degree equal to 1, vertex i must have in–degree equal to 0 but out–degree equal to 1 and vertex j must have in–degree equal to 1 but out–degree equal to 0. The resulting spanning subdigraph therefore has a path from vertex i to vertex j,

- for $i = j$, all vertices must have in–degree and out–degree equal to 1, while vertex $i = j$ must have in–degree and out–degree equal to 0.

As mentioned in the main text, the 1–connections are closely related to the linear subdigraphs. In fact, the 1–connections $D^*[i \to j]$ obtained using the definition above are equivalent to those obtained from the corresponding linear subdigraph $L_{\ni i \to j}$ simply by removing the edge $j \to i$. By means of this definition, we now show the construction of an off–diagonal adjugate term. Consider again the matrix $\boldsymbol{G}$, we now build the adjugate term $\text{adj}(\boldsymbol{G})_{1,2}$ consisting of the 1–connections $D^*[1 \to 2]$. To do this, we consider all the linear subdigraphs that include the edge $1 \to 2$ (one single subdigraph in our example) and remove the edge from vertex $2 \to 1$, as shown in Fig. 21. Summing the weights of the edges of the 1–connections, we obtain the adjugate term, $\text{adj}(\boldsymbol{G})_{1,2} = (-1)^4(-1)^{1+1}(1 \cdot 2 \cdot 2) = 4$, where the first term accounts for the factor $(-1)^N$, the second term accounts for the number of cycles $(-1)^{c(D^*[i \to j])+1}$, and the last accounts for the weights of the 1–connections $\gamma(D^*[i \to j])$.

A.2 Similarity transformation between a matrix and its Frobenius companion form

Consider a matrix $\boldsymbol{A} \in \mathbb{C}^{N \times N}$ and its Frobenius companion matrix (see Eq. 17 in the main text),

$$\boldsymbol{A}_{\text{Frob}} = \begin{pmatrix} 0 & 1 & 0 & \cdots & 0 & 0 \\ 0 & 0 & 1 & \cdots & 0 & 0 \\ \vdots & \vdots & \vdots & \ddots & \vdots & \vdots \\ 0 & 0 & 0 & \cdots & 1 & 0 \\ 0 & 0 & 0 & \cdots & 0 & 1 \\ -c_0 & -c_1 & -c_2 & \cdots & -c_{N-2} & -c_{N-1} \end{pmatrix}, \tag{A.5}$$

where c_i are the coefficients of the characteristic polynomial of $\boldsymbol{A}$. If there exists a row vector $\boldsymbol{b} \in \mathbb{C}^{1\times N}$ such that the matrix

$$\boldsymbol{T} = \begin{pmatrix} \boldsymbol{b} \\ \boldsymbol{bA} \\ \vdots \\ \boldsymbol{bA}^{N-2} \\ \boldsymbol{bA}^{N-1} \end{pmatrix} \in \mathbb{C}^{N\times N} \tag{A.6}$$

is non-singular, then the matrix $\boldsymbol{A}$ is similar to its Frobenius companion matrix $\boldsymbol{A}_{\text{Frob}}$ [52],

$$\boldsymbol{A}_{\text{Frob}} = \boldsymbol{T}^{-1}\boldsymbol{A}\boldsymbol{T}. \tag{A.7}$$

Here, the matrix $\boldsymbol{T}$ is the Vandermonde matrix, whose entries are thus given by

$$\boldsymbol{T}_{ij} = \boldsymbol{b}\boldsymbol{A}^{i-1}_{:,j}, \tag{A.8}$$

where $\boldsymbol{A}^{i-1}_{:,j}$ denotes the j-th column of $\boldsymbol{A}^{i-1}$. Note that, in what follows, we do not compute the vector $\boldsymbol{b}$ but rather we infer the transformation matrix $\boldsymbol{T}$ while keeping $\boldsymbol{b}$ implicit. The Vandermonde determinant can be expressed as

$$\det(\boldsymbol{T}) = \prod_{1\leq i<j\leq N} (\boldsymbol{b}\boldsymbol{A}^{j-1} - \boldsymbol{b}\boldsymbol{A}^{i-1}). \tag{A.9}$$

It is immediate to see that $\boldsymbol{T}$ is non-singular if and only if $\det(\boldsymbol{T}) \neq 0$, thus the N rows $\boldsymbol{b}, \boldsymbol{bA}, \cdots, \boldsymbol{bA}^{N-2}, \boldsymbol{bA}^{N-1}$ are distinct. The rows of the Vandermonde matrix are generated by the different powers of $\boldsymbol{A}$ multiplied by the same vector $\boldsymbol{b}$. Therefore, asking for $\boldsymbol{T}$ to be non-singular is equivalent to ask that the characteristic polynomial of $\boldsymbol{A}$ has N distinct roots, which requires $\boldsymbol{A}$ to be diagonalizable. Thus, we can write $\boldsymbol{A} = \boldsymbol{PDP}^{-1}$, where $\boldsymbol{D}$ is a diagonal matrix whose entries are the eigenvalues of $\boldsymbol{A}$, and $\boldsymbol{P}$ is a non-singular matrix whose columns are the eigenvectors of $\boldsymbol{A}$. Now, if $\boldsymbol{A}$ has N distinct roots, the Frobenius companion matrix can be diagonalized by the matrix $\boldsymbol{Q}$ whose columns are made of the set of N eigenvectors of $\boldsymbol{A}_{\text{Frob}}$ [53]

$$\boldsymbol{q}_i = (1, \lambda_i, \lambda_i^2, \cdots, \lambda_i^{N-1})^T \tag{A.10}$$

relative to its eigenvalues λ_i. Note that a consistent order of the eigenvalues must be kept throughout the calculations. We have that

$$\boldsymbol{A}_{\mathrm{Frob}} = \boldsymbol{T}^{-1}\boldsymbol{A}\boldsymbol{T} = \boldsymbol{T}^{-1}\boldsymbol{P}\boldsymbol{D}\boldsymbol{P}^{-1}\boldsymbol{T} = \boldsymbol{Q}\boldsymbol{D}\boldsymbol{Q}^{-1} \tag{A.11}$$

which implies $\boldsymbol{Q} = \boldsymbol{T}^{-1}\boldsymbol{P}$. Since all the matrices in the last expression are invertible, we can derive $\boldsymbol{T} = \boldsymbol{P}\boldsymbol{Q}^{-1}$ and consequently find the transformations $\boldsymbol{A}_{\mathrm{Frob}} = \boldsymbol{T}^{-1}\boldsymbol{A}\boldsymbol{T}$.

As an example, consider the 3×3 matrix

$$\boldsymbol{A} = \begin{pmatrix} 2 & 0 & 0 \\ -3 & 5 & -4 \\ -2 & 2 & -1 \end{pmatrix} \tag{A.12}$$

with eigenvalues $\lambda_1 = 3, \lambda_2 = 2, \lambda_3 = 1$. The similarity matrices $\boldsymbol{P}$ and $\boldsymbol{Q}$ are,

$$\boldsymbol{P} = \begin{pmatrix} 0 & 1 & 0 \\ 2 & 1 & 1 \\ 1 & 0 & 1 \end{pmatrix}, \quad \boldsymbol{Q} = \begin{pmatrix} 1 & 1 & 1 \\ 3 & 2 & 1 \\ 9 & 4 & 1 \end{pmatrix}. \tag{A.13}$$

The similarity transformation $\boldsymbol{T}$ between the matrix $\boldsymbol{A}$ and its Frobenius companion matrix $\boldsymbol{A}_{\mathrm{Frob}}$ thus results

$$\boldsymbol{T} = \boldsymbol{P}\boldsymbol{Q}^{-1} = \begin{pmatrix} -3 & 4 & -1 \\ 2 & -3/2 & 1/2 \\ 4 & -4 & 1 \end{pmatrix}. \tag{A.14}$$

We finally perform the transformation,

$$\boldsymbol{A}_{\mathrm{Frob}} = \boldsymbol{T}^{-1}\boldsymbol{A}\boldsymbol{T} = \begin{pmatrix} 0 & 1 & 0 \\ 0 & 0 & 1 \\ 6 & -11 & 6 \end{pmatrix}. \tag{A.15}$$

B Local vs global master equation

B.1 Derivation of the GME

Here, we derive a second-order master equation under the Markov and secular approximations. Essentially, we follow Ref. [139], but simplify the derivation. Let the Hamiltonian of our system be

$$\boldsymbol{H} = \boldsymbol{H}_S + \boldsymbol{H}_B + \lambda \boldsymbol{H}_{SB}, \tag{B.1}$$

where $\boldsymbol{H}_{SB}$ stands for the dissipative interactions between system (S) and bath (B). Note that we are transferring the magnitude of these interactions into λ, which means that the rescaled $\boldsymbol{H}_{SB}$ is now $\mathcal{O}(1)$, unlike in the main text (cf. Eq. (40)).

Our starting point will be the Liouville–von Neumann equation in the interaction picture with respect to $\boldsymbol{H}_0 \coloneqq \boldsymbol{H}_S + \boldsymbol{H}_B$. This is

$$\frac{\mathrm{d}\tilde{\boldsymbol{\rho}}}{\mathrm{d}t} = -i\,\lambda\,[\tilde{\boldsymbol{H}}_{SB}(t), \tilde{\boldsymbol{\rho}}(t)] \coloneqq \lambda\,\tilde{\mathcal{L}}(t)\,\tilde{\boldsymbol{\rho}}(t), \tag{B.2}$$

where $\tilde{\boldsymbol{O}}(t) \coloneqq e^{i\boldsymbol{H}_0 t}\boldsymbol{O}\,e^{-i\boldsymbol{H}_0 t}$. Here, $\tilde{\boldsymbol{\rho}}(t)$ is the full system–environment state. Since we are only interested in the system's marginal $\tilde{\boldsymbol{\varrho}} \coloneqq \mathrm{tr}_B\,\tilde{\boldsymbol{\rho}}(t)$, we trace out the bath, i.e.,

$$\frac{\mathrm{d}\tilde{\boldsymbol{\varrho}}}{\mathrm{d}t} = \lambda\,\mathrm{tr}_B\,\tilde{\mathcal{L}}(t)\,\tilde{\boldsymbol{\rho}}(t) \tag{B.3}$$

and integrate formally. This gives us

$$\tilde{\boldsymbol{\varrho}}(t) = \boldsymbol{\varrho}(0) + \lambda \int_0^t \mathrm{d}s\ \mathrm{tr}_B\,\tilde{\mathcal{L}}(s)\tilde{\boldsymbol{\rho}}(s), \tag{B.4}$$

and iterating,

$$\tilde{\boldsymbol{\varrho}}(t) = \boldsymbol{\varrho}(0) + \lambda \int_0^t \mathrm{d}s\,\mathrm{tr}_B\,\tilde{\mathcal{L}}(s)\boldsymbol{\rho}(0) + \lambda^2 \int_0^t \mathrm{d}s \int_0^s \mathrm{d}s'\,\mathrm{tr}_B\,\tilde{\mathcal{L}}(s)\tilde{\mathcal{L}}(s')\tilde{\boldsymbol{\rho}}(s'). \tag{B.5}$$

Replacing the state $\tilde{\boldsymbol{\rho}}(s')$ in Eq. (B.5) by the expression in (B.4) once again, we see that

$$\tilde{\boldsymbol{\varrho}}(t) = \boldsymbol{\varrho}(0) + \lambda \int_0^t \mathrm{d}s\ \mathrm{tr}_B\,\tilde{\mathcal{L}}(s)\boldsymbol{\rho}(0) + \lambda^2 \int_0^t \mathrm{d}s \int_0^s \mathrm{d}s'\ \mathrm{tr}_B\,\tilde{\mathcal{L}}(s)\tilde{\mathcal{L}}(s')\boldsymbol{\rho}(0) + \mathcal{O}(\lambda^3). \tag{B.6}$$

Assuming that λ is small enough so that all $\mathcal{O}(\lambda^3)$ terms or smaller can be neglected will be our first key approximation. This will lead to a *second-order quantum master equation* after taking the time derivative; namely,

$$\frac{\mathrm{d}\tilde{\boldsymbol{\varrho}}}{\mathrm{d}t} = \lambda \, \mathrm{tr}_B \, \tilde{\mathcal{L}}(t)\boldsymbol{\rho}(0) + \lambda^2 \int_0^t \mathrm{d}s \, \mathrm{tr}_B \, \tilde{\mathcal{L}}(t)\tilde{\mathcal{L}}(s)\boldsymbol{\rho}(0). \tag{B.7}$$

Notice, however, that this master equation time-non-local and, still, of little practical use. To overcome this problem, we make two additional assumptions: First, we require the *initial* state to include no correlations between system's and bath's degrees of freedom. Namely, $\boldsymbol{\rho}(0) = \boldsymbol{\varrho}_S(0) \otimes \boldsymbol{\varrho}_B$. Secondly, we impose

$$\mathrm{tr}_B \, \tilde{\mathcal{L}}(s)\boldsymbol{\varrho}(0) \otimes \boldsymbol{\varrho}_B = 0. \tag{B.8}$$

For instance, if the system–bath interaction is of the simple form $\boldsymbol{H}_{SB} = \boldsymbol{S} \otimes \boldsymbol{B}$ (cf. Eq. (40)), Eq. (B.8) translates into $\langle \boldsymbol{B} \rangle = 0$ when averaged on the initial state of the environment.

Inserting (B.8) into (B.6), we see that $\boldsymbol{\varrho}(0) = \tilde{\boldsymbol{\varrho}}(t) + \mathcal{O}(\lambda^2)$, which allows us to write our equation in the much more convenient time-local form

$$\frac{\mathrm{d}\tilde{\boldsymbol{\varrho}}}{\mathrm{d}t} = \lambda^2 \int_0^t \mathrm{d}s \, \mathrm{tr}_B \, \tilde{\mathcal{L}}(t)\tilde{\mathcal{L}}(s)\tilde{\boldsymbol{\varrho}}(t) \otimes \boldsymbol{\varrho}_B \tag{B.9}$$

while still remaining accurate within $\mathcal{O}(\lambda^3)$. It is customary to perform a change of variables in the integral, re-expressing it as

$$\frac{\mathrm{d}\tilde{\boldsymbol{\varrho}}}{\mathrm{d}t} = \lambda^2 \int_0^t \mathrm{d}s \, \mathrm{tr}_B \, \tilde{\mathcal{L}}(t)\tilde{\mathcal{L}}(t-s)\tilde{\boldsymbol{\varrho}}(t) \otimes \boldsymbol{\varrho}_B. \tag{B.10}$$

We note that objects like

$$\mathrm{tr}_B \, \tilde{\mathcal{L}}(t)\tilde{\mathcal{L}}(t-s)\tilde{\boldsymbol{\varrho}}(t) \otimes \boldsymbol{\varrho}_B \tag{B.11}$$

enclose two-time correlation functions of bath operators, i.e., $\mathrm{tr}_B \, \tilde{\boldsymbol{B}}(t)\tilde{\boldsymbol{B}}(t-s)\boldsymbol{\varrho}_B$. In many situations of practical interest, these decay extremely fast—much faster than any relevant timescale in the problem. Hence, we may replace the upper

integration limit in (B.10) by infinity without substantial error

$$\frac{\mathrm{d}\tilde{\boldsymbol{\varrho}}}{\mathrm{d}t} = \lambda^2 \int_0^\infty \mathrm{d}s \ \mathrm{tr}_B \, \tilde{\mathcal{L}}(t)\tilde{\mathcal{L}}(t-s)\tilde{\boldsymbol{\varrho}}(t) \otimes \boldsymbol{\varrho}_B. \tag{B.12}$$

This is often referred-to as the *Markov approximation* and the resulting equation, as (Markovian) *Redfield master equation*. However, the use of the term 'Markovian' can be problematic since the dynamics generated by this equation is, in general, not even *positive* [139]. This means that the corresponding dynamical map might not be *divisible*, and lack of divisibility is often associated with '*non*-Markovianity' [234].

Before the final step in our derivation, we must transcribe the shorthand $\mathrm{tr}_B \, \tilde{\mathcal{L}}(t)\tilde{\mathcal{L}}(t-s)\tilde{\boldsymbol{\varrho}}(t) \otimes \boldsymbol{\varrho}_B$, which gives

$$\tilde{\mathcal{L}}(t)\tilde{\mathcal{L}}(t-s)\tilde{\boldsymbol{\varrho}}(t)\otimes\boldsymbol{\varrho}_B = -\tilde{\boldsymbol{H}}_{SB}(t)\tilde{\boldsymbol{H}}_{SB}(t-s)\tilde{\boldsymbol{\varrho}}(t)\otimes\boldsymbol{\varrho}_B + \tilde{\boldsymbol{H}}_{SB}(t-s)\tilde{\boldsymbol{\varrho}}(t)\otimes\boldsymbol{\varrho}_B\tilde{\boldsymbol{H}}_{SB}(t) + \text{h.c.}$$

We may always write the system–bath interaction term as $\boldsymbol{H}_{SB} = \sum_\alpha \boldsymbol{S}_\alpha \otimes \boldsymbol{B}_\alpha$. Here, we take $\boldsymbol{H}_{SB} = \boldsymbol{S} \otimes \boldsymbol{B}$ for simplicity, and hence,

$$\begin{aligned}\tilde{\mathcal{L}}(t)\tilde{\mathcal{L}}(t-s)\tilde{\boldsymbol{\varrho}}(t) \otimes \boldsymbol{\varrho}_B = &- \tilde{\boldsymbol{S}}(t)\tilde{\boldsymbol{S}}(t-s)\tilde{\boldsymbol{\varrho}}(t) \ \mathrm{tr}_B \, \tilde{\boldsymbol{B}}(t)\tilde{\boldsymbol{B}}(t-s)\boldsymbol{\varrho}_B \\ &+ \tilde{\boldsymbol{S}}(t-s)\tilde{\boldsymbol{\varrho}}(t)\tilde{\boldsymbol{S}}(t) \ \mathrm{tr}_B \, \tilde{\boldsymbol{B}}(t-s)\boldsymbol{\varrho}_B\tilde{\boldsymbol{B}}(t) + \text{h.c.}\end{aligned}$$

The explicit form of the interaction-picture system operator $\tilde{\boldsymbol{S}}(t)$ can be found easily by exploiting the decomposition from Eqs. (31) in the main text. Namely, given the properties of the jump operators $\boldsymbol{A}_\omega$ it is easy to see that $\tilde{\boldsymbol{S}}(t) = \sum_\omega \boldsymbol{A}_\omega \, e^{-i\omega t}$. Putting together all the pieces

$$\begin{aligned}\frac{\mathrm{d}\tilde{\boldsymbol{\varrho}}}{\mathrm{d}t} &= \sum\nolimits_{\omega,\omega'} \left(-\Gamma(\omega) \, \boldsymbol{A}_{\omega'}\boldsymbol{A}_\omega e^{-i(\omega+\omega')t}\tilde{\boldsymbol{\varrho}}(t) \ + \Gamma(\omega) \, \boldsymbol{A}_\omega\tilde{\boldsymbol{\varrho}}(t)\boldsymbol{A}_{\omega'} e^{-i(\omega+\omega')t} + \text{h.c.}\right) \\ &= \sum\nolimits_{\omega,\omega'} \left(-\Gamma(\omega) \, \boldsymbol{A}^\dagger_{\omega'}\boldsymbol{A}_\omega e^{i(\omega'-\omega)t}\tilde{\boldsymbol{\varrho}}(t) \ + \Gamma(\omega) \, \boldsymbol{A}_\omega\tilde{\boldsymbol{\varrho}}(t)\boldsymbol{A}^\dagger_{\omega'} e^{i(\omega'-\omega')t} + \text{h.c.}\right), \end{aligned} \tag{B.13}$$

where

$$\Gamma(\omega) \coloneqq \lambda^2 \int_0^\infty \mathrm{d}s \, e^{i\omega s} \, \mathrm{tr}_B \, \tilde{\boldsymbol{B}}(t)\tilde{\boldsymbol{B}}(t-s), \tag{B.14}$$

and the corresponding real and imaginary parts are $\Gamma(\omega) = \frac{1}{2}\gamma(\omega) + iS(\omega)$. The imaginary part $S(\omega)$ is typically ignored. It introduces two effects—a displacement of the energy levels of $\boldsymbol{H}_S$ through a *Lamb shift* term $\boldsymbol{H}_L = \sum_\omega S(\omega)\boldsymbol{A}^\dagger_\omega\boldsymbol{A}_\omega$

($[\boldsymbol{H}_S, \boldsymbol{H}_L] = 0$); but also, non-trivial dissipative terms. These are, however, typically very small.

Many terms in Eq. (B.13) can be dropped, since they are fast-oscillating and average out to zero over the time-scale defined by the dynamics of $\boldsymbol{\varrho}(t)$ [87]. Namely, we can drop all terms for which ω and ω' have the same sign ($\omega \times \omega' > 0$), since these oscillate as $e^{\pm|\omega+\omega'|t}$. Eq. (B.13) is often called 'partial Redfield equation' [88, 100, 105]

It is now time to abandon the interaction picture undoing the corresponding unitary transformation. This gives us

$$\frac{\mathrm{d}\boldsymbol{\varrho}}{\mathrm{d}t} = -i[\boldsymbol{H}_S, \boldsymbol{\varrho}] + \frac{1}{2}\sum_{\omega\times\omega'<0} \gamma(\omega)\left(\boldsymbol{A}_\omega \boldsymbol{\varrho}(t)\boldsymbol{A}_{\omega'}^\dagger - \boldsymbol{A}_{\omega'}^\dagger \boldsymbol{A}_\omega \boldsymbol{\varrho}(t)\right) + \text{h.c.} \tag{B.15}$$

One final step is necessary to bring Eq. (B.15) into GKSL form—the *secular approximation*. This consists in removing all terms in which $\omega \neq \omega'$ from the double sum in (B.15). The rationale for this—seemingly arbitrary—simplification often involves again a time averaging which now 'kills' *all* the remaining oscillating terms in Eq. (B.13) [87]. From all approximations involved in the process, this is certainly the most problematic and difficult to justify. Nonetheless, it does hold in many situations of practical interest [87]. This way, we finally arrive at the celebrated global GKSL master equation

$$\frac{\mathrm{d}\boldsymbol{\varrho}}{\mathrm{d}t} = -i[\boldsymbol{H}_S, \boldsymbol{\varrho}] + \sum_{\omega} \gamma(\omega)\left(\boldsymbol{A}_\omega \boldsymbol{\varrho}(t)\boldsymbol{A}_\omega^\dagger - \frac{1}{2}\{\boldsymbol{A}_\omega^\dagger \boldsymbol{A}_\omega \boldsymbol{\varrho}(t)\}_+\right). \tag{B.16}$$

B.2 Dynamics of second-order moments

We now study the dynamics of the second-order moments showing the matrices of the dynamics generated by LME (Eq. (B.21)), GME (Eq. (B.25)) and Redfield equation (Eq. (B.28)).

We first consider the local approach. Using Eq. (35), we obtain a set of 10 coupled first-order differential equations defining the dynamics of the covariances C_{ij} of the system, as defined in Sec. 3.6.2. These equations can be expressed as

$$\frac{\mathrm{d}\langle\tilde{\mathbf{q}}\rangle}{\mathrm{d}t} = \mathsf{M}_{\mathscr{L},2}\langle\tilde{\mathbf{q}}\rangle + \mathsf{c}_{\mathscr{L},2}, \tag{B.17}$$

where the ordered vector of the covariances is

$$\tilde{\mathbf{q}} \coloneqq \left(\boldsymbol{x}_h^2, \boldsymbol{p}_h^2, \frac{1}{2}\{\boldsymbol{x}_h, \boldsymbol{p}_h\}_+, \boldsymbol{x}_c^2, \boldsymbol{p}_c^2, \frac{1}{2}\{\boldsymbol{x}_c, \boldsymbol{p}_c\}_+, \boldsymbol{x}_h\boldsymbol{p}_c, \boldsymbol{x}_c\boldsymbol{p}_h, \boldsymbol{x}_h\boldsymbol{x}_c, \boldsymbol{p}_h\boldsymbol{p}_c\right)^{\mathsf{T}}, \tag{B.18}$$

and the constant vector $\mathsf{c}_{\mathscr{L},2}$ is

$$\mathsf{c}_{\mathscr{L},2} = \left(\frac{\Sigma_\omega^{(h)}}{2\omega}, \frac{\omega\Sigma_\omega^{(h)}}{2}, 0, \frac{\Sigma_\omega^{(c)}}{2\omega}, \frac{\omega\Sigma_\omega^{(c)}}{2}, 0, 0, 0, 0, 0\right)^{\mathsf{T}}. \tag{B.19}$$

The coefficients $\Sigma_\omega^{(\alpha)}$s are defined as

$$\Sigma_\omega^{(\alpha)} \coloneqq \frac{\gamma_{-\omega}^{(\alpha)} + \gamma_\omega^{(\alpha)}}{2\omega}. \tag{B.20}$$

Therefore, in the local approach, the matrix of the dynamics takes the form

$$\mathsf{M}_{\mathscr{L},2} = \begin{pmatrix}
\Delta_\omega^{(h)} & 0 & 2 & 0 & 0 & 0 & 0 & 0 & 0 & 0 \\
0 & \Delta_\omega^{(h)} & -2\omega^2 & 0 & 0 & 0 & 0 & k & 0 & 0 \\
-\omega^2 & 1 & \Delta_\omega^{(h)} & 0 & 0 & 0 & 0 & 0 & k/2 & 0 \\
0 & 0 & 0 & \Delta_\omega^{(c)} & 0 & 2 & 0 & 0 & 0 & 0 \\
0 & 0 & 0 & 0 & \Delta_\omega^{(c)} & -2\omega^2 & k & 0 & 0 & 0 \\
0 & 0 & 0 & -\omega^2 & 1 & \Delta_\omega^{(c)} & 0 & 0 & k/2 & 0 \\
k/2 & 0 & 0 & 0 & 0 & 0 & \frac{\Delta_\omega^{(h)}+\Delta_\omega^{(c)}}{2} & 0 & -\omega^2 & 1 \\
0 & 0 & 0 & k/2 & 0 & 0 & 0 & \frac{\Delta_\omega^{(h)}+\Delta_\omega^{(c)}}{2} & -\omega^2 & 1 \\
0 & 0 & 0 & 0 & 0 & 0 & 1 & 1 & \frac{\Delta_\omega^{(h)}+\Delta_\omega^{(c)}}{2} & 0 \\
0 & 0 & k/2 & 0 & 0 & k/2 & -\omega^2 & -\omega^2 & 0 & \frac{\Delta_\omega^{(h)}+\Delta_\omega^{(c)}}{2}
\end{pmatrix}, \tag{B.21}$$

where the coefficients $\Delta_\omega^{(\alpha)}$ were already introduced in Eq. (59). Studying (numerically) the condition number of the eigenvectors matrix of $\mathsf{M}_{\mathscr{L},2}$, we obtain the exact same line of singularities emerging from the condition in Eq. (61).

Let us consider next the case of the global master equation. Since the condition number is independent of the basis, in the following we report the dynamics expressed in terms of the normal-mode quadratures of the system. In the case of the global master equation, we obtain

$$\frac{\mathrm{d}\langle\tilde{\mathbf{Q}}\rangle}{\mathrm{d}t} = \mathsf{M}'_{\mathscr{G},2}\langle\tilde{\mathbf{Q}}\rangle + \mathsf{c}'_{\mathscr{G},2}. \tag{B.22}$$

In this case, the ordered vector of the covariances is

$$\tilde{\mathbf{Q}} := \left(\boldsymbol{\eta}_1^2, \boldsymbol{\Pi}_1^2, \frac{1}{2}\{\boldsymbol{\eta}_1, \boldsymbol{\Pi}_1\}_+, \boldsymbol{\eta}_2^2, \boldsymbol{\Pi}_2^2, \frac{1}{2}\{\boldsymbol{\eta}_2, \boldsymbol{\Pi}_2\}_+, \boldsymbol{\eta}_1\boldsymbol{\Pi}_2, \boldsymbol{\eta}_2\boldsymbol{\Pi}_1, \boldsymbol{\eta}_1\boldsymbol{\eta}_2, \boldsymbol{\Pi}_1\boldsymbol{\Pi}_2\right)^{\mathsf{T}}, \tag{B.23}$$

and the constant vector is given by

$$\mathsf{c}'_{\mathscr{G},2} = \left(\frac{\tilde{\Sigma}_1}{2\Omega_1}, \frac{\Omega_1\tilde{\Sigma}_1}{2}, 0, \frac{\tilde{\Sigma}_2}{2\Omega_2}, \frac{\Omega_2\tilde{\Sigma}_2}{2}, 0, 0, 0, 0, 0\right)^{\mathsf{T}}, \tag{B.24}$$

while the matrix of the dynamics is

$$\mathsf{M}'_{\mathscr{G},2} = \begin{pmatrix}
\tilde{\Delta}_1 & 0 & 2 & 0 & 0 & 0 & 0 & 0 & 0 & 0 \\
0 & \tilde{\Delta}_1 & -2\Omega_1^2 & 0 & 0 & 0 & 0 & 0 & 0 & 0 \\
-2\Omega_1^2 & 1 & \tilde{\Delta}_1 & 0 & 0 & 0 & 0 & 0 & 0 & 0 \\
0 & 0 & 0 & \tilde{\Delta}_2 & 0 & 2 & 0 & 0 & 0 & 0 \\
0 & 0 & 0 & 0 & \tilde{\Delta}_2 & -2\Omega_2^2 & 0 & 0 & 0 & 0 \\
0 & 0 & 0 & -\Omega_2^2 & 1 & \tilde{\Delta}_2 & 0 & 0 & 0 & 0 \\
0 & 0 & 0 & 0 & 0 & 0 & \frac{\tilde{\Delta}_1+\tilde{\Delta}_2}{2} & 0 & -\Omega_2^2 & 1 \\
0 & 0 & 0 & 0 & 0 & 0 & 0 & \frac{\tilde{\Delta}_1+\tilde{\Delta}_2}{2} & -\Omega_1^2 & 1 \\
0 & 0 & 0 & 0 & 0 & 0 & 1 & 1 & \frac{\tilde{\Delta}_1+\tilde{\Delta}_2}{2} & 0 \\
0 & 0 & 0 & 0 & 0 & 0 & -\Omega_1^2 & -\Omega_2^2 & 0 & \frac{\tilde{\Delta}_1+\tilde{\Delta}_2}{2}
\end{pmatrix}. \tag{B.25}$$

The $\tilde{\Delta}_j$ have been introduced in Eq. (69) and, analogously, we define here the coefficients

$$\tilde{\Sigma}_j := \frac{1}{2}\sum\nolimits_{\alpha} \Sigma_{\Omega_j}^{(\alpha)}. \tag{B.26}$$

In this case, the evaluation of the condition number reveals no exceptional points, just as in the case of the first-order moments. Hence, the discrepancy between the local and global master equation persists at the level of the second-order moments.

Now, we present the evolution of the covariances in the case of the Redfield equation. Again, in normal-mode variables, the dynamics is expressed as

$$\frac{\mathrm{d}\langle\tilde{\mathbf{Q}}\rangle}{\mathrm{d}t} = \mathsf{M}'_{\mathscr{R},2}\langle\tilde{\mathbf{Q}}\rangle + \mathsf{c}'_{\mathscr{R},2}. \tag{B.27}$$

The matrix of the dynamics takes the form

$$\mathsf{M}'_{\mathscr{R},2} = \begin{pmatrix} \tilde{\Delta}_1 & 0 & 2 & 0 & 0 & 0 & 0 & 0 & \frac{\Omega_2}{\Omega 1}\tilde{\Delta}'_2 & 0 \\ 0 & \tilde{\Delta}_1 & -2\Omega_1^2 & 0 & 0 & 0 & 0 & 0 & 0 & \tilde{\Delta}'_2 \\ -2\Omega_1^2 & 1 & \tilde{\Delta}_1 & 0 & 0 & 0 & \frac{\tilde{\Delta}'_2}{2} & \frac{\Omega_2}{2\Omega_1}\tilde{\Delta}'_2 & 0 & 0 \\ 0 & 0 & 0 & \tilde{\Delta}_2 & 0 & 2 & 0 & 0 & \frac{\Omega_1}{\Omega_2}\tilde{\Delta}'_1 & 0 \\ 0 & 0 & 0 & 0 & \tilde{\Delta}_2 & -2\Omega_2^2 & 0 & 0 & 0 & \tilde{\Delta}'_1 \\ 0 & 0 & 0 & -\Omega_2^2 & 1 & \tilde{\Delta}_2 & \frac{\tilde{\Delta}'_1}{2} & 0 & 0 & 0 \\ 0 & 0 & \frac{\tilde{\Delta}'_1}{2} & 0 & 0 & \frac{\Omega_2}{2\Omega_1}\tilde{\Delta}'_2 & \frac{\tilde{\Delta}_1+\tilde{\Delta}_2}{2} & 0 & -\Omega_2^2 & 1 \\ 0 & 0 & \frac{\Omega_1}{2\Omega_2}\tilde{\Delta}'_1 & 0 & 0 & \frac{\tilde{\Delta}'_2}{2} & 0 & \frac{\tilde{\Delta}_1+\tilde{\Delta}_2}{2} & -\Omega_1^2 & 1 \\ \frac{\Omega_1}{2\Omega_2}\tilde{\Delta}'_1 & 0 & 0 & \frac{\Omega_2}{2\Omega_1}\tilde{\Delta}'_2 & 0 & 0 & 1 & 1 & \frac{\tilde{\Delta}_1+\tilde{\Delta}_2}{2} & 0 \\ 0 & \frac{\tilde{\Delta}'_1}{2} & 0 & 0 & \frac{\tilde{\Delta}'_2}{2} & 0 & -\Omega_1^2 & -\Omega_2^2 & 0 & \frac{\tilde{\Delta}_1+\tilde{\Delta}_2}{2} \end{pmatrix}, \tag{B.28}$$

while the constant vector is

$$\mathsf{c}'_{\mathscr{R},2} = \left(\frac{\tilde{\Sigma}_1}{2\Omega_1}, \frac{\Omega_1\tilde{\Sigma}_1}{2}, 0, \frac{\tilde{\Sigma}_2}{2\Omega_2}, \frac{\Omega_2\tilde{\Sigma}_2}{2}, 0, 0, 0, \frac{\tilde{\Sigma}'_1}{4\Omega_2} + \frac{\tilde{\Sigma}'_2}{4\Omega_1}, \frac{\Omega_1\tilde{\Sigma}'_1}{4} + \frac{\Omega_2\tilde{\Sigma}'_2}{4} \right)^{\mathsf{T}}. \tag{B.29}$$

In these expressions, we have defined the new coefficients

$$\tilde{\Delta}'_j \coloneqq \frac{1}{2}\left(\Delta^{(h)}_{\Omega_j} - \Delta^{(c)}_{\Omega_j}\right) \tag{B.30a}$$

$$\tilde{\Sigma}'_j \coloneqq \frac{1}{2}\left(\Sigma^{(h)}_{\Omega_j} - \Sigma^{(c)}_{\Omega_j}\right). \tag{B.30b}$$

Calculating the condition number of the corresponding matrix of eigenvectors, one can readily confirm, once again, the presence of the exceptional points along the exact same 'exceptional lines' (61).

It is worth noting that, since the system considered is Gaussian, these singularities will be present, according to the LME and the Redfield equation, in any n^{th}-order moment. This is so, because any higher-order correlation functions of a Gaussian system can be cast as a combination of first- and second-order moments, and these simultaneously display exceptional points. Conversely, no moments of any order will ever pick up exceptional points according to the global description.

B.3 Conditions for the appearance of exceptional points

As mentioned in the main text, for the exceptional points to appear, dissipation must be asymmetric and the oscillators must be resonant. Here, we show the validity of this statement.

Consider the non-resonant case, where the resonators have bare frequencies ω_h and ω_c. The matrix of the dynamics of the first order moments is

$$\tilde{\mathsf{M}}_{\mathscr{L},1} = \frac{1}{2}\begin{pmatrix} \Delta^{(h)}_{\omega_h} & 2 & 0 & 0 \\ -2\omega_h^2 & \Delta^{(h)}_{\omega_h} & -2k & 0 \\ 0 & 0 & \Delta^{(c)}_{\omega_c} & 2 \\ -2k & 0 & -2\omega_c^2 & \Delta^{(c)}_{\omega_c} \end{pmatrix}, \tag{B.31}$$

where

$$\Delta^{(\alpha)}_{\omega_i} := \frac{\gamma^{(\alpha)}_{-\omega_i} - \gamma^{(\alpha)}_{\omega_i}}{2\omega_i}. \tag{B.32}$$

To identify the exceptional points we look for square root singularities in the expressions of the eigenvalues. Two of the eigenvalues of the latter matrix are

$$\lambda_{1,2} = \frac{1}{4}\Big[\Delta^{(h)}_{\omega_h} + \Delta^{(c)}_{\omega_c} + 2\sqrt{-(\omega_h+\omega_c)^2} + \tag{B.33}$$
$$\pm \sqrt{(\Delta^{(h)}_{\omega_h} - \Delta^{(c)}_{\omega_c})^2 - 4(\omega_h-\omega_c)^2 - \frac{4k^2}{\omega_h\omega_c} - 4(\Delta^{(h)}_{\omega_h} - \Delta^{(c)}_{\omega_c})\frac{\omega_h^2-\omega_c^2}{\sqrt{-(\omega_h+\omega_c)^2}}}\Big]$$

which coalesce when the latter square root vanishes. Therefore, we find the condition of exceptional points for the inter-resonators coupling k,

$$k = \pm\frac{1}{2}\sqrt{\omega_h\omega_c}\sqrt{(\Delta^{(h)}_{\omega_h} - \Delta^{(c)}_{\omega_c})^2 - 4(\omega_h-\omega_c)\left[(\omega_h-\omega_c) - i(\Delta^{(h)}_{\omega_h} - \Delta^{(c)}_{\omega_c})\right]}. \tag{B.34}$$

Since the inter-resonators coupling k is assumed to be real, we have the only acceptable solution when the system is resonant, $\omega_h = \omega_c = \omega$ and dissipation asymmetric, $\Delta_h \neq \Delta_c$. In this way, we recover the expression in Eq. (60).

B.4 Local, global, and Redfield dissipators out of resonance

We now show that the relationship between the Redfield and the local approach pertains even in the non-resonant case. First of all, note that, out of resonance, the transformation matrix P that defines the rotation into normal modes gener-

alises to [88]

$$\mathsf{P} = \begin{pmatrix} \sin\zeta & \cos\zeta \\ \cos\zeta & -\sin\zeta \end{pmatrix}, \tag{B.35}$$

where $\zeta = \arccos\sqrt{\dfrac{\delta+\sqrt{4k^2+\delta^2}}{2\sqrt{4k^2+\delta^2}}}$ and $\delta = \omega_h^2 - \omega_c^2$. The eigenfrequencies are

$$\Omega_{1,2}^2 = \frac{1}{2}\left(\omega_h^2 + \omega_c^2 \pm \sqrt{4k^2+\delta^2}\right). \tag{B.36}$$

Namely, in the non-resonant case *both* the eigenvectors and the Bohr frequencies of $\boldsymbol{H}_S$ depend explicitly on the internal coupling strength k.

Moving now to the Redfield dissipators (B.15) we can write it out in adjoint form as

$$\begin{aligned}
\mathscr{R}_h^\dagger(\boldsymbol{O}) + \mathscr{R}_c^\dagger(\boldsymbol{O}) = \sum_{i,j=1}^{2} \Big[& \frac{\gamma_{\Omega_i}^{(h)}}{2}\left(\boldsymbol{A}_{-\Omega_j}^{(h)}\boldsymbol{O}\boldsymbol{A}_{\Omega_i}^{(h)} + \boldsymbol{A}_{-\Omega_i}^{(h)}\boldsymbol{O}\boldsymbol{A}_{\Omega_j}^{(h)} - \boldsymbol{O}\boldsymbol{A}_{-\Omega_j}^{(h)}\boldsymbol{A}_{\Omega_i}^{(h)} - \boldsymbol{A}_{-\Omega_i}^{(h)}\boldsymbol{A}_{\Omega_j}^{(h)}\boldsymbol{O}\right) \\
& + \frac{\gamma_{-\Omega_i}^{(h)}}{2}\left(\boldsymbol{A}_{\Omega_j}^{(h)}\boldsymbol{O}\boldsymbol{A}_{-\Omega_i}^{(h)} + \boldsymbol{A}_{\Omega_i}^{(h)}\boldsymbol{O}\boldsymbol{A}_{-\Omega_j}^{(h)} - \boldsymbol{O}\boldsymbol{A}_{\Omega_j}^{(h)}\boldsymbol{A}_{-\Omega_i}^{(h)} - \boldsymbol{A}_{\Omega_i}^{(h)}\boldsymbol{A}_{-\Omega_j}^{(h)}\boldsymbol{O}\right) \\
& + \frac{\gamma_{\Omega_i}^{(c)}}{2}\left(\boldsymbol{A}_{-\Omega_j}^{(c)}\boldsymbol{O}\boldsymbol{A}_{\Omega_i}^{(c)} + \boldsymbol{A}_{-\Omega_i}^{(c)}\boldsymbol{O}\boldsymbol{A}_{\Omega_j}^{(c)} - \boldsymbol{O}\boldsymbol{A}_{-\Omega_j}^{(c)}\boldsymbol{A}_{\Omega_i}^{(c)} - \boldsymbol{A}_{-\Omega_i}^{(c)}\boldsymbol{A}_{\Omega_j}^{(c)}\boldsymbol{O}\right) \\
& + \frac{\gamma_{-\Omega_i}^{(c)}}{2}\left(\boldsymbol{A}_{\Omega_j}^{(c)}\boldsymbol{O}\boldsymbol{A}_{-\Omega_i}^{(c)} + \boldsymbol{A}_{\Omega_i}^{(c)}\boldsymbol{O}\boldsymbol{A}_{-\Omega_j}^{(c)} - \boldsymbol{O}\boldsymbol{A}_{\Omega_j}^{(c)}\boldsymbol{A}_{-\Omega_i}^{(c)} - \boldsymbol{A}_{\Omega_i}^{(c)}\boldsymbol{A}_{-\Omega_j}^{(c)}\boldsymbol{O}\right)\Big]
\end{aligned} \tag{B.37}$$

To find the zeroth order term $\mathscr{R}^{\dagger\,(0)}$, we must simply set $k=0$ in P and the normal-mode frequencies. We thus find that the normal modes rotate back to the local coordinates $\boldsymbol{x}_\alpha$ and Ω_α collapse into the bare frequencies ω_α. Importantly, as a result, frequency $\Omega_1^{(0)} = \omega_h$ will only appear in the hot dissipator $\mathscr{R}_h^\dagger$ and $\Omega_2^{(0)} = \omega_c$ will be only linked to $\mathscr{R}_c^\dagger$. Therefore, the double sums in Eq. (B.37) directly transform into the local expression (36) which in the specific case of the system

studied is

$$\begin{aligned}\mathscr{L}_h^\dagger(\boldsymbol{O})+\mathscr{L}_c^\dagger(\boldsymbol{O}) = \gamma_{\omega_h}^{(h)}&\left(\boldsymbol{L}_{-\omega_h}^{(h)}\boldsymbol{O}\boldsymbol{L}_{\omega_h}^{(h)}-\frac{1}{2}\{\boldsymbol{L}_{-\omega_h}^{(h)}\boldsymbol{L}_{\omega_h}^{(h)},\boldsymbol{O}\}_+\right)\\ +\gamma_{-\omega_h}^{(h)}&\left(\boldsymbol{L}_{\omega_h}^{(h)}\boldsymbol{O}\boldsymbol{L}_{-\omega_h}^{(h)}-\frac{1}{2}\{\boldsymbol{L}_{\omega_h}^{(h)}\boldsymbol{L}_{-\omega_h}^{(h)},\boldsymbol{O}\}_+\right)\\ +\gamma_{\omega_c}^{(c)}&\left(\boldsymbol{L}_{-\omega_c}^{(c)}\boldsymbol{O}\boldsymbol{L}_{\omega_c}^{(c)}-\frac{1}{2}\{\boldsymbol{L}_{-\omega_c}^{(c)}\boldsymbol{L}_{\omega_c}^{(c)},\boldsymbol{O}\}_+\right)\\ +\gamma_{-\omega_c}^{(c)}&\left(\boldsymbol{L}_{\omega_c}^{(c)}\boldsymbol{O}\boldsymbol{L}_{-\omega_c}^{(c)}-\frac{1}{2}\{\boldsymbol{L}_{\omega_c}^{(c)}\boldsymbol{L}_{-\omega_c}^{(c)},\boldsymbol{O}\}_+\right).\end{aligned} \tag{B.38}$$

In the low-k limit, this will always be true—regardless of $\boldsymbol{H}_S$—provided that the system couples to each bath by a single transition at some specific frequency.

In the same way, it is easy to show that the relationship between the global and the local dissipators, proposed in [113], remains valid in the out-of-resonance case. The adjoint global dissipator takes the form

$$\begin{aligned}\mathscr{G}_h^\dagger(\boldsymbol{O})+\mathscr{G}_c^\dagger(\boldsymbol{O}) = \sum_{i=1}^{2}\Big[&\gamma_{\Omega_i}^{(h)}\left(\boldsymbol{A}_{-\Omega_i}^{(h)}\boldsymbol{O}\boldsymbol{A}_{\Omega_i}^{(h)}-\frac{1}{2}\{\boldsymbol{A}_{-\Omega_i}^{(h)}\boldsymbol{A}_{\Omega_i}^{(h)},\boldsymbol{O}\}_+\right)\\ &+\gamma_{-\Omega_i}^{(h)}\left(\boldsymbol{A}_{\Omega_i}^{(h)}\boldsymbol{O}\boldsymbol{A}_{-\Omega_i}^{(h)}-\frac{1}{2}\{\boldsymbol{A}_{\Omega_i}^{(h)}\boldsymbol{A}_{-\Omega_i}^{(h)},\boldsymbol{O}\}_+\right)\\ &+\gamma_{\Omega_i}^{(c)}\left(\boldsymbol{A}_{-\Omega_i}^{(c)}\boldsymbol{O}\boldsymbol{A}_{\Omega_i}^{(c)}-\frac{1}{2}\{\boldsymbol{A}_{-\Omega_i}^{(c)}\boldsymbol{A}_{\Omega_i}^{(c)},\boldsymbol{O}\}_+\right)\\ &+\gamma_{-\Omega_i}^{(c)}\left(\boldsymbol{A}_{\Omega_i}^{(c)}\boldsymbol{O}\boldsymbol{A}_{-\Omega_i}^{(c)}-\frac{1}{2}\{\boldsymbol{A}_{\Omega_i}^{(c)}\boldsymbol{A}_{-\Omega_i}^{(c)},\boldsymbol{O}\}_+\right)\Big].\end{aligned} \tag{B.39}$$

Again, to find the zeroth order term of the k-expansion of the dissipator, we set $k=0$ in the matrix P. Therefore, the global jump operators in Eq. (66) are cast to $\boldsymbol{A}_{\Omega_1}^{(h)}=\boldsymbol{L}_{\omega_h}^{(h)}, \boldsymbol{A}_{\Omega_2}^{(h)}=0, \boldsymbol{A}_{\Omega_1}^{(c)}=0, \boldsymbol{A}_{\Omega_2}^{(c)}=\boldsymbol{L}_{\omega_c}^{(c)}$ which makes the global dissipator converge to the local expression.

C Spin-boson model

C.1 Tracing for spin and reservoir, in classical and quantum setting

C.1.1 Spin tracing in the classical setting

For a classical spin of length S_0, with components S_x, S_y, S_z, one can change into spherical coordinates, i.e.

$$S_x = S_0 \sin\vartheta\cos\varphi, \quad S_y = S_0 \sin\vartheta \sin\varphi, \tag{C.1}$$
$$S_z = S_0\cos\vartheta, \qquad \vartheta \in [0,\pi], \varphi \in [0, 2\pi].$$

Then, traces of functions $A(S_x, S_z)$ are evaluated as

$$\mathrm{tr}_{\mathrm{S}}^{\mathrm{cl}}[A(S_x,S_z)] = \tag{C.2}$$
$$\frac{1}{4\pi}\int_0^{2\pi}\mathrm{d}\varphi \int_0^{\pi}\mathrm{d}\vartheta\ \sin\vartheta A(S_0\sin\vartheta\cos\varphi, S_0\cos\vartheta).$$

C.1.2 Spin tracing in the quantum setting

For a quantum spin S_0, given any orthogonal basis $|m\rangle$, then the trace of functions of the spin operators $A(S_x, S_z)$ are evaluated as

$$\mathrm{tr}_{\mathrm{S}}^{\mathrm{qu}}[A(S_x,S_z)] = \sum_m \langle m|\, A(S_x,S_z)\,|m\rangle\,. \tag{C.3}$$

C.1.3 Reservoir traces

When taking traces over the environmental degrees of freedom (in either the classical or quantum case), we ought to first discretise the energy spectrum of H_{R}. This is because, strictly speaking, the partition function for the reservoir, $Z_{\mathrm{R}} = \mathrm{tr}\big[\exp(-\beta H_{\mathrm{R}})\big]$, is not well defined in the continuum limit. Thus, we write

$$H_{\mathrm{R}} = \sum_{n=0}^{\infty}\frac{1}{2}\left(P_{\omega_n}^2 + \omega_n^2 X_{\omega_n}^2\right). \tag{C.4}$$

Then, for example, the classical partition function of the environment is

$$Z_{\mathrm{R}}^{\mathrm{cl}} = \prod_{n=0}^{\infty} \left[\int_{-\infty}^{+\infty} \mathrm{d}X_{\omega_n} \int_{-\infty}^{\infty} \mathrm{d}P_{\omega_n} e^{-\frac{\beta}{2}\left(P_{\omega_n}^2 + \omega_n^2 X_{\omega_n}^2\right)} \right], \tag{C.5}$$

and similarly for the quantum case.

C.2 Expectation values from the partition function

With the partition function of the MF we can proceed to calculate the S_z and S_x expectation values as follows.

C.2.1 Classical case

For the classical spin, from (82) we have the partition function

$$\tilde{Z}_{\mathrm{S}}^{\mathrm{cl}} = \frac{1}{4\pi} \int_0^{2\pi} \mathrm{d}\varphi \int_0^{\pi} \mathrm{d}\vartheta \, \sin\vartheta e^{-\beta(-\omega_{\mathrm{L}} S_z(\vartheta,\varphi) - Q S_\theta^2(\vartheta,\varphi))}. \tag{C.6}$$

While obtaining the S_z expectation value is straightforward, the S_x case may seem less obvious. It is therefore convenient to do a change of coordinates

$$\begin{aligned} S_{z'}(\vartheta,\varphi) &= S_z(\vartheta,\varphi)\cos\theta - S_x(\vartheta,\varphi)\sin\theta, \\ S_{x'}(\vartheta,\varphi) &= S_x(\vartheta,\varphi)\cos\theta + S_z(\vartheta,\varphi)\sin\theta. \end{aligned} \tag{C.7}$$

Defining $h_{x'} = -\omega_{\mathrm{L}}\sin\theta$, $h_{z'} = -\omega_{\mathrm{L}}\cos\theta$, we then have that

$$\begin{aligned} \tilde{Z}_{\mathrm{S}}^{\mathrm{cl}} = \frac{1}{4\pi} \int_0^{2\pi} \mathrm{d}\varphi \int_0^{\pi} \mathrm{d}\vartheta \, \sin\vartheta \\ e^{-\beta(h_{z'} S_{z'}(\vartheta,\phi) + h_{x'} S_{x'}(\vartheta,\phi) - Q S_{z'}^2(\vartheta,\phi))}, \end{aligned} \tag{C.8}$$

and we can obtain the $S_{z'}$ and $S_{x'}$ expectation values as usual, i.e.

$$\left\langle S_{x',z'} \right\rangle = -\frac{1}{\beta} \frac{\partial}{\partial h_{x',z'}} \log \tilde{Z}_{\mathrm{S}}^{\mathrm{cl}}. \tag{C.9}$$

Finally, by linearity, we have that

$$\langle S_x \rangle = \langle S_{x'} \rangle \cos\theta - \langle S_{z'} \rangle \sin\theta, \tag{C.10}$$
$$\langle S_z \rangle = \langle S_{z'} \rangle \cos\theta + \langle S_{x'} \rangle \sin\theta.$$

C.2.2 Quantum case

For the quantum case we proceed in a completely analogous manner. We have that

$$\langle S_x \rangle = \mathrm{tr}^{\mathrm{qu}} \left[S_x e^{-\beta(-\omega_{\mathrm{L}} S_z + S_\theta B + H_{\mathrm{R}})} \right], \tag{C.11}$$
$$\langle S_z \rangle = \mathrm{tr}^{\mathrm{qu}} \left[S_z e^{-\beta(-\omega_{\mathrm{L}} S_z + S_\theta B + H_{\mathrm{R}})} \right].$$

Starting from the partition function

$$Z^{\mathrm{qu}}_{\mathrm{SR}} = \mathrm{tr}^{\mathrm{qu}} \left[e^{-\beta(-\omega_{\mathrm{L}} S_z + S_\theta B + H_{\mathrm{R}})} \right], \tag{C.12}$$

we define a new set of rotated operators,

$$S_{z'} = S_z \cos\theta - S_x \sin\theta, \tag{C.13}$$
$$S_{x'} = S_x \cos\theta + S_z \sin\theta,$$

and variables $h_{x'} = -\omega_{\mathrm{L}} \sin\theta$, $h_{z'} = -\omega_{\mathrm{L}} \cos\theta$, so that

$$Z^{\mathrm{qu}}_{\mathrm{SR}} = \mathrm{tr}^{\mathrm{qu}} [e^{-\beta(h_{z'} S_{z'} + h_{x'} S_{x'} + S_{z'} B + H_{\mathrm{R}})}]. \tag{C.14}$$

Then, we proceed in an analagous way as in (C.9) and (C.10).

C.2.3 Example: Ultrastrong limit

Let us consider the quantum ultrastrong partition function,

$$\tilde{Z}^{\mathrm{qu}}_{\mathrm{S,US}} = \cosh\left(\beta \omega_{\mathrm{L}} S_0 \cos\theta\right). \tag{C.15}$$

Following the procedure outlined above, we have that $h_{z'} = -\omega_{\mathrm{L}} \cos\theta$, and therefore

$$\tilde{Z}^{\mathrm{qu}}_{\mathrm{S,US}} = \cosh\left(\beta S_0 h_{z'}\right). \tag{C.16}$$

Therefore, the expectation values of the transformed observables are

$$\langle S_{x'} \rangle = -\frac{1}{\beta}\frac{\partial}{\partial h_{x'}} \log \tilde{Z}^{\mathrm{qu}}_{\mathrm{S,US}} = 0, \tag{C.17}$$

$$\begin{aligned}\langle S_{z'} \rangle &= -\frac{1}{\beta}\frac{\partial}{\partial h_{z'}} \log \tilde{Z}^{\mathrm{qu}}_{\mathrm{S,US}} = -S_0 \tanh\left(\beta S_0 h_{z'}\right) \\ &= -S_0 \tanh\left(\beta \omega_{\mathrm{L}} S_0 \cos\theta\right).\end{aligned} \tag{C.18}$$

Therefore, in the original variables we have

$$\langle S_x \rangle = S_0 \sin\theta \tanh\left(\beta \omega_{\mathrm{L}} S_0 \cos\theta\right), \tag{C.19}$$

$$\langle S_z \rangle = -S_0 \cos\theta \tanh\left(\beta \omega_{\mathrm{L}} S_0 \cos\theta\right), \tag{C.20}$$

in agreement with what is later obtained in Appendix C.7 directly from the MF in the ultra-strong limit.

C.3 Derivation of classical MF state for arbitrary coupling

In this section we derive the mean force Gibbs state of the classical spin for arbitrary coupling strength. As discussed in C.1, we discretise the environmental degrees of freedom, and thus we have for the total Hamiltonian, (78)

$$H_{\mathrm{tot}} = -\omega_{\mathrm{L}} S_z + \sum_{n=0}^{\infty} \left[\frac{1}{2}\left(P^2_{\omega_n} + \omega_n^2 X^2_{\omega_n}\right) + S_\theta C_{\omega_n} X_{\omega_n} \right]. \tag{C.21}$$

On 'completing the square', we get

$$H_{\mathrm{tot}} = -\omega_{\mathrm{L}} S_z + \sum_{n=0}^{\infty} \frac{1}{2} \left[P^2_{\omega_n} + \omega_n^2 \left(X_{\omega_n} - \frac{S_\theta C_{\omega_n}}{\omega_n^2} \right)^2 - \frac{(S_\theta C_{\omega_n})^2}{2\omega_n^2} \right]. \tag{C.22}$$

The partition function is then,

$$Z_{\mathrm{SR}}^{\mathrm{cl}} = \frac{1}{4\pi}\int_0^{2\pi} \mathrm{d}\varphi \int_0^{\pi} \mathrm{d}\vartheta \, \sin\vartheta e^{-\beta H_{\mathrm{eff}}} Z_{\mathrm{R}}^{\mathrm{cl}}. \tag{C.23}$$

Here, there appears an effective system Hamiltonian given by

$$H_{\mathrm{eff}} \equiv -\omega_{\mathrm{L}} S_z - Q S_\theta^2 \tag{C.24}$$

where the reorganization energy Q, is given by Eq. (80) of the main text, and

$$Z_{\mathrm{R}}^{\mathrm{cl}} = \prod_n \int_{-\infty}^{\infty} \mathrm{d}X_{\omega_n} \int_{-\infty}^{\infty} \mathrm{d}P_{\omega_n} \, e^{-\frac{1}{2}\beta\left(P_{\omega_n}^2 + \omega_n^2\left(X_{\omega_n} - \frac{S_\theta C_{\omega_n}}{\omega_n^2}\right)^2\right)}, \tag{C.25}$$

is the partition function for the reservoir only. Note that, despite seemingly depending on the spin coordinates, this last integral coincides with the reservoir partition function since once one carries out the Gaussian integral, the dependence on S_θ vanishes.

While it is possible to derive an expression for Z_{R}, its details are not needed as it depends solely on reservoir variables and can be divided out to yield the system's MF partition function,

$$\tilde{Z}_{\mathrm{S}}^{\mathrm{cl}} = \frac{Z_{\mathrm{SR}}^{\mathrm{cl}}}{Z_{\mathrm{R}}^{\mathrm{cl}}} = \frac{1}{4\pi}\int_0^{2\pi} \mathrm{d}\varphi \int_0^{\pi} \mathrm{d}\vartheta \, \sin\vartheta e^{-\beta H_{\mathrm{eff}}}, \tag{C.26}$$

where H_{eff} includes all spin terms independent of the coordinates of the environment. Finally, the MF is given by

$$\tau_{\mathrm{MF}} = \frac{1}{\tilde{Z}_{\mathrm{S}}^{\mathrm{cl}}} e^{-\beta H_{\mathrm{eff}}}, \tag{C.27}$$

which is precisely Eq. (82) of the main text.

In terms of polar coordinates, we have $S_\theta = S_0\left(\cos\vartheta\cos\theta - \sin\vartheta\cos\varphi\sin\theta\right)$, and then

$$\begin{aligned} H_{\mathrm{eff}}(\vartheta,\varphi) = &-\omega_{\mathrm{L}} S_0 \cos\vartheta \\ &- S_0^2 Q\left(\cos\theta\cos\vartheta - \sin\theta\sin\vartheta\cos\varphi\right)^2. \end{aligned} \tag{C.28}$$

The equilibrium state of the spin is then entirely determined by $\tilde{Z}_{\mathrm{S}}^{\mathrm{cl}}$. The classical expectation values for the spin components S_z and S_x are then given by

$$\begin{aligned}\langle s_z\rangle &= \frac{\langle S_z\rangle}{S_0} \\ &= \frac{1}{\tilde{Z}_{\mathrm{S}}^{\mathrm{cl}}}\int_0^{2\pi}\mathrm{d}\varphi\int_0^{\pi}\mathrm{d}\vartheta\,\sin\vartheta\cos\vartheta e^{-\beta H_{\mathrm{eff}}(\vartheta,\varphi)}\end{aligned} \tag{C.29}$$

$$\begin{aligned}\langle s_x\rangle &= \frac{\langle S_x\rangle}{S_0} \\ &= \frac{1}{\tilde{Z}_{\mathrm{S}}^{\mathrm{cl}}}\int_0^{2\pi}\mathrm{d}\varphi\,\cos\varphi\int_0^{\pi}\mathrm{d}\vartheta\,\sin^2\vartheta e^{-\beta H_{\mathrm{eff}}(\vartheta,\varphi)}.\end{aligned} \tag{C.30}$$

The integral expressions for the expectation values above cannot in general be expressed in a closed form, but can be readily evaluated numerically for arbitrary coupling strength Q.

C.4 Quantum–classical correspondence for the MF partition functions

Starting from equation (C.75) of the main text, we now "complete the square" for the combination

$$h_{\mathrm{R}} + s_\theta\int_0^\infty\mathrm{d}\omega\,C_\omega\sqrt{S_0}x_\omega, \tag{C.31}$$

to arrive at

$$\frac{1}{2}\int_0^\infty\mathrm{d}\omega\left(p_\omega^2+\omega^2\left(x_\omega+s_\theta\frac{C_\omega\sqrt{S_0}}{\omega^2}\right)^2\right) - s_\theta^2 S_0 Q(S_0) = h_{\mathrm{R}}^{\mathrm{shift}} - s_\theta^2 S_0 Q(S_0), \tag{C.32}$$

where $Q(S_0) = \int_0^\infty\mathrm{d}\omega\,C_\omega^2(S_0)/(2\omega^2)$ is the reorganisation energy, see (80). Note that because of the scaling $C_\omega \propto 1/\sqrt{S_0}$, the product $S_0Q(S_0) = \alpha\,\omega_{\mathrm{L}}$ is independent of S_0. Here, we have defined the reservoir Hamiltonian

$$h_{\mathrm{R}}^{\mathrm{shift}} = \frac{1}{2}\int_0^\infty\mathrm{d}\omega\left(p_\omega^2+\omega^2\left(x_\omega+s_\theta\frac{C_\omega\sqrt{S_0}}{\omega^2}\right)^2\right), \tag{C.33}$$

where the oscillator centres have been shifted.

Applying (83) to the total spin-reservoir Hamiltonian H_{tot}, and immediately

taking the reservoir trace on both sides, gives

$$\begin{aligned}\lim_{S_0\to\infty}\frac{\hbar}{2S_0+\hbar}Z_{\mathrm{SR}}^{\mathrm{qu}}(\beta,S_0,\alpha) &= \lim_{S_0\to\infty}\frac{\hbar}{2S_0+\hbar}\,\mathrm{tr}_{\mathrm{SR}}^{\mathrm{qu}}\left[e^{-\beta'\left(-\omega_{\mathrm{L}}s_z+h_{\mathrm{R}}^{\mathrm{shift}}-s_\theta^2\,\alpha\,\omega_{\mathrm{L}}\right)}\right]\\ &= \lim_{S_0\to\infty}\frac{1}{4\pi}\int_0^{2\pi}\mathrm{d}\varphi\int_0^{\pi}\mathrm{d}\vartheta\,\sin\vartheta\\ &\qquad \mathrm{tr}_{\mathrm{R}}^{\mathrm{qu}}\left[e^{-\beta'\left(-\omega_{\mathrm{L}}\cos\vartheta+h_{\mathrm{R}}^{\mathrm{shift}}-s_\theta^2(\vartheta,\phi')\,\alpha\,\omega_{\mathrm{L}}\right)}\right]\\ &= \lim_{S_0\to\infty}\frac{1}{4\pi}\int_0^{2\pi}\mathrm{d}\varphi\int_0^{\pi}\mathrm{d}\vartheta\,\sin\vartheta\\ &\qquad e^{-\beta'\left(-\omega_{\mathrm{L}}\cos\vartheta-s_\theta^2(\vartheta,\phi')\,\alpha\,\omega_{\mathrm{L}}\right)}\,\mathrm{tr}_{\mathrm{R}}^{\mathrm{qu}}\left[e^{-\beta' h_{\mathrm{R}}^{\mathrm{shift}}}\right],\end{aligned}\tag{C.34}$$

where the trace over the reservoir now factors out and

$$s_\theta(\vartheta,\phi') = \cos\theta\cos\vartheta-\sin\theta\cos\varphi\sin\vartheta.\tag{C.35}$$

The reservoir trace factor gives

$$\begin{aligned}\mathrm{tr}_{\mathrm{R}}^{\mathrm{qu}}\left[e^{-\beta' h_{\mathrm{R}}^{\mathrm{shift}}}\right] &= \mathrm{tr}_{\mathrm{R}}^{\mathrm{qu}}\left[e^{-\beta\frac{1}{2}\int_0^\infty\mathrm{d}\omega\left(P_\omega^2+\omega^2(X_\omega+\mu_\omega)^2\right)}\right]\\ &= Z_{\mathrm{R}}^{\mathrm{qu}}(\beta),\end{aligned}\tag{C.36}$$

with $\mu_\omega = S_\theta\frac{C_\omega}{\omega^2}$ a shift in the centre position of the oscillators. The operators $X_\omega+\mu_\omega$ have the same commutation relations with the P_ω as the X_ω themselves. Thus such a shift does not affect the trace and the result is the bare quantum reservoir partition function at inverse temperature β, i.e. $Z_{\mathrm{R}}^{\mathrm{qu}}(\beta)$.

Dividing by $Z_{\mathrm{R}}^{\mathrm{qu}}(\beta)$ on both sides, putting it all together, we find

$$\lim_{S_0\to\infty}\frac{\hbar}{2S_0+\hbar}\frac{Z_{\mathrm{SR}}^{\mathrm{qu}}(\beta,S_0,\alpha)}{Z_{\mathrm{R}}^{\mathrm{qu}}(\beta)} = \frac{1}{4\pi}\int_0^{2\pi}\mathrm{d}\varphi\int_0^{\pi}\mathrm{d}\vartheta\,\sin\vartheta\,e^{-\beta'\left(-\omega_{\mathrm{L}}\cos\vartheta-s_\theta^2(\vartheta,\phi')\,\alpha\,\omega_{\mathrm{L}}\right)},\tag{C.37}$$

where we have dropped the limit symbol since there is no dependence on S_0.

Now we may replace again $\beta' = \beta S_0$, and the RHS emerges as the spin's classical mean force partition function $\tilde{Z}_{\mathrm{S}}^{\mathrm{cl}}(\beta S_0,\alpha)$, cf. (82), where the classical trace is taken according to (C.2). Moreover, the fraction of total quantum partition function divided by bare reservoir partition function is the quantum mean force

partition function [212, 213]. Thus, we conclude:

$$\lim_{S_0\to\infty} \frac{\hbar}{2S_0+\hbar}\,\tilde{Z}_{\mathrm{S}}^{\mathrm{qu}}(\beta,S_0,\alpha) = \lim_{S_0\to\infty} \frac{\hbar}{2S_0+\hbar}\frac{Z_{\mathrm{SR}}^{\mathrm{qu}}(\beta,S_0,\alpha)}{Z_{\mathrm{R}}^{\mathrm{qu}}(\beta)} = \tilde{Z}_{\mathrm{S}}^{\mathrm{cl}}(\beta S_0,\alpha). \tag{C.38}$$

C.5 Quantum Reaction Coordinate mapping

The Reaction Coordinate mapping method [219, 220, 221, 222] is a technique for dealing with systems strongly coupled to bosonic environments. To do so, it isolates a single collective environmental degree of freedom, the so called "reaction coordinate" (RC), that interacts with the system via an effective Hamiltonian. The rest of the environmental degrees of freedom manifest as a new bosonic environment coupled to the RC. Concretely, for our total Hamiltonian (78), the effective Hamiltonian that we have to consider is

$$H_{\mathrm{tot}}^{\mathrm{RC}} = H_{\mathrm{S}} + H_{\mathrm{RC}} + H_{\mathrm{int}}^{\mathrm{RC}} + H_{\mathrm{int}}^{\mathrm{res}} + H_{\mathrm{res}}, \tag{C.39}$$

where H_{RC} is the Hamiltonian of the RC mode,

$$H_{\mathrm{RC}} = \hbar\Omega_{\mathrm{RC}} a^\dagger a, \tag{C.40}$$

with $a^\dagger$ the creation operator of a quantum harmonic oscillator of frequency Ω_{RC}; $H_{\mathrm{int}}^{\mathrm{RC}}$ is the spin–RC interaction

$$H_{\mathrm{int}}^{\mathrm{RC}} = \lambda_{\mathrm{RC}} S_\theta (a + a^\dagger), \tag{C.41}$$

where λ_{RC} determines the the coupling strength between the RC mode and the spin; $H_{\mathrm{res}} = \int \mathrm{d}\omega (p_\omega^2 + \omega^2 q_\omega^2)/2$ is the Hamiltonian of the residual bosonic bath; and finally the residual bath-RC interaction $H_{\mathrm{int}}^{\mathrm{res}}$ is

$$H_{\mathrm{int}}^{\mathrm{res}} = (a + a^\dagger) \int_0^\infty \mathrm{d}\omega \, \sqrt{2\omega J_{\mathrm{RC}}}\, q_\omega, \tag{C.42}$$

with J_{RC} the spectral density of the residual bath.

Given H_{tot}, for an appropriate choice of J_{RC} (which depends on the original Hamiltonian spectral density and coupling), it has been proven that the reduced

dynamics of the spin under $H_{\rm tot}$ are exactly the same as those of the spin under the effective Hamiltonian $H_{\rm tot}^{\rm RC}$ [221]. In general, the mapping between the original spectral density, J_ω, and that of the RC Hamiltonian, $J_{\rm RC}$, is hard to find. However, one particular case were there is a simple closed form for $J_{\rm RC}$ is that of a Lorentzian spectral density J_ω (see main text). In such case, the $J_{\rm RC}$ spectral density is exactly Ohmic [219, 220, 221], i.e. has the form

$$J_{\rm RC} = \gamma_{\rm RC}\omega e^{-\omega/\omega_{\rm c}}, \qquad \omega_{\rm c} \to \infty. \tag{C.43}$$

Furthermore, the RC effective Hamiltonian parameters ($\Omega_{\rm RC}$, $\lambda_{\rm RC}$ and $\gamma_{\rm RC}$) are given in terms of the Lorentzian parameters by

$$\Omega_{\rm RC} = \omega_0, \tag{C.44}$$

$$\lambda_{\rm RC} = \sqrt{Q\omega_0}, \tag{C.45}$$

$$\gamma_{\rm RC} = \frac{\Gamma}{2\pi\omega_0}. \tag{C.46}$$

Noticeably, by appropriately choosing Q, Γ, and ω_0, we can have an initial Hamiltonian with arbitrarily strong coupling to the full environment (i.e. arbitrarily strong Q), while having arbitrarily small coupling to the residual bath of the RC Hamiltonian (i.e. arbitrarily small $\gamma_{\rm RC}$).

As mentioned, it has been shown that the reduced spin dynamics under $H_{\rm tot}$ with Lorentzian spectral density (see main text) is exactly the same as the reduced spin dynamics under $H_{\rm tot}^{\rm RC}$ with spectral density (C.43). In particular, the steady state of the spin will also be the same. Therefore, it is reasonable to expect that the spin MF state obtained with $H_{\rm tot}$ will be the same as the spin MF state for $H_{\rm tot}^{\rm RC}$, i.e.

$$\tau_{\rm MF} = \tilde{Z}_{\rm S}^{-1}\,{\rm tr}_{\rm R}[e^{-\beta H_{\rm tot}}] = \tilde{Z}_{\rm S}'^{-1}\,{\rm tr}_{\rm R}[e^{-\beta H_{\rm tot}^{\rm RC}}]. \tag{C.47}$$

We now assume that $\gamma_{\rm RC}$ is arbitrarily small, so that the MF state is simply going to be given by the Gibbs state of spin+RC, i.e.

$$\begin{aligned}\tau_{\rm MF} &= \tilde{Z}_{\rm S}'^{-1}\,{\rm tr}_{\rm R}[e^{-\beta H_{\rm tot}^{\rm RC}}] \\ &\approx \tilde{Z}_{\rm S}''^{-1}\,{\rm tr}_{\rm R}\left[e^{-\beta\left(H_{\rm S}+\Omega_{\rm RC}a^\dagger a+\lambda_{\rm RC}S_\theta(a+a^\dagger)\right)}\right].\end{aligned} \tag{C.48}$$

It is key here to observe that the condition $\gamma_{\mathrm{RC}} \to 0$ does not imply any constraint on the coupling strength to the original environment, since we can always choose Γ and ω_0 so that γ_{RC} is arbitrarily small, while allowing Q to be arbitrarily large.

Finally, to numerically obtain the MF state, since unfortunately (C.48) does not have a general closed form, we numerically evaluate (C.48) by diagonalising the full Hamiltonian and then taking the partial trace over the RC. To numerically diagonalise this Hamiltonian we have to choose a cutoff on the number of energy levels of the RC harmonic oscillator. This cutoff was chosen by increasing the number of levels until observing convergence of the numerical results.

C.6 Quantum to classical limit in the weak coupling approximation

In this section we explicitly compute the large spin limit for the weak coupling expressions of the classical and quantum mean force Gibbs states. These results are used in the characterisation of the different coupling regimes.

Since we are going to perform perturbative expansions in the coupling strength, in what follows we introduce, for book-keeping purposes, an adimensional parameter λ in the interaction, so that H_{int} now reads

$$H_{\mathrm{int}} = \lambda S_\theta \int_0^\infty \mathrm{d}\omega \, C_\omega X_\omega. \tag{C.49}$$

This will allow us to properly keep track of the order of each term in the expansion. Finally, at the end of the calculations we will take $\lambda = 1$.

C.6.1 Classical spin: weak coupling

Here, we derive the classical weak coupling expectation values starting from the exact MF found in C.3. The effective Hamiltonian, with the inclusion of the parameter λ now reads

$$H_{\mathrm{eff}} = -\omega_{\mathrm{L}} S_z - \lambda^2 Q S_\theta^2. \tag{C.50}$$

For weak coupling, the expressions for $\tilde{Z}_{\mathrm{S}}^{\mathrm{cl}}$, $\langle S_z \rangle$ and $\langle S_x \rangle$ can be approximated by treating the term $\lambda^2 S_0^2 Q$ as a perturbation. Therefore, expanding $\exp[-\beta H_{\mathrm{eff}}]$ to

lowest order in λ we have

$$e^{-\beta H_{\text{eff}}} = e^{\beta\omega_{\text{L}} S_0 \cos\vartheta}\Big[1 + \beta\lambda^2 S_0^2 Q\left(\cos\theta\cos\vartheta - \sin\theta\sin\vartheta\cos\varphi\right)^2\Big] + \mathscr{O}(\lambda^4), \quad \text{(C.51)}$$

from which we can determine the weak coupling limit of the classical spin partition function and spin expectation values.

Standard Gibbs results for a classical spin First, here we write the partition function and spin expectation values for a classical spin in the standard Gibbs state for the bare Hamiltonian H_{S} (i.e. in the limit of vanishing coupling, $\lambda = 0$). These expressions will be useful to later on to write the second order corrections.

For the partition function we have that

$$\begin{aligned} Z_0^{\text{cl}} &= \frac{1}{4\pi}\int_0^{2\pi}\mathrm{d}\varphi\int_0^{\pi}\mathrm{d}\vartheta\ \sin\vartheta\exp[\beta\omega_{\text{L}} S_0\cos\vartheta] \\ &= \frac{\sinh(\beta\omega_{\text{L}} S_0)}{\beta\omega_{\text{L}} S_0}. \end{aligned} \quad \text{(C.52)}$$

The expectation value of S_x is trivially 0 by symmetry, i.e.

$$\begin{aligned} \langle S_x\rangle_0 &= \frac{1}{Z_0^{\text{cl}}} S_0\int_0^{2\pi}\mathrm{d}\varphi\ \cos\varphi\int_0^{\pi}\mathrm{d}\vartheta\ \sin^2\vartheta e^{\beta\omega_{\text{L}} S_0\cos\vartheta} \quad \text{(C.53)} \\ &= 0. \end{aligned}$$

For the expectation value of the powers of S_z (which will be useful later), we have

$$\langle S_z^n\rangle_0 = \frac{2\pi}{Z_0^{\text{cl}}} S_0^n\int_0^{\pi}\mathrm{d}\vartheta\ \sin\vartheta\cos^n\vartheta\, e^{\beta\omega_{\text{L}} S_0\cos\vartheta}. \quad \text{(C.54)}$$

In particular, we find

$$\langle S_z\rangle_0 = S_0\coth(\beta\omega_{\text{L}} S_0) - \frac{1}{\beta\omega_{\text{L}}}, \quad \text{(C.55)}$$

$$\langle S_z^2\rangle_0 = S_0^2 - \frac{2S_0\coth(\beta\omega_{\text{L}} S_0)}{\beta\omega_{\text{L}}} + \frac{2}{(\beta\omega_{\text{L}})^2}, \quad \text{(C.56)}$$

$$\begin{aligned} \langle S_z^3\rangle_0 &= S_0^3\coth(\beta\omega_{\text{L}} S_0) - \frac{3S_0^2}{\beta\omega_{\text{L}}} \quad \text{(C.57)} \\ &\quad + \frac{6S_0\coth(\beta\omega_{\text{L}} S_0)}{(\beta\omega_{\text{L}})^2} - \frac{6}{(\beta\omega_{\text{L}})^3}. \end{aligned}$$

Classical spin partition function for weak coupling Expanding the partition function to second order in λ we find that

$$\tilde{Z}_{\mathrm{S}}^{\mathrm{cl}} = \frac{1}{4\pi}\int_0^{2\pi}\mathrm{d}\varphi\int_0^{\pi}\mathrm{d}\vartheta\,\sin\vartheta\left[e^{\beta\omega_{\mathrm{L}}S_0\cos\vartheta} + \frac{\beta\lambda^2 S_0^2 Q}{4\pi}e^{\beta\omega_{\mathrm{L}}S_0\cos\vartheta}\big(\cos\theta\cos\vartheta - \sin\theta\sin\vartheta\cos\varphi\big)^2\right] + \mathscr{O}(\lambda^4). \tag{C.58}$$

The first term can be recognised as the partition function for the bare system, Z_0^{cl}. The φ' integral in the second term is straightforward to perform,

$$\tilde{Z}_{\mathrm{S}}^{\mathrm{cl}} = Z_0^{\mathsf{cl}} + \frac{1}{2}\beta\lambda^2 S_0^2 Q\int_0^{\pi}\mathrm{d}\vartheta\,\sin\vartheta e^{\beta\omega_{\mathrm{L}}S_0\cos\vartheta}\big[(3\cos^2\theta-1)\cos^2\vartheta + \sin^2\theta\big] + \mathscr{O}(\lambda^4). \tag{C.59}$$

We typically require the inverse of the partition function, which to lowest order in the perturbation is

$$\tilde{Z}_{\mathrm{S}}^{\mathrm{cl}} = (Z_0^{\mathsf{cl}})^{-1}\left[1 - \pi\beta\lambda^2 S_0^2 Q Z_0^{-1}\int_0^{\pi}\mathrm{d}\vartheta\,\sin\vartheta e^{\beta\omega_{\mathrm{L}}S_0\cos\vartheta}\big((3\cos^2\theta-1)\cos^2\vartheta + \sin^2\theta\big)\right] + \mathscr{O}(\lambda^4). \tag{C.60}$$

Now turning to the expectation value $\langle S_z\rangle$, given in Eq. (C.29), and carrying out the same lowest order expansion we get

$$\langle S_z\rangle = \langle S_z\rangle_0 + \frac{1}{2}\beta\lambda^2 Q\left[(3\cos^2\theta-1)(\langle S_z^3\rangle_0 - \langle S_z\rangle_0\langle S_z^2\rangle_0)\right] + \mathscr{O}(\lambda^4). \tag{C.61}$$

This result will be compared later to the quantum weak coupling result obtained in the large spin (classical) limit.

Classical $\langle S_x\rangle$ for weak coupling A similar calculation can be followed for $\langle S_x\rangle$, the main difference being in the handling of the φ' integral. Thus, we find

$$\langle S_x\rangle = -\tfrac{1}{2}\sin 2\theta\beta\lambda^2 Q\left(\langle S_z\rangle_0 S_0^2 - \langle S_z^3\rangle_0\right) + \mathscr{O}(\lambda^4), \tag{C.62}$$

where we have used that $Z_0/\tilde{Z}_{\mathrm{S}}^{\mathrm{cl}} = 1$ to lowest order.

Using the zeroth order expressions for $\langle S_z\rangle_0$ and $\langle S_z^3\rangle_0$ from (C.55) we get the

result in terms of the scaled temperature $\beta' = \beta S_0$

$$\langle s_x \rangle = -\frac{\sin 2\theta \lambda^2 S_0 Q}{\omega_{\rm L}} \left(1 - \frac{3\coth(\beta'\omega_{\rm L})}{\beta'\omega_{\rm L}} + \frac{3}{(\beta'\omega_{\rm L})^2} \right) + \mathscr{O}(\lambda^4). \tag{C.63}$$

This result will be compared later to the quantum weak coupling result obtained in the large spin (classical) limit.

C.6.2 Quantum spin: weak coupling

In general, the quantum mean force Gibbs state is given by

$$\tau_{\rm MF} = \frac{{\rm tr}_{\rm R}^{\rm qu}\left[e^{-\beta H_{\rm tot}}\right]}{Z_{\rm tot}^{\rm qu}}, \tag{C.64}$$

with $H_{\rm tot}$ given by Eq. (78) of the main text. Unfortunately, determining the form of $\tau_{\rm MF}$ and the various expectation values for the spin components is unfeasible in the general case, but limiting forms are available. Here we derive the spin expectation values in the weak coupling limit, and then later on take the large spin limit to explicitly verify the quantum-to-classical transition.

Standard Gibbs results for a quantum spin Here, we present the results of the standard Gibbs state for the quantum spin (i.e. in the limit of vanishing coupling, $\lambda = 0$). The Gibbs state for the system's bare Hamiltonian is

$$\tau_{\rm S} = \frac{e^{\beta\omega_{\rm L} S_z}}{Z_{\rm S}^{\rm qu}}, \quad Z_{\rm S}^{\rm qu} = {\rm tr}\left[e^{\beta\omega_{\rm L} S_z}\right]. \tag{C.65}$$

We also have that $[\tau_{\rm S}, S_z] = 0$. The trace is readily evaluated, yielding the partition function

$$Z_0^{\mathsf{qu}} = \frac{\sinh \beta\omega_{\rm L}(S_0 + \frac{\hbar}{2})}{\sinh \frac{\hbar}{2}\beta\omega_{\rm L}}, \tag{C.66}$$

from which we can derive the expectation values of S_z, S_z^2 and S_z^3,

$$\langle S_z^n \rangle_0 = \frac{1}{Z_0^{\mathsf{qu}}} \frac{{\rm d}^n}{{\rm d}(\beta\omega_{\rm L})^n} Z_0^{\mathsf{qu}}. \tag{C.67}$$

We find,

$$\langle S_z\rangle_0 = (S_0+\tfrac{\hbar}{2})\coth\Big(\beta\omega_{\rm L}(S_0+\tfrac{\hbar}{2})\Big) - \tfrac{\hbar}{2}\coth\Big(\tfrac{\hbar}{2}\beta\omega_{\rm L}\Big) \tag{C.68}$$

$$\begin{aligned}\langle S_z^2\rangle_0 &= (S_0+\tfrac{\hbar}{2})^2 \\ &\quad - \hbar(S_0+\tfrac{\hbar}{2})\coth\Big(\tfrac{\hbar}{2}\beta\omega_{\rm L}\Big)\coth\Big(\beta\omega_{\rm L}(S_0+\tfrac{\hbar}{2})\Big) \\ &\quad + \tfrac{\hbar^2}{4}\Big(2\coth^2(\tfrac{\hbar}{2}\beta\omega_{\rm L})-1\Big)\end{aligned} \tag{C.69}$$

$$\begin{aligned}\langle S_z^3\rangle_0 &= (S_0+\tfrac{\hbar}{2})^3\coth\Big(\beta\omega_{\rm L}(S_0+\tfrac{\hbar}{2})\Big) \\ &\quad - \tfrac{3\hbar}{2}(S_0+\tfrac{\hbar}{2})^2\coth\Big(\tfrac{\hbar}{2}\beta\omega_{\rm L}\Big) \\ &\quad + \tfrac{3\hbar^2}{4}(S_0+\tfrac{\hbar}{2})\coth\Big(\beta\omega_{\rm L}(S_0+\tfrac{\hbar}{2})\Big) \\ &\qquad\qquad \Big(2\coth^2(\tfrac{\hbar}{2}\beta\omega_{\rm L})-1\Big) \\ &\quad - \tfrac{3\hbar^3}{4}\coth^3(\tfrac{\hbar}{2}\beta\omega_{\rm L}) + \tfrac{5\hbar^3}{8}\coth\Big(\tfrac{\hbar}{2}\beta\omega_{\rm L}\Big).\end{aligned} \tag{C.70}$$

General form of weak coupling density operator For a total Hamiltonian $H_{\rm S}+H_{\rm R}+H_{\rm int}$ with interaction of the form $H_{\rm int}=\lambda XB$, the general expression for the *unnormalised* mean force state to second order in the interaction is given by [178]

$$\begin{aligned}\tilde\rho^{(2)} &= \tau_{\rm S} \\ &\quad + \lambda^2\sum_n\Big(\Big[X_n^\dagger,\tau_{\rm S}X_n\Big]\,A'_\beta(\omega_n) + \beta\tau_{\rm S}X_nX_n^\dagger\,A_\beta(\omega_n)\Big) \\ &\quad + \lambda^2\sum_{m\neq n}\omega_{mn}^{-1}\Big(\Big[X_m,X_n^\dagger\tau_{\rm S}\Big]+\Big[\tau_{\rm S}X_n,X_m^\dagger\Big]\Big)\,A_\beta(\omega_n),\end{aligned} \tag{C.71}$$

where the system operator X is expanded in terms of the energy eigenoperators X_n

$$X=\sum_n X_n, \tag{C.72}$$

with $[H_{\rm S},X_n]=\omega_nX_n$, and ω_n are Bohr frequencies for the system. We have $X_n^\dagger = X_{-n}$ and $\omega_n=-\omega_{-n}$. The quantities $A_\beta(\omega_n)$ are determined by the correlation properties of the reservoir operator B and are given by

$$A_\beta(\omega_n)=\int_0^\infty{\rm d}\omega\,J_\omega\left(\frac{n_\beta(\omega)+1}{\omega-\omega_n}-\frac{n_\beta(\omega)}{\omega+\omega_n}\right), \tag{C.73}$$

$$A'_\beta(\omega_n)=\int_0^\infty{\rm d}\omega\,\frac{J_\omega}{\hbar}\left(\frac{n_\beta(\omega)+1}{(\omega-\omega_n)^2}+\frac{n_\beta(\omega)}{(\omega+\omega_n)^2}\right). \tag{C.74}$$

We can separate out the particular case of $\omega_n = 0$, for which we find

$$A_\beta(0) = \int_0^\infty \mathrm{d}\omega \, \frac{J_\omega}{\omega} = Q. \tag{C.75}$$

It turns out that we will require various symmetric and antisymmetric combinations of $A_\beta(\omega_n)$ and $A'_\beta(\omega_n)$. [Note that in the following (and in the initial definition of the quantity $A'_\beta(\omega_n)$), the dash indicates a derivative wrt to the argument ω_n. Thus the quantity $A'_\beta(-\omega_n)$ is a derivative wrt $-\omega_n$, i.e., $A'_\beta(-\omega_n) = -\mathrm{d}A_\beta(-\omega_n)/\mathrm{d}\omega_n$, whereas, as usual, $A'_\beta(\omega_n) = \mathrm{d}A_\beta(\omega_n)/\mathrm{d}\omega_n$ etc.] Therefore, we define

$$\begin{aligned}
\Sigma(\omega_n) &= A_\beta(\omega_n) + A_\beta(-\omega_n) \\
&= 2\int_0^\infty \mathrm{d}\omega \, J_\omega \frac{\omega}{\omega^2 - \omega_n^2} && \text{(C.76)} \\
\Delta_\beta(\omega_n) &= A_\beta(\omega_n) - A_\beta(-\omega_n) \\
&= 2\omega_n \int_0^\infty \mathrm{d}\omega \, J_\omega \frac{1}{\omega^2 - \omega_n^2} \coth\left(\tfrac{1}{2}\beta\hbar\omega\right) && \text{(C.77)} \\
\Delta'_\beta(\omega_n) &= A'_\beta(\omega_n) + A'_\beta(-\omega_n) \\
&= 2\int_0^\infty \mathrm{d}\omega \, \frac{J_\omega}{\hbar} \frac{(\omega^2 + \omega_n^2)}{(\omega^2 - \omega_n^2)^2} \coth\left(\tfrac{1}{2}\beta\hbar\omega\right) && \text{(C.78)} \\
\Sigma'(\omega_n) &= A'_\beta(\omega_n) - A'_\beta(-\omega_n) \\
&= 4\omega_n \int_0^\infty \mathrm{d}\omega \, \frac{J_\omega}{\hbar} \frac{\omega}{(\omega^2 - \omega_n^2)^2}. && \text{(C.79)}
\end{aligned}$$

Normalising the second order MF state From (C.71) we get the second order partition function

$$\tilde{Z}_{\mathrm{S}}^{(2)} = \mathrm{tr}\left[\tilde{\rho}^{(2)}\right] = 1 + \beta\lambda^2 \sum_n \mathrm{tr}\left[\tau_{\mathrm{S}} X_n X_n^\dagger\right] A_\beta(\omega_n). \tag{C.80}$$

This can be used directly to evaluate the second order expectation value $\langle S_z \rangle^{(2)}$, but instead we will proceed to derive the second order MF state. This normalised state can be arrived at as in [178], where a binomial approximation in used. Those expressions however seem to imply that the validity of the approximation depends on the temperature, with the approximation breaking down at low enough temperatures. Here we proceed in an alternative way that shows that there is no such limitation.

The exact density operator is

$$\tau_{\mathrm{MF}}(\lambda) = \frac{\tilde{\rho}(\lambda)}{\tilde{Z}_{\mathrm{S}}^{\mathrm{qu}}(\lambda)}, \tag{C.81}$$

where the dependence on λ is made explicit, and write

$$\tau_{\mathrm{MF}}(\lambda) = \tau_{\mathrm{MF}}(0) + \tfrac{1}{2}\lambda^2 \frac{\mathrm{d}^2\tau_{\mathrm{MF}}}{\mathrm{d}\lambda^2}(0) + \mathscr{O}(\lambda^4), \tag{C.82}$$

where $\tau_{\mathrm{MF}}(0) = \tau_{\mathrm{S}}$ is the Gibbs state of the system in the limit of vanishingly small system-reservoir coupling, and it has been recognised that odd order contributions will vanish.

From this we also find

$$\tilde{Z}_{\mathrm{S}}^{\mathrm{qu}}(\lambda) = 1 + \tfrac{1}{2}\lambda^2 \frac{\mathrm{d}^2\tilde{Z}_{\mathrm{S}}^{\mathrm{qu}}}{\mathrm{d}\lambda^2}(0) + \mathscr{O}(\lambda^4). \tag{C.83}$$

If we now do a Taylor series expansion of $\tau_{\mathrm{MF}}(\lambda)$ we find, using $\tilde{Z}_{\mathrm{S}}^{\mathrm{qu}}(0) = 1$,

$$\begin{aligned}
\tau_{\mathrm{MF}}(\lambda) &= \tau_{\mathrm{S}} + \tfrac{1}{2}\lambda^2 \left(\frac{\mathrm{d}^2\tilde{\rho}}{\mathrm{d}\lambda^2}(0) - \frac{\mathrm{d}^2\tilde{Z}_{\mathrm{S}}^{\mathrm{qu}}}{\mathrm{d}\lambda^2}(0)\tau_{\mathrm{S}} \right) \mathscr{O}(\lambda^4) \\
&= \tau_{\mathrm{S}} + \lambda^2 \sum_n \left[\left[X_n^\dagger, \tau_{\mathrm{S}} X_n \right] A'_\beta(\omega_n) + \beta\tau_{\mathrm{S}} \left(X_n X_n^\dagger - \mathrm{tr}\left[\tau_{\mathrm{S}} X_n X_n^\dagger \right] \right) A_\beta(\omega_n) \right] \\
&\quad + \sum_{m\neq n} \left(\left[X_m, X_n^\dagger \tau_{\mathrm{S}} \right] + \left[\tau_{\mathrm{S}} X_n, X_m^\dagger \right] \right) \frac{A_\beta(\omega_n)}{\omega_{nm}} + \mathscr{O}(\lambda^4).
\end{aligned} \tag{C.84}$$

We regain the expressions found in [178], but without having to consider any restrictions on β. In contrast, the binomial expansion based derivation of [178] seems to imply that irrespective of the choice of coupling strength, there will always be a temperature below which the binomial approximation will fail and (C.84) can lead to incorrect results below this temperature. But this argument cannot be sustained as the validity of the second order expansion is not constrained by any lower temperature limit implied by the binomial expansion as it can be obtained without making this approximation.

What we now have is the necessary requirement that (for some definition of

the norm $||\dots||$ of the operators involved)

$$\tfrac{1}{2}\lambda^2 \left|\left| \left(\frac{\mathrm{d}^2\tau_{\mathrm{MF}}}{\mathrm{d}\lambda^2}(0) - \tau_{\mathrm{S}} \frac{\mathrm{d}^2\tilde{Z}_{\mathrm{S}}^{\mathrm{qu}}}{\mathrm{d}\lambda^2}(0) \right) \right|\right| \ll \left|\left|\tau_{\mathrm{S}}\right|\right|, \tag{C.85}$$

for the second order result (C.84) to be valid. This of course is not a sufficient condition as the higher order terms, $\mathscr{O}(\lambda^4)$, are not guaranteed to be negligible.

The concern is the low temperature limit $\beta \to \infty$, where the term linear in β seems to imply linear divergence so the condition (C.85) cannot be met. However, it can be shown that in this limit the second order correction term in (C.84) actually vanishes [178]. It also does so for $\beta \to 0$, the high temperature limit, so there might be an intermediate temperature for which the condition (C.85) is not satisfied, this then requiring a weaker interaction coupling strength.

The conclusion then is that for sufficiently weak coupling, the result (C.84) will hold true for all temperatures.

To evaluate the second order expression for the normalised density operator given by (C.84) we need to expand $X = S_\theta$ in terms of the energy eigenoperators X_n,

$$\begin{aligned} X &= S_z \cos\theta - S_x \sin\theta \\ &= -\tfrac{1}{2}\sin\theta S_- + \cos\theta S_z - \tfrac{1}{2}\sin\theta S_+, \end{aligned} \tag{C.86}$$

so we can identify, from $X = X_{-1} + X_0 + X_{+1}$,

$$X_{-1} = -\tfrac{1}{2}\sin\theta S_-, \tag{C.87}$$

$$X_0 = \cos\theta S_z, \tag{C.88}$$

$$X_{+1} = -\tfrac{1}{2}\sin\theta S_+. \tag{C.89}$$

To determine the corresponding eigenfrequencies, we use $[H_{\mathrm{S}}, X_n] = \omega_n X_n$ and find that

$$[H_{\mathrm{S}}, X_{-1}] = \left[-\omega_{\mathrm{L}} S_z, -\tfrac{1}{2}\sin\theta S_-\right] = \omega_{\mathrm{L}} X_{-1}, \tag{C.90}$$

and hence $\omega_{-1} = \omega_{\mathrm{L}}$. It follows that $\omega_{+1} = -\omega_{\mathrm{L}}$, and by inspection, $\omega_0 = 0$.

To evaluate $\tau_{\mathrm{MF}}^{(2)}$ we then have a number of sums to evaluate, and from that

expression we can then calculate the expectation values of S_z and S_x. The calculation of these quantities is made 'easier' by the fact that $\tau_{\rm S}$ is diagonal in the S_z basis, and that $\langle S_y \rangle = 0$. After somewhat lengthy but straightforward calculations we find that

$$\begin{aligned}\langle S_z\rangle^{(2)} = \langle S_z\rangle_0 + \tfrac{1}{4}\hbar\lambda^2 \sin^2\theta \Big[& (S_0(S_0+\hbar) \\ & - \langle S_z^2\rangle_0)\Sigma'(\omega_{\rm L}) - \langle S_z\rangle_0 \hbar\Delta'_\beta(\omega_{\rm L})\Big] \\ & - \beta\lambda^2\Big[\tfrac{1}{4}\sin^2\theta\big(\left(\langle S_z^2\rangle_0 - \langle S_z\rangle_0^2\right)\hbar\Delta_\beta(\omega_{\rm L}) \\ & + \left(\langle S_z^3\rangle_0 - \langle S_z\rangle_0\langle S_z^2\rangle_0\right)\Sigma(\omega_{\rm L})\big) \\ & - \cos^2\theta\left(\langle S_z^3\rangle_0 - \langle S_z\rangle_0\langle S_z^2\rangle_0\right)Q\Big], \end{aligned} \tag{C.91}$$

and

$$\begin{aligned}\langle S_x\rangle^{(2)} = \lambda^2\frac{\sin 2\theta}{4\omega_{\rm L}}\Big[& \left(S_0(S_0+\hbar) - \langle S_z^2\rangle_0\right)\Sigma(\omega_{\rm L}) \\ & - \hbar\langle S_z\rangle_0\Delta_\beta(\omega_{\rm L}) - 4\langle S_z^2\rangle_0 Q\Big], \end{aligned} \tag{C.92}$$

where $\langle \ldots \rangle_0 = {\rm tr}[\tau_{\rm S} \ldots]$.

C.6.3 Quantum to classical limit for weak coupling

In what follows we explicitly verify the quantum to classical transition in the large spin limit presented in C.4, using the quantum and classical weak coupling expressions found in the previous sections.

First, (C.91), we have $\langle S_z\rangle$, regrouped to read

$$\begin{aligned}\langle S_z\rangle = \langle S_z\rangle_0 + \tfrac{1}{4}\lambda^2\sin^2\theta\Big[& (S_0(S_0+\hbar) - \langle S_z^2\rangle_0)\hbar\Sigma' \\ & - \langle S_z\rangle_0\hbar^2\Delta'_\beta - \beta\big(\left(\langle S_z^2\rangle_0 - \langle S_z\rangle_0^2\right)\hbar\Delta_\beta \\ & + \left(\langle S_z^3\rangle_0 - \langle S_z\rangle_0\langle S_z^2\rangle_0\right)(\Sigma - 2Q)\big)\Big] \\ & + \tfrac{1}{4}\beta\lambda^2(1+3\cos 2\theta)Q\left(\langle S_z^3\rangle_0 - \langle S_z\rangle_0\langle S_z^2\rangle_0\right). \end{aligned} \tag{C.93}$$

Introducing the scaled temperature $\beta' = \beta S_0$ and the scaled spin $s_z = S_z/S_0$ and

taking the limit $S_0 \to \infty$ with β' held constant gives

$$\begin{aligned}\langle s_z\rangle = \langle s_z\rangle_0 + \tfrac{1}{4}\lambda^2 \sin^2\theta \Big[& (1-\langle s_z^2\rangle_0)\hbar(S_0\Sigma') \\ & - \langle s_z\rangle_0 \hbar^2 \Delta'_\beta - \beta' \Big(\left(\langle s_z^2\rangle_0 - \langle s_z\rangle_0^2\right) \hbar\Delta_\beta \\ & + \left(\langle s_z^3\rangle_0 - \langle s_z\rangle_0\langle s_z^2\rangle_0\right)\left((S_0\Sigma) - 2S_0Q\right)\Big)\Big] \\ & + \tfrac{1}{4}\beta'\lambda^2(1+3\cos 2\theta)(S_0Q)\left(\langle s_z^3\rangle_0 - \langle s_z\rangle_0\langle s_z^2\rangle_0\right). \end{aligned} \tag{C.94}$$

with (and noting that $S_0 J_\omega$ is independent of S_0)

$$S_0\Sigma \to \int_0^\infty (S_0 J_\omega)\frac{2\omega}{\omega^2-\omega_{\rm L}^2}\mathrm{d}\omega, \tag{C.95}$$

$$\Delta_\beta \to \int_0^\infty \frac{(S_0 J_\omega)}{\hbar}\frac{4\omega_{\rm L}}{\omega^2-\omega_{\rm L}^2}\frac{1}{\beta'\omega}\mathrm{d}\omega, \tag{C.96}$$

$$\Delta'_\beta \to \int_0^\infty \frac{(S_0 J_\omega)}{\hbar^2}\frac{4\left(\omega^2+\omega_{\rm L}^2\right)}{\left(\omega^2-\omega_{\rm L}^2\right)^2}\frac{1}{\beta'\omega}\mathrm{d}\omega, \tag{C.97}$$

$$S_0\Sigma' \to \int_0^\infty \frac{(S_0 J_\omega)}{\hbar}\frac{4\omega_{\rm L}\omega}{\left(\omega^2-\omega_{\rm L}^2\right)^2}\mathrm{d}\omega, \tag{C.98}$$

$$S_0 Q \to \int_0^\infty (S_0 J_\omega)\frac{1}{\omega}\mathrm{d}\omega. \tag{C.99}$$

Making use of the $S_0 \to \infty$ limit of $\langle s_z^n\rangle_0$, $n = 1, 2, 3$ with β' held constant, given from (C.68) by the classical forms (C.55):

$$\langle s_z\rangle_0 = \coth\left(\beta'\omega_{\rm L}\right) - \frac{1}{\beta'\omega_{\rm L}}, \tag{C.100}$$

$$\langle s_z^2\rangle_0 = 1 - \frac{2\coth(\beta'\omega_{\rm L})}{\beta'\omega_{\rm L}} + \frac{2}{(\beta'\omega_{\rm L})^2}, \tag{C.101}$$

$$\begin{aligned}\langle s_z^3\rangle_0 = & \coth\left(\beta'\omega_{\rm L}\right) - \frac{3}{\beta'\omega_{\rm L}} + \frac{6\coth(\beta'\omega_{\rm L})}{(\beta'\omega_{\rm L})^2} \\ & - \frac{6}{(\beta'\omega_{\rm L})^3}, \end{aligned} \tag{C.102}$$

and the above limiting forms for the integrals, we find that the factor multiplying $\sin^2\theta$ vanishes and we are left with

$$\begin{aligned}\langle s_z\rangle = & \langle s_z\rangle_0 \\ & + \frac{1}{4}\beta'\lambda^2 S_0 Q(1+3\cos 2\theta)\left(\langle s_z^3\rangle_0 - \langle s_z\rangle_0\langle s_z^2\rangle_0\right), \end{aligned} \tag{C.103}$$

which on substituting for the $\langle s_z^n\rangle_0$ yields a result formally identical to the fully

classical result, (C.61). In a similar way we can check the large spin limit for $\langle S_x \rangle$, and we regain the classical result, (C.63).

C.7 Ultrastrong coupling limit

In this section the we examine ultrastrong coupling limit of the quantum and classical MF.

C.7.1 Classical ultrastrong coupling limit

The ultrastrong limit is the limit in which the coupling λ is made very large, in principle taken to infinity. To take this limit, first note that the partition function can be written as

$$Z_{\mathsf{S}}^{\mathsf{cl}} = Z_0^{\mathsf{cl}} \int_0^{\pi} \mathrm{d}\theta' \sin\theta' e^{\beta\omega_{\mathrm{L}} S_0 \cos\theta'} \, F(\lambda, \theta, \theta'), \tag{C.104}$$

where

$$F(\lambda, \theta, \theta') = \int_0^{2\pi} d\varphi' e^{\frac{1}{2}\beta\lambda^2 S_0^2 Q\left(\sin\theta \sin\theta' \cos\varphi' - \cos\theta\cos\theta'\right)^2}. \tag{C.105}$$

Defining $a = \frac{1}{2}\beta Q S_0^2$, expanding the exponent and using the periodicity of the trigonometric functions we can rewrite

$$\begin{aligned} F(\lambda, \theta, \theta') = {} & e^{a\lambda^2 \cos^2(\theta'-\theta)} H(\cos\theta'\cos\theta) \\ & \int_0^{2\pi} \mathrm{d}\varphi' e^{-4a\lambda^2 \sin\theta\sin\theta'\cos^2(\varphi'/2)\left(\sin\theta\sin\theta'\sin^2(\varphi'/2)+\cos\theta\cos\theta'\right)} \\ & + e^{a\lambda^2\cos^2(\theta'+\theta)} H(-\cos\theta'\cos\theta) \\ & \int_{-\pi}^{\pi} \mathrm{d}\varphi' e^{-4a\lambda^2 \sin\theta\sin\theta'\sin^2(\varphi'/2)\left(\sin\theta\sin\theta'\cos^2(\varphi'/2)-\cos\theta\cos\theta'\right)} \end{aligned} \tag{C.106}$$

where $H(x)$ is the Heaviside step function. The advantage of this rewriting of $F(\lambda, \theta, \theta')$ is that now the exponents in the integrands are all negative (or zero) over the range of integration. The exponent of the integrand for the first integral where $\cos\theta'\cos\theta > 0$ will vanish at $\varphi' = \pi$, while for the second integral, where $\cos\theta'\cos\theta < 0$, the exponent of the integrand will vanish at $\varphi' = 0, 2\pi$. At these points the integrands will have local maxima which will become increasingly sharp as λ is increased. Similarly, for the second integral the maximum of the second integrand lies at $\varphi' = 0$.

Thus, as λ is increased, we can approximate the exponent in the integral by its behaviour in the neighbourhood of $\varphi' = \pi$ for the first integral, and in the neighbourhood of $\varphi' = 0$ for the second one. This is just using the method of steepest descent. We then obtain

$$Z_{\mathrm{S}}^{\mathrm{cl}} \sim Z_0^{\mathrm{cl}} e^{a\lambda^2} \int_0^{\pi} d\theta' \sin\theta' e^{\beta\omega_{\mathrm{L}} S_0 \cos\theta'} \Big[e^{-a\lambda^2 \sin^2(\theta'-\theta)} R_-(\theta',\theta) H(\cos\theta'\cos\theta) \int_0^{2\pi} \mathrm{d}\varphi' \delta(\varphi'-\pi) + e^{-a\lambda^2 \sin^2(\theta'+\theta)} R_+(\theta',\theta) H(-\cos\theta'\cos\theta) \int_{-\pi}^{\pi} \mathrm{d}\varphi' \delta(\varphi') \Big]. \tag{C.107}$$

where

$$R_{\pm}(\theta',\theta) = \sqrt{\frac{\pi}{a\lambda^2 |\sin\theta' \sin\theta \cos(\theta' \pm \theta)|}}, \tag{C.108}$$

and for later interpretation purposes, the φ' integrals have been retained unevaluated.

Once again we notice that the exponents in the integrands are all negative. The zeroes of the exponents will occur within the range of integration for $\theta' = \theta$ for the first exponents, and for $\theta' = \pi - \theta$ for the second. Therefore, in the large λ limit we have

$$Z_{\mathrm{S}}^{\mathrm{cl}} \to \tilde{Z}_{\mathrm{S,US}}^{\mathrm{cl}} \sim Z_0^{\mathrm{cl}} \frac{\pi e^{a\lambda^2}}{a\lambda^2} \int_0^{\pi} \mathrm{d}\theta' e^{\beta\omega_{\mathrm{L}} S_0 \cos\theta'} \Big[\int_0^{2\pi} \mathrm{d}\varphi' \delta(\theta'-\theta)\delta(\varphi'-\pi) + \int_{-\pi}^{\pi} \mathrm{d}\varphi' \delta(\theta'+\theta-\pi)\delta(\varphi') \Big]. \tag{C.109}$$

This suggests that in the large λ limit, the spin orients itself in either the $\theta' = \theta, \varphi' = \pi$ or $\theta' = \pi - \theta, \varphi' = 0$ directions, though with different weightings for the two directions.

If we return to the interaction on which this result is based, that is

$$\begin{aligned} V &= (S_z \cos\theta - S_x \sin\theta) B \\ &= \mathbf{S} \cdot B(-\sin\theta \mathbf{x} + \cos\theta \mathbf{z}) \\ &= \mathbf{S} \cdot \mathbf{B}, \end{aligned} \tag{C.110}$$

we see that the vector $-\sin\theta\mathbf{x} + \cos\theta\mathbf{z}$ has the polar angles $\theta' = \theta, \varphi' = \pi$. But as

B can be fluctuate between positive or negative values, the vector $\mathbf{B}$ can fluctuate between this and the opposite direction $\theta' = \pi - \theta, \varphi' = 0$. So the effect of the ultrastrong noise is to force the spin to orient itself in either of these two directions.

Returning to the expression for the partition function, we have

$$\begin{aligned}\tilde{Z}^{\rm cl}_{\rm S,US} &\sim Z_0'' \left(e^{\beta\omega_{\rm L} S_0 \cos\theta} + e^{-\beta\omega_{\rm L} S_0 \cos\theta} \right) \\ &\propto \cosh(\beta\omega_{\rm L} S_0 \cos\theta),\end{aligned} \tag{C.111}$$

where extraneous factors have been absorbed into Z_0''. These results are of the same form as found for a quantum spin half. That result is understandable given that the spin half would have two orientations, which mirrors the two orientations that emerge in the strong coupling limit here in the classical case.

C.7.2 Quantum ultrastrong coupling limit

The aim here is to derive an expression for the quantum MFG state of a spin S_0 particle coupled to a thermal reservoir at a temperature β^{-1}, (C.64).

The ultrastrong coupling limit is achieved by making λ very much greater than all other energy parameters of the system, in effect, $\lambda \to \infty$. However, note the absence of the 'counter-term' $-\lambda^2(\cos\theta S_z - \sin\theta S_x)^2 Q$ in the above Hamiltonian. This term appears in [178], where it is found to be cancelled in the strong coupling limit when the trace over the reservoir states is made. Here, that cancellation will not take place, so its presence must be taken into account. It will have no impact in the case of $S_0 = \frac{1}{2}$, as this will be a c-number contribution, but it will have an impact otherwise.

With $H_{\rm S} = -\omega_{\rm L} S_z$ and $P_{s_\theta} = |s_\theta\rangle\langle s_\theta|$ the projector onto the eigenstate $|s_\theta\rangle$ of S_θ where

$$S_\theta = \cos\theta S_z - \sin\theta S_x; \quad S_\theta |s_\theta\rangle = s_\theta |s_\theta\rangle \tag{C.112}$$

we have, in the ultrastrong coupling limit, the unnormalised MFG state of the

particle

$$\tilde{\rho} = \exp\left[-\beta \sum_{s_\theta=-S_0}^{S_0} P_{s_\theta} H_{\rm S} P_{s_\theta}\right] e^{\beta\lambda^2 S_\theta^2 Q}$$
$$= \sum_{s_\theta=-S_0}^{S_0} P_{s_\theta} \exp\left[-\beta\langle s_\theta|H_{\rm S}|s_\theta\rangle\right] e^{\beta\lambda^2\gamma^2 s_\theta^2 Q}. \tag{C.113}$$

Note, as a consequence of the absence of a counter-term, the contribution $\exp\left[\beta\lambda^2 S_\theta^2 Q\right]$ is not cancelled.

Further note the limits on the sum are $\pm S_0$. This follows since $S_\theta = \cos\theta S_z - \sin\theta S_x$ is just S_z rotated around the y axis, i.e.,

$$\cos\theta S_z - \sin\theta S_x = e^{i\theta S_y} S_z e^{-i\theta S_y} = S_\theta \tag{C.114}$$

so the eigenvalue spectrum of S_θ will be the same as that of S_z, i.e., $s_z = -S_0, -S_0+1, \ldots, S_0-1, S_0$. The eigenvectors of S_θ are then, from $S_z|s_z\rangle = s_z|s_z\rangle$

$$S_\theta e^{i\theta S_y}|s_z\rangle = s_z\, e^{i\theta S_y}|s_z\rangle \tag{C.115}$$

i.e., the eigenvectors of S_θ are

$$|s_\theta\rangle = e^{i\theta S_y}|s_z\rangle; \quad s_\theta = s_z = -S_0, \ldots, S_0. \tag{C.116}$$

We then have

$$\langle s_\theta|H_{\rm S}|s_\theta\rangle = \omega_{\rm L}\langle s_z|e^{-i\theta S_y} S_z e^{i\theta S_y}|s_z\rangle$$
$$= \omega_{\rm L}\langle s_z|\cos\theta S_z + \sin\theta S_x|s_z\rangle$$
$$= \omega_{\rm L} s_z \cos\theta, \tag{C.117}$$

from which follows

$$\tilde{\rho} = \sum_{s_z=-S_0}^{S_0} e^{i\theta S_y}|s_z\rangle\langle s_z|e^{-i\theta S_y} e^{\beta\omega_{\rm L} s_z\cos\theta} e^{\beta\lambda^2 Q s_z^2}. \tag{C.118}$$

The partition function is then given by

$$\tilde{Z}_{\mathrm{S}}^{\mathrm{qu}} = \sum_{s_z=-S_0}^{s_z=S_0} e^{\beta\omega_{\mathrm{L}} s_z \cos\theta} e^{\beta\lambda^2 Q s_z^2}. \tag{C.119}$$

This cannot be evaluated exactly, but the limit of large λ is yet to be taken. The dominant contribution to the sum in that limit will be for $s_z = \pm S_0$, so we can write

$$\begin{aligned} \tilde{Z}_{\mathrm{S,US}}^{\mathrm{qu}} e^{-\beta\lambda^2 Q S_0^2} &\sim e^{\beta\omega_{\mathrm{L}} S_0 \cos\theta} + e^{-\beta\omega_{\mathrm{L}} S_0 \cos\theta} \\ &\propto \cosh(\beta\omega_{\mathrm{L}} S_0 \cos\theta). \end{aligned} \tag{C.120}$$

Apart from an unimportant proportionality factor, this is exactly the same results as found for the classical case in the limit of ultrastrong coupling, (C.111).

References

[1] Muamer Kadic, Graeme W. Milton, Martin van Hecke, and Martin Wegener. 3d metamaterials. *Nature Reviews Physics*, 1(3):198–210, jan 2019. doi:10.1038/s42254-018-0018-y.

[2] Giampaolo Pitruzzello and Thomas F Krauss. Photonic crystal resonances for sensing and imaging. *Journal of Optics*, 20(7):073004, jun 2018. doi:10.1088/2040-8986/aac75b.

[3] Sylvain Gigan. Imaging and computing with disorder. *Nature Physics*, 18 (9):980–985, sep 2022. doi:10.1038/s41567-022-01681-1.

[4] Hui Cao. Lasing in random media. *Waves in Random Media*, 13(3):R1–R39, jul 2003. doi:10.1088/0959-7174/13/3/201.

[5] Carl M. Bender and Stefan Boettcher. Real spectra in non-hermitian hamiltonians having pt symmetry. *Physical Review Letters*, 80(24):5243–5246, jun 1998. doi:10.1103/physrevlett.80.5243.

[6] S. A. R. Horsley, M. Artoni, and G. C. La Rocca. Spatial kramers–kronig relations and the reflection of waves. *Nature Photonics*, 9(7):436–439, jun 2015. doi:10.1038/nphoton.2015.106.

[7] K. G. Makris, Z. H. Musslimani, D. N. Christodoulides, and S. Rotter. Constant-intensity waves and their modulation instability in non-hermitian potentials. *Nature Communications*, 6(1), jul 2015. doi:10.1038/ncomms8257.

[8] S A R Horsley, C G King, and T G Philbin. Wave propagation in complex coordinates. *Journal of Optics*, 18(4):044016, apr 2016. doi:10.1088/2040-8978/18/4/044016.

[9] Dimitrios L. Sounas, Romain Fleury, and Andrea Alù. Unidirectional cloaking based on metasurfaces with balanced loss and gain. *Physical Review Applied*, 4(1), jul 2015. doi:10.1103/physrevapplied.4.014005.

[10] Xiaobo Yin and Xiang Zhang. Unidirectional light propagation at exceptional points. *Nature Materials*, 12(3):175–177, feb 2013. doi:10.1038/nmat3576.

[11] Y. D. Chong, Li Ge, Hui Cao, and A. D. Stone. Coherent perfect absorbers: Time-reversed lasers. *Physical Review Letters*, 105(5), jul 2010. doi:10.1103/physrevlett.105.053901.

[12] Denis G. Baranov, Alex Krasnok, Timur Shegai, Andrea Alù, and Yidong Chong. Coherent perfect absorbers: linear control of light with light. *Nature Reviews Materials*, 2(12), oct 2017. doi:10.1038/natrevmats.2017.64.

[13] C.G. King, S.A.R. Horsley, and T.G. Philbin. Perfect transmission through disordered media. *Physical Review Letters*, 118(16), apr 2017. doi:10.1103/physrevlett.118.163201.

[14] Wenchao Hu, Hailong Wang, Perry Ping Shum, and Y. D. Chong. Exceptional points in a non-hermitian topological pump. *Physical Review B*, 95 (18), may 2017. doi:10.1103/physrevb.95.184306.

[15] Liang Feng, Ramy El-Ganainy, and Li Ge. Non-hermitian photonics based on parity–time symmetry. *Nature Photonics*, 11(12):752–762, nov 2017. doi:10.1038/s41566-017-0031-1.

[16] Chengzhi Shi, Marc Dubois, Yun Chen, Lei Cheng, Hamidreza Ramezani, Yuan Wang, and Xiang Zhang. Accessing the exceptional points of parity-time symmetric acoustics. *Nature Communications*, 7(1), mar 2016. doi:10.1038/ncomms11110.

[17] Etienne Rivet, Andre Brandstötter, Konstantinos G. Makris, Hervé Lissek, Stefan Rotter, and Romain Fleury. Constant-pressure sound waves in non-hermitian disordered media. *Nature Physics*, 14(9):942–947, jul 2018. doi:10.1038/s41567-018-0188-7.

[18] Choonlae Cho, Xinhua Wen, Namkyoo Park, and Jensen Li. Digitally virtualized atoms for acoustic metamaterials. *Nature Communications*, 11(1), jan 2020. doi:10.1038/s41467-019-14124-y.

[19] Mohammad-Ali Miri and Andrea Alù. Exceptional points in optics and photonics. *Science*, 363(6422), jan 2019. doi:10.1126/science.aar7709.

[20] Jan Wiersig. Sensors operating at exceptional points: General theory. *Physical Review A*, 93(3), mar 2016. doi:10.1103/physreva.93.033809.

[21] Hossein Hodaei, Absar U. Hassan, Steffen Wittek, Hipolito Garcia-Gracia, Ramy El-Ganainy, Demetrios N. Christodoulides, and Mercedeh Khajavikhan. Enhanced sensitivity at higher-order exceptional points. *Nature*, 548(7666):187–191, aug 2017. doi:10.1038/nature23280.

[22] Raam Uzdin, Alexei Mailybaev, and Nimrod Moiseyev. On the observability and asymmetry of adiabatic state flips generated by exceptional points. *Journal of Physics A: Mathematical and Theoretical*, 44(43):435302, oct 2011. doi:10.1088/1751-8113/44/43/435302.

[23] M V Berry and R Uzdin. Slow non-hermitian cycling: exact solutions and the stokes phenomenon. *Journal of Physics A: Mathematical and Theoretical*, 44(43):435303, oct 2011. doi:10.1088/1751-8113/44/43/435303.

[24] Mohamed Y. Nada, Mohamed A. K. Othman, and Filippo Capolino. Theory of coupled resonator optical waveguides exhibiting high-order exceptional points of degeneracy. *Physical Review B*, 96(18), nov 2017. doi:10.1103/physrevb.96.184304.

[25] Sharareh Sayyad and Flore K. Kunst. Realizing exceptional points of any order in the presence of symmetry. *Physical Review Research*, 4(2), may 2022. doi:10.1103/physrevresearch.4.023130.

[26] Bruce T. Draine and Piotr J. Flatau. Discrete-dipole approximation for scattering calculations. *Journal of the Optical Society of America A*, 11(4):1491, apr 1994. doi:10.1364/josaa.11.001491.

[27] M.A. Yurkin and A.G. Hoekstra. The discrete dipole approximation: An overview and recent developments. *Journal of Quantitative Spectroscopy and Radiative Transfer*, 106(1-3):558–589, jul 2007. doi:10.1016/j.jqsrt.2007.01.034.

[28] Edward M. Purcell and Carlton R. Pennypacker. Scattering and absorption of light by nonspherical dielectric grains. *The Astrophysical Journal*, 186: 705, dec 1973. doi:10.1086/152538.

[29] Nathan Landy and David R. Smith. Two-dimensional metamaterial device design in the discrete dipole approximation. *Journal of Applied Physics*, 116(4):044906, jul 2014. doi:10.1063/1.4891295.

[30] James R. Capers, Stephen J. Boyes, Alastair P. Hibbins, and Simon A. R. Horsley. Designing the collective non-local responses of metasurfaces. *Communications Physics*, 4(1), sep 2021. doi:10.1038/s42005-021-00713-1.

[31] Maryam Baker, Weilin Liu, and Euan McLeod. Accurate and fast modeling of scattering from random arrays of nanoparticles using the discrete dipole approximation and angular spectrum method. *Optics Express*, 29 (14):22761, jul 2021. doi:10.1364/oe.431754.

[32] Evgenij Zubko, Dmitry Petrov, Yevgen Grynko, Yuriy Shkuratov, Hajime Okamoto, Karri Muinonen, Timo Nousiainen, Hiroshi Kimura, Tetsuo Yamamoto, and Gorden Videen. Validity criteria of the discrete dipole approximation. *Applied Optics*, 49(8):1267, mar 2010. doi:10.1364/ao.49.001267.

[33] Mohammad Mahdi Salary, Samad Jafar-Zanjani, and Hossein Mosallaei. Nonreciprocal optical links based on time-modulated nanoantenna arrays: Full-duplex communication. *Physical Review B*, 99(4), jan 2019. doi:10.1103/physrevb.99.045416.

[34] Howard DeVoe. Optical properties of molecular aggregates. i. classical model of electronic absorption and refraction. *The Journal of Chemical Physics*, 41(2):393–400, jul 1964. doi:10.1063/1.1725879.

[35] Leonhard Euler. Solutio problematis ad geometriam situs pertinentis. *Commentarii academiae scientiarum Petropolitanae*, 8(24):128–140, aug 1735.

[36] L. R. Foulds. *Graph Theory Applications*. Springer New York, 1992. doi:10.1007/978-1-4612-0933-1.

[37] C. Coates. Flow-graph solutions of linear algebraic equations. *IRE Transactions on Circuit Theory*, 6(2):170–187, 1959. doi:10.1109/tct.1959.1086537.

[38] Richard A. Brualdi and Dragos Cvetkovic. *A Combinatorial Approach to Matrix Theory and Its Applications*. Chapman and Hall/CRC, aug 2008. doi:10.1201/9781420082241.

[39] Douglas Brent West. *Introduction to graph theory*. Pearson, 2001.

[40] Béla Bollobás. *Graph Theory*. Springer New York, 1979. doi:10.1007/978-1-4612-9967-7.

[41] Werner H. Greub. *Linear Algebra*. Springer Berlin Heidelberg, 1963. doi:10.1007/978-3-662-01545-2.

[42] J. V. Greenman. Graphs and determinants. *The Mathematical Gazette*, 60 (414):241–246, dec 1976. doi:10.2307/3615432.

[43] Roger G. Newton. *Scattering Theory of Waves and Particles*. Springer Berlin Heidelberg, 1982. doi:10.1007/978-3-642-88128-2.

[44] Roger A. Horn and Charles R. Johnson. *Matrix Analysis*. Cambridge University Press, oct 2012. doi:10.1017/cbo9781139020411.

[45] Gilles Demange and Eva-Maria Graefe. Signatures of three coalescing eigenfunctions. *Journal of Physics A: Mathematical and Theoretical*, 45(2): 025303, dec 2011. doi:10.1088/1751-8113/45/2/025303.

[46] Jan Wiersig. Enhancing the sensitivity of frequency and energy splitting detection by using exceptional points: Application to microcavity sensors for single-particle detection. *Physical Review Letters*, 112(20), may 2014. doi:10.1103/physrevlett.112.203901.

[47] Zin Lin, Adi Pick, Marko Lončar, and Alejandro W. Rodriguez. Enhanced spontaneous emission at third-order dirac exceptional points in inverse-designed photonic crystals. *Physical Review Letters*, 117(10), aug 2016. doi:10.1103/physrevlett.117.107402.

[48] C. Dembowski, H.-D. Gräf, H. L. Harney, A. Heine, W. D. Heiss, H. Rehfeld, and A. Richter. Experimental observation of the topological structure of exceptional points. *Physical Review Letters*, 86(5):787–790, jan 2001. doi:10.1103/physrevlett.86.787.

[49] Weijian Chen, Şahin Kaya Özdemir, Guangming Zhao, Jan Wiersig, and Lan Yang. Exceptional points enhance sensing in an optical microcavity. *Nature*, 548(7666):192–196, aug 2017. doi:10.1038/nature23281.

[50] Ayan Banerjee, Rimika Jaiswal, Madhusudan Manjunath, and Awadhesh Narayan. A tropical geometric approach to exceptional points. *Arxiv*, jan 2023. doi:10.48550/arXiv.2301.13485.

[51] Louis Brand. The companion matrix and its properties. *The American Mathematical Monthly*, 71(6):629–634, jun 1964. doi:10.1080/00029890.1964.11992294.

[52] Feng Ding. Transformations between some special matrices. *Computers & Mathematics with Applications*, 59(8):2676–2695, apr 2010. doi:10.1016/j.camwa.2010.01.036.

[53] Richard Bellman. *Introduction to Matrix Analysis, Second Edition*. Society for Industrial and Applied Mathematics, jan 1997. doi:10.1137/1.9781611971170.

[54] Stefano Scali, Janet Anders, and Luis A. Correa. Local master equations bypass the secular approximation. *Quantum*, 5:451, may 2021. doi:10.22331/q-2021-05-01-451.

[55] Ingrid Rotter. The role of exceptional points in quantum systems. *Arxiv*, nov 2010. doi:10.48550/arXiv.1011.0645.

[56] Weiyuan Tang, Xue Jiang, Kun Ding, Yi-Xin Xiao, Zhao-Qing Zhang, C. T. Chan, and Guancong Ma. Exceptional nexus with a hybrid topological invariant. *Science*, 370(6520):1077–1080, nov 2020. doi:10.1126/science.abd8872.

[57] Uwe Günther, Ingrid Rotter, and Boris F Samsonov. Projective hilbert space structures at exceptional points. *Journal of Physics A: Mathematical and Theoretical*, 40(30):8815–8833, jul 2007. doi:10.1088/1751-8113/40/30/014.

[58] Yanyuan Ma and Alan Edelman. Nongeneric eigenvalue perturbations of jordan blocks. *Linear Algebra and its Applications*, 273(1-3):45–63, apr 1998. doi:10.1016/s0024-3795(97)00342-x.

[59] Vadim A. Markel. Extinction, scattering and absorption of electromagnetic waves in the coupled-dipole approximation. *Journal of Quantitative Spectroscopy and Radiative Transfer*, 236:106611, oct 2019. doi:10.1016/j.jqsrt.2019.106611.

[60] William R. Sweeney, Chia Wei Hsu, Stefan Rotter, and A. Douglas Stone. Perfectly absorbing exceptional points and chiral absorbers. *Physical Review Letters*, 122(9), mar 2019. doi:10.1103/physrevlett.122.093901.

[61] Changqing Wang, William R. Sweeney, A. Douglas Stone, and Lan Yang. Coherent perfect absorption at an exceptional point. *Science*, 373(6560): 1261–1265, sep 2021. doi:10.1126/science.abj1028.

[62] Alex Krasnok, Denis Baranov, Huanan Li, Mohammad-Ali Miri, Francesco Monticone, and Andrea Alú. Anomalies in light scattering. *Advances in Optics and Photonics*, 11(4):892, dec 2019. doi:10.1364/aop.11.000892.

[63] Alex Krasnok, Nikita Nefedkin, and Andrea Alu. Parity-time symmetry and exceptional points [electromagnetic perspectives]. *IEEE Antennas and Propagation Magazine*, 63(6):110–121, dec 2021. doi:10.1109/map.2021.3115766.

[64] Hamed Ghaemi-Dizicheh and Henning Schomerus. Compatibility of transport effects in non-hermitian nonreciprocal systems. *Physical Review A*, 104(2), aug 2021. doi:10.1103/physreva.104.023515.

[65] Xiujuan Zhang, Tian Zhang, Ming-Hui Lu, and Yan-Feng Chen. A review on non-hermitian skin effect. *Advances in Physics: X*, 7(1), aug 2022. doi:10.1080/23746149.2022.2109431.

[66] Haoran Xin, Wange Song, Shengjie Wu, Zhiyuan Lin, Shining Zhu, and Tao Li. Manipulating the non-hermitian skin effect in optical ring resonators. *Physical Review B*, 107(16), apr 2023. doi:10.1103/physrevb.107.165401.

[67] Matti Partanen, Jan Goetz, Kuan Yen Tan, Kassius Kohvakka, Vasilii Sevriuk, Russell E Lake, Roope Kokkoniemi, Joni Ikonen, Dibyendu Hazra, Akseli Mäkinen, et al. Exceptional points in tunable superconducting resonators. *Phys. Rev. B*, 100(13):134505, 2019. doi:10.1103/PhysRevB.100.134505.

[68] R Alicki. The quantum open system as a model of the heat engine. *Journal of Physics A: Mathematical and General*, 12(5):L103–L107, may 1979. doi:10.1088/0305-4470/12/5/007.

[69] Herbert Spohn. Entropy production for quantum dynamical semigroups. *J. Math. Phys.*, 19:1227, 1978. doi:10.1063/1.523789.

[70] Ronnie Kosloff. A quantum mechanical open system as a model of a heat engine. *The Journal of chemical physics*, 80(4):1625–1631, 1984. doi:10.1063/1.446862.

[71] Felix Binder, Luis A. Correa, Christian Gogolin, Janet Anders, and Gerardo Adesso, editors. *Thermodynamics in the Quantum Regime*. Springer International Publishing, 2018. doi:10.1007/978-3-319-99046-0.

[72] J. Rossnagel, S. T. Dawkins, K. N. Tolazzi, O. Abah, E. Lutz, F. Schmidt-Kaler, and K. Singer. A single-atom heat engine. *Science*, 352(6283): 325–329, apr 2016. doi:10.1126/science.aad6320.

[73] David Von Lindenfels, Oliver Gräb, Christian T Schmiegelow, Vidyut Kaushal, Jonas Schulz, Mark T Mitchison, John Goold, Ferdinand Schmidt-Kaler, and Ulrich G Poschinger. Spin heat engine coupled to a harmonic-oscillator flywheel. *Physical review letters*, 123(8):080602, 2019. doi:10.1103/physrevlett.123.080602.

[74] James Klatzow, Jonas N Becker, Patrick M Ledingham, Christian Weinzetl, Krzysztof T Kaczmarek, Dylan J Saunders, Joshua Nunn, Ian A Walmsley, Raam Uzdin, and Eilon Poem. Experimental demonstration of quantum effects in the operation of microscopic heat engines. *Physical Review Letters*, 122(11):110601, 2019. doi:10.1103/physrevlett.122.110601.

[75] D Gelbwaser-Klimovsky, Krzysztof Szczygielski, U Vogl, A Saß, Robert Alicki, G Kurizki, and M Weitz. Laser-induced cooling of broadband heat reservoirs. *Physical Review A*, 91(2):023431, 2015. doi:10.1103/physreva.91.023431.

[76] Yueyang Zou, Yue Jiang, Yefeng Mei, Xianxin Guo, and Shengwang Du. Quantum heat engine using electromagnetically induced transparency. *Physical Review Letters*, 119(5), aug 2017. doi:10.1103/physrevlett.119.050602.

[77] Jonne V Koski, Ville F Maisi, Jukka P Pekola, and Dmitri V Averin. Experimental realization of a szilard engine with a single electron. *Proceedings of the National Academy of Sciences*, 111(38):13786–13789, 2014. doi:10.1073/pnas.1406966111.

[78] Y. Masuyama, K. Funo, Y. Murashita, A. Noguchi, S. Kono, Y. Tabuchi, R. Yamazaki, M. Ueda, and Y. Nakamura. Information-to-work conversion by maxwell's demon in a superconducting circuit quantum electrodynamical system. *Nature Communications*, 9(1), mar 2018. doi:10.1038/s41467-018-03686-y.

[79] M Naghiloo, JJ Alonso, A Romito, E Lutz, and KW Murch. Information gain and loss for a quantum maxwell's demon. *Physical review letters*, 121(3): 030604, 2018. doi:10.1103/physrevlett.121.030604.

[80] Nathanaël Cottet, Sébastien Jezouin, Landry Bretheau, Philippe Campagne-Ibarcq, Quentin Ficheux, Janet Anders, Alexia Auffèves, Rémi Azouit, Pierre Rouchon, and Benjamin Huard. Observing a quantum maxwell demon at work. *Proceedings of the National Academy of Sciences*, 114(29):7561–7564, jul 2017. doi:10.1073/pnas.1704827114.

[81] Vittorio Gorini. Completely positive dynamical semigroups of n-level systems. *Journal of Mathematical Physics*, 17(5):821, 1976. doi:10.1063/1.522979.

[82] G. Lindblad. On the generators of quantum dynamical semigroups. *Communications in Mathematical Physics*, 48(2):119–130, jun 1976. doi:10.1007/bf01608499.

[83] Robert Alicki and Ronnie Kosloff. Introduction to quantum thermodynamics: History and prospects. In *Fundamental Theories of Physics*, pages 1–33. Springer International Publishing, 2018. doi:10.1007/978-3-319-99046-0_1.

[84] Ronnie Kosloff. Quantum thermodynamics: A dynamical viewpoint. *Entropy*, 15(12):2100–2128, may 2013. doi:10.3390/e15062100.

[85] Ronnie Kosloff and Amikam Levy. Quantum heat engines and refrigerators: Continuous devices. *Annual Review of Physical Chemistry*, 65(1):365–393, apr 2014. doi:10.1146/annurev-physchem-040513-103724.

[86] Herbert Spohn. An algebraic condition for the approach to equilibrium of an open n-level system. *Lett. Maths. Phys.*, 2(1):33–38, 1977. doi:10.1007/BF00420668.

[87] Heinz-Peter Breuer and Francesco Petruccione. *The Theory of Open Quantum Systems*. Oxford University Press, jan 2007. doi:10.1093/acprof:oso/9780199213900.001.0001.

[88] J Onam González, Luis A Correa, Giorgio Nocerino, José P Palao, Daniel Alonso, and Gerardo Adesso. Testing the validity of the 'local'and 'global'gkls master equations on an exactly solvable model. *Open Syst. Inf. Dyn.*, 24(04):1740010, 2017. doi:10.1142/S1230161217400108.

[89] Patrick P Hofer, Martí Perarnau-Llobet, L David M Miranda, Géraldine Haack, Ralph Silva, Jonatan Bohr Brask, and Nicolas Brunner. Markovian master equations for quantum thermal machines: local versus global approach. *New J. Phys.*, 19(12):123037, 2017. doi:10.1088/1367-2630/aa964f.

[90] Hannu Wichterich, Markus J. Henrich, Heinz-Peter Breuer, Jochen Gemmer, and Mathias Michel. Modeling heat transport through completely positive maps. *Physical Review E*, 76(3), sep 2007. doi:10.1103/physreve.76.031115.

[91] Ángel Rivas, A Douglas K Plato, Susana F Huelga, and Martin B Plenio. Markovian master equations: a critical study. *New Journal of Physics*, 12 (11):113032, nov 2010. doi:10.1088/1367-2630/12/11/113032.

[92] Luis A Correa, José P Palao, Gerardo Adesso, and Daniel Alonso. Performance bound for quantum absorption refrigerators. *Phys. Rev. E*, 87(4): 042131, 2013. doi:10.1103/PhysRevE.87.042131.

[93] Amikam Levy and Ronnie Kosloff. The local approach to quantum transport may violate the second law of thermodynamics. *EPL (Europhysics Letters)*, 107(2):20004, jul 2014. doi:10.1209/0295-5075/107/20004.

[94] Pedro D. Manrique, Ferney Rodríguez, Luis Quiroga, and Neil F. Johnson. Nonequilibrium quantum systems: Divergence between global and local descriptions. *Advances in Condensed Matter Physics*, 2015:1–7, 2015. doi:10.1155/2015/615727.

[95] Jürgen T. Stockburger and Thomas Motz. Thermodynamic deficiencies of some simple lindblad operators. *Fortschritte der Physik*, 65(6-8):1600067, nov 2016. doi:10.1002/prop.201600067.

[96] Jader P. Santos and Gabriel T. Landi. Microscopic theory of a nonequilibrium open bosonic chain. *Phys. Rev. E*, 94:062143, Dec 2016. doi:10.1103/PhysRevE.94.062143.

[97] Mark T Mitchison and Martin B Plenio. Non-additive dissipation in open quantum networks out of equilibrium. *New Journal of Physics*, 20(3): 033005, mar 2018. doi:10.1088/1367-2630/aa9f70.

[98] Jan Kołodyński, Jonatan Bohr Brask, Martí Perarnau-Llobet, and Bogna Bylicka. Adding dynamical generators in quantum master equations. *Phys. Rev. A*, 97:062124, Jun 2018. doi:10.1103/PhysRevA.97.062124.

[99] M. Tahir Naseem, André Xuereb, and Özgür E. Müstecaplıoğlu. Thermodynamic consistency of the optomechanical master equation. *Physical Review A*, 98(5), nov 2018. doi:10.1103/physreva.98.052123.

[100] Marco Cattaneo, Gian Luca Giorgi, Sabrina Maniscalco, and Roberta Zambrini. Local versus global master equation with common and separate baths: superiority of the global approach in partial secular approximation. *New Journal of Physics*, 21(11):113045, nov 2019. doi:10.1088/1367-2630/ab54ac.

[101] Conor McConnell and Ahsan Nazir. Electron counting statistics for non-additive environments. *The Journal of Chemical Physics*, 151(5):054104, aug 2019. doi:10.1063/1.5095838.

[102] Adam Hewgill, Gabriele De Chiara, and Alberto Imparato. Quantum thermodynamically consistent local master equations. *Physical Review Research*, 3(1), feb 2021. doi:10.1103/physrevresearch.3.013165.

[103] Luis A. Correa, José P. Palao, and Daniel Alonso. Internal dissipation and heat leaks in quantum thermodynamic cycles. *Physical Review E*, 92(3), sep 2015. doi:10.1103/physreve.92.032136.

[104] Gernot Schaller and Tobias Brandes. Preservation of positivity by dynamical coarse graining. *Phys. Rev. A*, 78:022106, Aug 2008. doi:10.1103/PhysRevA.78.022106.

[105] JD Cresser and C Facer. Coarse-graining in the derivation of markovian master equations and its significance in quantum thermodynamics. *arXiv preprint arXiv:1710.09939*, 2017. URL https://arxiv.org/abs/1710.09939.

[106] Stella Seah, Stefan Nimmrichter, and Valerio Scarani. Refrigeration beyond weak internal coupling. *Phys. Rev. E*, 98:012131, Jul 2018. doi:10.1103/PhysRevE.98.012131.

[107] Donato Farina and Vittorio Giovannetti. Open-quantum-system dynamics: Recovering positivity of the redfield equation via the partial secular approximation. *Phys. Rev. A*, 100:012107, Jul 2019. doi:10.1103/PhysRevA.100.012107.

[108] D. Farina, G. De Filippis, V. Cataudella, M. Polini, and V. Giovannetti. Going beyond local and global approaches for localized thermal dissipation. *Physical Review A*, 102(5), nov 2020. doi:10.1103/physreva.102.052208.

[109] Christian Majenz, Tameem Albash, Heinz-Peter Breuer, and Daniel A. Lidar. Coarse graining can beat the rotating-wave approximation in quantum markovian master equations. *Physical Review A*, 88(1), jul 2013. doi:10.1103/physreva.88.012103.

[110] Daniel A. Lidar, Zsolt Bihary, and K.Birgitta Whaley. From completely positive maps to the quantum markovian semigroup master equation. *Chemical Physics*, 268(1-3):35–53, jun 2001. doi:10.1016/s0301-0104(01)00330-5.

[111] Evgeny Mozgunov and Daniel Lidar. Completely positive master equation for arbitrary driving and small level spacing. *Quantum*, 4:227, feb 2020. doi:10.22331/q-2020-02-06-227.

[112] Cyril Elouard, David Herrera-Martí, Massimiliano Esposito, and Alexia Auffèves. Thermodynamics of optical bloch equations. *New Journal of Physics*, 22(10):103039, oct 2020. doi:10.1088/1367-2630/abbd6e.

[113] A. S. Trushechkin and I. V. Volovich. Perturbative treatment of inter-site couplings in the local description of open quantum networks. *EPL (Europhysics Letters)*, 113(3):30005, feb 2016. doi:10.1209/0295-5075/113/30005.

[114] Archak Purkayastha, Abhishek Dhar, and Manas Kulkarni. Out-of-equilibrium open quantum systems: A comparison of approximate quantum master equation approaches with exact results. *Physical Review A*, 93(6), jun 2016. doi:10.1103/physreva.93.062114.

[115] Luis A. Correa, Antonio A. Valido, and Daniel Alonso. Asymptotic discord and entanglement of nonresonant harmonic oscillators under weak and strong dissipation. *Phys. Rev. A*, 86:012110, Jul 2012. doi:10.1103/PhysRevA.86.012110.

[116] Luis A. Correa, Jose P. Palao, Daniel Alonso, and Gerardo Adesso. Quantum-enhanced absorption refrigerators. *Sci. Rep.*, 4:3949, Feb 2014. doi:10.1038/srep03949.

[117] Tosio Kato. *Perturbation Theory for Linear Operators*. Springer Berlin Heidelberg, 1995. doi:10.1007/978-3-642-66282-9.

[118] A. G. Redfield. On the theory of relaxation processes. *IBM Journal of Research and Development*, 1(1):19–31, jan 1957. doi:10.1147/rd.11.0019.

[119] Philipp Strasberg, Gernot Schaller, Thomas L. Schmidt, and Massimiliano Esposito. Fermionic reaction coordinates and their application to an autonomous maxwell demon in the strong-coupling regime. *Phys. Rev. B*, 97: 205405, May 2018. doi:10.1103/PhysRevB.97.205405.

[120] Max Planck. *Treatise on Thermodynamics*, volume 69. Springer Science and Business Media LLC, dec 1903. doi:10.1038/069194a0.

[121] Gabriele De Chiara, Gabriel Landi, Adam Hewgill, Brendan Reid, Alessandro Ferraro, Augusto J Roncaglia, and Mauro Antezza. Reconciliation of quantum local master equations with thermodynamics. *New Journal of Physics*, 20(11):113024, nov 2018. doi:10.1088/1367-2630/aaecee.

[122] Valerio Scarani, Mário Ziman, Peter Štelmachovič, Nicolas Gisin, and Vladimír Bužek. Thermalizing quantum machines: Dissipation and entanglement. *Phys. Rev. Lett.*, 88:097905, Feb 2002. doi:10.1103/PhysRevLett.88.097905.

[123] Felipe Barra. The thermodynamic cost of driving quantum systems by their boundaries. *Scientific Reports*, 5(1), oct 2015. doi:10.1038/srep14873.

[124] F. Barra and C. Lledó. The smallest absorption refrigerator: the thermodynamics of a system with quantum local detailed balance. *Eur. Phys. J. Spec. Top.*, 227:231, 2018. doi:10.1140/epjst/e2018-00084-x.

[125] Fabio Benatti, Roberto Floreanini, and Laleh Memarzadeh. Bath assisted transport in a three-site spin chain: global vs. local approach. *arXiv preprint arXiv:2004.10433*, 2020. doi:10.1103/physreva.102.042219.

[126] Chris Fleming, N I Cummings, Charis Anastopoulos, and B L Hu. The rotating-wave approximation: consistency and applicability from an open quantum system analysis. *Journal of Physics A: Mathematical and Theoretical*, 43(40):405304, sep 2010. doi:10.1088/1751-8113/43/40/405304.

[127] Jan Wiersig. Enhancing the sensitivity of frequency and energy splitting detection by using exceptional points: Application to microcavity sensors for single-particle detection. *Physical Review Letters*, 112(20), may 2014. doi:10.1103/physrevlett.112.203901.

[128] Weijian Chen, Şahin Kaya Özdemir, Guangming Zhao, Jan Wiersig, and Lan Yang. Exceptional points enhance sensing in an optical microcavity. *Nature*, 548(7666):192–196, aug 2017. doi:10.1038/nature23281.

[129] H. Hodaei, M.-A. Miri, M. Heinrich, D. N. Christodoulides, and M. Khajavikhan. Parity-time-symmetric microring lasers. *Science*, 346(6212):975–978, oct 2014. doi:10.1126/science.1258480.

[130] Jörg Doppler, Alexei A. Mailybaev, Julian Böhm, Ulrich Kuhl, Adrian Girschik, Florian Libisch, Thomas J. Milburn, Peter Rabl, Nimrod Moiseyev, and Stefan Rotter. Dynamically encircling an exceptional point for asymmetric mode switching. *Nature*, 537(7618):76–79, jul 2016. doi:10.1038/nature18605.

[131] H. Xu, D. Mason, Luyao Jiang, and J. G. E. Harris. Topological energy transfer in an optomechanical system with exceptional points. *Nature*, 537 (7618):80–83, jul 2016. doi:10.1038/nature18604.

[132] Mengzhen Zhang, William Sweeney, Chia Wei Hsu, Lan Yang, A. D. Stone, and Liang Jiang. Quantum noise theory of exceptional point amplifying sensors. *Physical Review Letters*, 123(18), oct 2019. doi:10.1103/physrevlett.123.180501.

[133] J. Okołowicz, M. Płoszajczak, and I. Rotter. Dynamics of quantum systems embedded in a continuum. *Physics Reports*, 374(4-5):271–383, feb 2003. doi:10.1016/s0370-1573(02)00366-6.

[134] Nimrod Moiseyev. *Non-Hermitian Quantum Mechanics*. Cambridge University Press, 2011. doi:10.1017/cbo9780511976186.

[135] Andrea Insinga, Bjarne Andresen, Peter Salamon, and Ronnie Kosloff. Quantum heat engines: Limit cycles and exceptional points. *Physical Review E*, 97(6), jun 2018. doi:10.1103/physreve.97.062153.

[136] Morag Am-Shallem, Ronnie Kosloff, and Nimrod Moiseyev. Exceptional points for parameter estimation in open quantum systems: analysis of the bloch equations. *New Journal of Physics*, 17(11):113036, nov 2015. doi:10.1088/1367-2630/17/11/113036.

[137] Fabrizio Minganti, Adam Miranowicz, Ravindra W. Chhajlany, and Franco Nori. Quantum exceptional points of non-hermitian hamiltonians and liouvillians: The effects of quantum jumps. *Physical Review A*, 100(6), dec 2019. doi:10.1103/physreva.100.062131.

[138] Alberto Suárez, Robert Silbey, and Irwin Oppenheim. Memory effects in the relaxation of quantum open systems. *J. Chem. Phys.*, 97(7):5101–5107, 1992. doi:10.1063/1.463831.

[139] Pierre Gaspard and Masataka Nagaoka. Slippage of initial conditions for the Redfield master equation. *J. Chem. Phys.*, 111(13):5668–5675, 1999. doi:10.1063/1.479867.

[140] Jan Jeske, David J. Ing, Martin B. Plenio, Susana F. Huelga, and Jared H. Cole. Bloch-redfield equations for modeling light-harvesting complexes. *The Journal of Chemical Physics*, 142(6):064104, feb 2015. doi:10.1063/1.4907370.

[141] Philipp Strasberg, Gernot Schaller, Neill Lambert, and Tobias Brandes. Nonequilibrium thermodynamics in the strong coupling and non-markovian regime based on a reaction coordinate mapping. *New J. Phys.*, 18(7): 073007, 2016. doi:10.1088/1367-2630/18/7/073007.

[142] Richard Hartmann and Walter T. Strunz. Accuracy assessment of perturbative master equations: Embracing nonpositivity. *Phys. Rev. A*, 101:012103, Jan 2020. doi:10.1103/PhysRevA.101.012103.

[143] Marek Winczewski and Robert Alicki. Renormalization in the theory of open quantum systems via the self-consistency condition. *arXiv*, 2023. doi:10.48550/arXiv.2112.11962.

[144] Luis A. Correa and Jonas Glatthard. Potential renormalisation, lamb shift and mean-force gibbs state – to shift or not to shift? *arXiv*, 2023. doi:10.48550/arXiv.2305.08941.

[145] J Anders, C R J Sait, and S A R Horsley. Quantum brownian motion for magnets. *New Journal of Physics*, 24(3):033020, mar 2022. doi:10.1088/1367-2630/ac4ef2.

[146] N. Bohr. Über die serienspektra der elemente. *Zeitschrift für Physik*, 2: 423–469, Oct 1920. doi:10.1007/BF01329978.

[147] Kenneth Millard and Harvey S. Leff. Infinite-spin limit of the quantum heisenberg model. *Journal of Mathematical Physics*, 12(6):1000–1005, 1971. doi:10.1063/1.1665664.

[148] Elliott H. Lieb. The classical limit of quantum spin systems. *Communications in Mathematical Physics*, 31(4):327–340, 1973. doi:10.1007/BF01646493.

[149] Richard L Liboff. Bohr correspondence principle for large quantum numbers. *Foundations of Physics*, 5(2):271–293, 1975.

[150] Richard L. Liboff. The correspondence principle revisited. *Physics Today*, 37(2):50–55, 1984.

[151] Maksym Kryvohuz and Jianshu Cao. Quantum-classical correspondence in response theory. *Phys. Rev. Lett.*, 95:180405, Oct 2005. doi:10.1103/PhysRevLett.95.180405.

[152] Eva-Maria Graefe, Hans Jürgen Korsch, and Astrid Elisa Niederle. Quantum-classical correspondence for a non-hermitian bose-hubbard dimer. *Phys. Rev. A*, 82:013629, Jul 2010. doi:10.1103/PhysRevA.82.013629.

[153] Christopher Jarzynski, H. T. Quan, and Saar Rahav. Quantum-classical correspondence principle for work distributions. *Phys. Rev. X*, 5:031038, Sep 2015. doi:10.1103/PhysRevX.5.031038.

[154] Jin-Fu Chen, Tian Qiu, and Hai-Tao Quan. Quantum–classical correspondence principle for heat distribution in quantum brownian motion. *Entropy*, 23(12), 2021. ISSN 1099-4300. doi:10.3390/e23121602.

[155] R F L Evans, W J Fan, P Chureemart, T A Ostler, M O A Ellis, and R W Chantrell. Atomistic spin model simulations of magnetic nanomaterials. *Journal of Physics: Condensed Matter*, 26(10):103202, feb 2014. doi:10.1088/0953-8984/26/10/103202.

[156] R F L Evans, W J Fan, P Chureemart, T A Ostler, M O A Ellis, and R W Chantrell. Atomistic spin model simulations of magnetic nanomaterials. *Journal of Physics: Condensed Matter*, 26(10):103202, feb 2014. doi:10.1088/0953-8984/26/10/103202.

[157] Joseph Barker and Gerrit E. W. Bauer. Semiquantum thermodynamics of complex ferrimagnets. *Phys. Rev. B*, 100:140401, Oct 2019. doi:10.1103/PhysRevB.100.140401.

[158] Mara Strungaru, Matthew O. A. Ellis, Sergiu Ruta, Oksana Chubykalo-Fesenko, Richard F. L. Evans, and Roy W. Chantrell. Spin-lattice dynamics model with angular momentum transfer for canonical and microcanonical ensembles. *Phys. Rev. B*, 103:024429, Jan 2021. doi:10.1103/PhysRevB.103.024429.

[159] Joseph Barker and Unai Atxitia. A review of modelling in ferrimagnetic spintronics. *Journal of the Physical Society of Japan*, 90(8):081001, 2021. doi:10.7566/JPSJ.90.081001.

[160] Patrick Vorndamme, Heinz-Jürgen Schmidt, Christian Schröder, and Jürgen Schnack. Observation of phase synchronization and alignment during free induction decay of quantum spins with heisenberg interactions. *New Journal of Physics*, 23(8):083038, aug 2021. doi:10.1088/1367-2630/ac18df.

[161] Chris Jarzynski. Nonequilibrium work theorem for a system strongly coupled to a thermal environment. *Journal of Statistical Mechanics: Theory and Experiment*, 2004(09):P09005, sep 2004. doi:10.1088/1742-5468/2004/09/p09005.

[162] Udo Seifert. First and second law of thermodynamics at strong coupling. *Phys. Rev. Lett.*, 116:020601, Jan 2016. doi:10.1103/PhysRevLett.116.020601.

[163] Christopher Jarzynski. Stochastic and macroscopic thermodynamics of strongly coupled systems. *Phys. Rev. X*, 7:011008, Jan 2017. doi:10.1103/PhysRevX.7.011008.

[164] Philipp Strasberg and Massimiliano Esposito. Stochastic thermodynamics in the strong coupling regime: An unambiguous approach based on coarse graining. *Phys. Rev. E*, 95:062101, Jun 2017. doi:10.1103/PhysRevE.95.062101.

[165] H. J. D. Miller and J. Anders. Entropy production and time asymmetry in the presence of strong interactions. *Phys. Rev. E*, 95:062123, Jun 2017. doi:10.1103/PhysRevE.95.062123.

[166] Erik Aurell. Unified picture of strong-coupling stochastic thermodynamics and time reversals. *Phys. Rev. E*, 97:042112, Apr 2018. doi:10.1103/PhysRevE.97.042112.

[167] Takashi Mori and Seiji Miyashita. Dynamics of the density matrix in contact with a thermal bath and the quantum master equation. *Journal of the Physical Society of Japan*, 77(12):124005, dec 2008. doi:10.1143/jpsj.77.124005.

[168] Michele Campisi, Peter Talkner, and Peter Hänggi. Thermodynamics and fluctuation theorems for a strongly coupled open quantum system: an exactly solvable case. *Journal of Physics A: Mathematical and Theoretical*, 42(39):392002, sep 2009. doi:10.1088/1751-8113/42/39/392002.

[169] Stefanie Hilt, Saroosh Shabbir, Janet Anders, and Eric Lutz. Landauer's principle in the quantum regime. *Phys. Rev. E*, 83:030102, Mar 2011. doi:10.1103/PhysRevE.83.030102.

[170] C. H. Fleming and N. I. Cummings. Accuracy of perturbative master equations. *Phys. Rev. E*, 83:031117, Mar 2011. doi:10.1103/PhysRevE.83.031117.

[171] Juzar Thingna, Jian-Sheng Wang, and Peter Hänggi. Generalized gibbs state with modified redfield solution: Exact agreement up to second order. *The Journal of Chemical Physics*, 136(19):194110, 2012. doi:10.1063/1.4718706.

[172] Y. Subaş ı, C. H. Fleming, J. M. Taylor, and B. L. Hu. Equilibrium states of open quantum systems in the strong coupling regime. *Phys. Rev. E*, 86: 061132, Dec 2012. doi:10.1103/PhysRevE.86.061132.

[173] T G Philbin and J Anders. Thermal energies of classical and quantum damped oscillators coupled to reservoirs. *Journal of Physics A: Mathematical and Theoretical*, 49(21):215303, apr 2016. doi:10.1088/1751-8113/49/21/215303.

[174] H. J. D. Miller and J. Anders. Energy-temperature uncertainty relation in quantum thermodynamics. *Nature Communications*, 9(1), jun 2018. doi:10.1038/s41467-018-04536-7.

[175] Philipp Strasberg. Repeated interactions and quantum stochastic thermodynamics at strong coupling. *Phys. Rev. Lett.*, 123:180604, Oct 2019. doi:10.1103/PhysRevLett.123.180604.

[176] Anton Trushechkin. Quantum master equations and steady states for the ultrastrong-coupling limit and the strong-decoherence limit. *arXiv preprint arXiv:2109.01888*, 2021.

[177] A. S. Trushechkin, M. Merkli, J. D. Cresser, and J. Anders. Open quantum system dynamics and the mean force gibbs state. *AVS Quantum Science*, 4(1):012301, 2022. doi:10.1116/5.0073853.

[178] J. D. Cresser and J. Anders. Weak and ultrastrong coupling limits of the quantum mean force gibbs state. *Phys. Rev. Lett.*, 127:250601, Dec 2021. doi:10.1103/PhysRevLett.127.250601.

[179] Archak Purkayastha, Giacomo Guarnieri, Mark T. Mitchison, Radim Filip, and John Goold. Tunable phonon-induced steady-state coherence in a double-quantum-dot charge qubit. *npj Quantum Information*, 6(1), mar 2020. doi:10.1038/s41534-020-0256-6.

[180] L. Ferialdi. Exact non-markovian master equation for the spin-boson and jaynes-cummings models. *Phys. Rev. A*, 95:020101, Feb 2017. doi:10.1103/PhysRevA.95.020101.

[181] Yiu-Fung Chiu, Aidan Strathearn, and Jonathan Keeling. Numerical evaluation and robustness of the quantum mean force gibbs state. *arXiv preprint arXiv:2112.08254*, 2021.

[182] Anton Trushechkin. Calculation of coherences in förster and modified redfield theories of excitation energy transfer. *The Journal of Chemical Physics*, 151(7):074101, 2019. doi:10.1063/1.5100967.

[183] Mino Yang and Graham R. Fleming. Influence of phonons on exciton transfer dynamics: comparison of the redfield, förster, and modified redfield equations. *Chemical Physics*, 282(1):163–180, 2002. ISSN 0301-0104. doi:https://doi.org/10.1016/S0301-0104(02)00604-3.

[184] Avinash Kolli, Edward J. O'Reilly, Gregory D. Scholes, and Alexandra Olaya-Castro. The fundamental role of quantized vibrations in coherent light harvesting by cryptophyte algae. *The Journal of Chemical Physics*, 137(17):174109, 2012. doi:10.1063/1.4764100.

[185] Jeremy M. Moix, Yang Zhao, and Jianshu Cao. Equilibrium-reduced density matrix formulation: Influence of noise, disorder, and temperature on localization in excitonic systems. *Phys. Rev. B*, 85:115412, Mar 2012. doi:10.1103/PhysRevB.85.115412.

[186] S.F. Huelga and M.B. Plenio. Vibrations, quanta and biology. *Contemporary Physics*, 54(4):181–207, 2013. doi:10.1080/00405000.2013.829687.

[187] Joachim Seibt and Tomáš Mančal. Ultrafast energy transfer with competing channels: Non-equilibrium förster and modified redfield theories. *The Journal of Chemical Physics*, 146(17):174109, 2017. doi:10.1063/1.4981523.

[188] Andrius Gelzinis and Leonas Valkunas. Analytical derivation of equilibrium state for open quantum system. *The Journal of Chemical Physics*, 152(5): 051103, 2020. doi:10.1063/1.5141519.

[189] Vivek Unikandanunni, Rajasekhar Medapalli, Marco Asa, Edoardo Albisetti, Daniela Petti, Riccardo Bertacco, Eric E. Fullerton, and Stefano Bonetti. Inertial spin dynamics in epitaxial cobalt films. *Phys. Rev. Lett.*, 129:237201, Nov 2022. doi:10.1103/PhysRevLett.129.237201.

[190] Kumar Neeraj, Nilesh Awari, Sergey Kovalev, Debanjan Polley, Nanna Zhou Hagström, Sri Sai Phani Kanth Arekapudi, Anna Semisalova, Kilian Lenz, Bertram Green, Jan-Christoph Deinert, Igor Ilyakov, Min Chen, Mohammed Bawatna, Valentino Scalera, Massimiliano d'Aquino, Claudio Serpico, Olav Hellwig, Jean-Eric Wegrowe, Michael Gensch, and Stefano Bonetti. Inertial spin dynamics in ferromagnets. *Nature Physics*, 17(2):245–250, sep 2020. doi:10.1038/s41567-020-01040-y.

[191] Kumar Neeraj, Matteo Pancaldi, Valentino Scalera, Salvatore Perna, Massimiliano d'Aquino, Claudio Serpico, and Stefano Bonetti. Magnetization switching in the inertial regime. *Phys. Rev. B*, 105:054415, Feb 2022. doi:10.1103/PhysRevB.105.054415.

[192] A Stupakiewicz, CS Davies, K Szerenos, D Afanasiev, KS Rabinovich, AV Boris, Andrea Caviglia, AV Kimel, and A Kirilyuk. Ultrafast phononic switching of magnetization. *Nature Physics*, 17(4):489–492, 2021.

[193] Ahsan Nazir. Correlation-dependent coherent to incoherent transitions in resonant energy transfer dynamics. *Phys. Rev. Lett.*, 103:146404, Oct 2009. doi:10.1103/PhysRevLett.103.146404.

[194] A. Recati, P. O. Fedichev, W. Zwerger, J. von Delft, and P. Zoller. Atomic quantum dots coupled to a reservoir of a superfluid bose-einstein condensate. *Phys. Rev. Lett.*, 94:040404, Feb 2005. doi:10.1103/PhysRevLett.94.040404.

[195] L. Magazzù, P. Forn-Díaz, R. Belyansky, J.-L. Orgiazzi, M. A. Yurtalan, M. R. Otto, A. Lupascu, C. M. Wilson, and M. Grifoni. Probing the strongly driven spin-boson model in a superconducting quantum circuit. *Nature Communications*, 9(1403), 2018. doi:10.1038/s41467-018-03626-w.

[196] Maria Popovic, Mark T. Mitchison, Aidan Strathearn, Brendon W. Lovett, John Goold, and Paul R. Eastham. Quantum heat statistics with time-evolving matrix product operators. *PRX Quantum*, 2:020338, Jun 2021. doi:10.1103/PRXQuantum.2.020338.

[197] Heinz-Peter Breuer and Francesco Petruccione. *The Theory of Open Quantum Systems*. Oxford University Press, jan 2007. doi:10.1093/acprof:oso/9780199213900.001.0001.

[198] Bruno Huttner and Stephen M. Barnett. Quantization of the electromagnetic field in dielectrics. *Phys. Rev. A*, 46:4306–4322, Oct 1992. doi:10.1103/PhysRevA.46.4306.

[199] Amir Fruchtman, Neill Lambert, and Erik M. Gauger. When do perturbative approaches accurately capture the dynamics of complex quantum systems? *Scientific Reports*, 6(1):2045–2322, jun 2016. doi:10.1038/srep28204.

[200] Jianlan Wu, Fan Liu, Young Shen, Jianshu Cao, and Robert J Silbey. Efficient energy transfer in light-harvesting systems, i: optimal temperature, reorganization energy and spatial–temporal correlations. *New Journal of Physics*, 12(10):105012, oct 2010. doi:10.1088/1367-2630/12/10/105012.

[201] Gerhard Ritschel, Jan Roden, Walter T Strunz, and Alexander Eisfeld. An efficient method to calculate excitation energy transfer in light-harvesting systems: application to the fenna–matthews–olson complex. *New Journal of Physics*, 13(11):113034, nov 2011. doi:10.1088/1367-2630/13/11/113034.

[202] Camille L Latune. Steady state in ultrastrong coupling regime: perturbative expansion and first orders. *arXiv preprint arXiv:2110.02186*, 2021.

[203] Nicholas Anto-Sztrikacs, Ahsan Nazir, and Dvira Segal. Effective hamiltonian theory of open quantum systems at strong coupling. *arXiv preprint*, 2022. doi:10.48550/ARXIV.2211.05701.

[204] Vojkan Jakšić and Claude-Alain Pillet. On a model for quantum friction iii. ergodic properties of the spin-boson system. *Communications in Mathematical Physics*, 178(3):627–651, Jul 1996. ISSN 1432-0916. doi:10.1007/BF02108818.

[205] Marco Merkli. Positive commutators in non-equilibrium quantum statistical mechanics. *Communications in Mathematical Physics*, 223(2):327–362, Oct 2001. ISSN 1432-0916. doi:10.1007/s002200100545.

[206] Volker Bach, Jürg Fröhlich, and Israel Michael Sigal. Return to equilibrium. *Journal of Mathematical Physics*, 41(6):3985–4060, 2000. doi:10.1063/1.533334.

[207] Marco Merkli. Correlation decay and markovianity in open systems. *arXiv preprint*, 2021. doi:10.48550/ARXIV.2107.02515.

[208] Marco Merkli. Dynamics of Open Quantum Systems I, Oscillation and Decay. *Quantum*, 6:615, January 2022. ISSN 2521-327X. doi:10.22331/q-2022-01-03-615.

[209] Marco Merkli. Dynamics of Open Quantum Systems II, Markovian Approximation. *Quantum*, 6:616, January 2022. ISSN 2521-327X. doi:10.22331/q-2022-01-03-616.

[210] Michael E. Fisher. Magnetism in one-dimensional systems—the heisenberg model for infinite spin. *American Journal of Physics*, 32(5):343–346, 1964. doi:10.1119/1.1970340.

[211] Y. K. Wang and F. T. Hioe. Phase transition in the dicke model of superradiance. *Phys. Rev. A*, 7:831–836, Mar 1973. doi:10.1103/PhysRevA.7.831.

[212] Michele Campisi, Peter Talkner, and Peter Hänggi. Fluctuation theorem for arbitrary open quantum systems. *Phys. Rev. Lett.*, 102:210401, May 2009. doi:10.1103/PhysRevLett.102.210401.

[213] Philipp Strasberg and Massimiliano Esposito. Measurability of nonequilibrium thermodynamics in terms of the hamiltonian of mean force. *Phys. Rev. E*, 101:050101, May 2020. doi:10.1103/PhysRevE.101.050101.

[214] S. Nemati, C. Henkel, and J. Anders. Coupling function from bath density of states. *arXiv preprint arXiv:2112.04001*, 2021.

[215] Giacomo Guarnieri, Michal Kolář, and Radim Filip. Steady-state coherences by composite system-bath interactions. *Phys. Rev. Lett.*, 121: 070401, Aug 2018. doi:10.1103/PhysRevLett.121.070401.

[216] Andrew Smith, Kanupriya Sinha, and Christopher Jarzynski. Quantum coherences and classical inhomogeneities as equivalent thermodynamics resources. *Entropy*, 24(4), 2022. ISSN 1099-4300. doi:10.3390/e24040474.

[217] P. Kammerlander and J. Anders. Coherence and measurement in quantum thermodynamics. *Scientific Reports*, 6(1), feb 2016. doi:10.1038/srep22174.

[218] H.-H. Hasegawa, J. Ishikawa, K. Takara, and D.J. Driebe. Generalization of the second law for a nonequilibrium initial state. *Physics Letters A*, 374(8):1001–1004, 2010. ISSN 0375-9601. doi:https://doi.org/10.1016/j.physleta.2009.12.042.

[219] Jake Iles-Smith, Neill Lambert, and Ahsan Nazir. Environmental dynamics, correlations, and the emergence of noncanonical equilibrium states in open quantum systems. *Phys. Rev. A*, 90:032114, Sep 2014. doi:10.1103/PhysRevA.90.032114.

[220] Jake Iles-Smith, Arend G. Dijkstra, Neill Lambert, and Ahsan Nazir. Energy transfer in structured and unstructured environments: Master equations beyond the born-markov approximations. *The Journal of Chemical Physics*, 144(4):044110, 2016. doi:10.1063/1.4940218.

[221] Ahsan Nazir and Gernot Schaller. The reaction coordinate mapping in quantum thermodynamics. In *Fundamental Theories of Physics*, pages 551–577. Springer International Publishing, 2018. doi:10.1007/978-3-319-99046-0_23.

[222] Luis A. Correa, Buqing Xu, Benjamin Morris, and Gerardo Adesso. Pushing the limits of the reaction-coordinate mapping. *The Journal of Chemical Physics*, 151(9):094107, 2019. doi:10.1063/1.5114690.

[223] Camille L. Latune. Steady state in strong system-bath coupling regime: Reaction coordinate versus perturbative expansion. *Phys. Rev. E*, 105: 024126, Feb 2022. doi:10.1103/PhysRevE.105.024126.

[224] Alexia Auffèves. Quantum technologies need a quantum energy initiative. *PRX Quantum*, 3:020101, Jun 2022. doi:10.1103/PRXQuantum.3.020101.

[225] S. V. Halilov, H. Eschrig, A. Y. Perlov, and P. M. Oppeneer. Adiabatic spin dynamics from spin-density-functional theory: Application to fe, co, and ni. *Physical Review B*, 58(1):293–302, jul 1998. doi:10.1103/physrevb.58.293.

[226] M.-C. Ciornei, J. M. Rubí, and J.-E. Wegrowe. Magnetization dynamics in the inertial regime: Nutation predicted at short time scales. *Physical Review B*, 83(2), jan 2011. doi:10.1103/physrevb.83.020410.

[227] E. Beaurepaire, J.-C. Merle, A. Daunois, and J.-Y. Bigot. Ultrafast spin dynamics in ferromagnetic nickel. *Physical Review Letters*, 76(22):4250–4253, may 1996. doi:10.1103/physrevlett.76.4250.

[228] L. Chen, S. Mankovsky, S. Wimmer, M. A. W. Schoen, H. S. Körner, M. Kronseder, D. Schuh, D. Bougeard, H. Ebert, D. Weiss, and C. H. Back. Emergence of anisotropic gilbert damping in ultrathin fe layers on GaAs(001). *Nature Physics*, 14(5):490–494, mar 2018. doi:10.1038/s41567-018-0053-8.

[229] Federico Cerisola, Marco Berritta, Stefano Scali, Simon A. R. Horsley, James D. Cresser, and Janet Anders. Quantum-classical correspondence in spin-boson equilibrium states at arbitrary coupling. *arXiv preprint*, 2022. doi:10.48550/arXiv.2204.10874.

[230] Felix Hartmann, Stefano Scali, and Janet Anders. Anisotropic signatures in the spin-boson model. *arXiv preprint*, 2023. doi:10.48550/arXiv.2305.16964.

[231] Marco Berritta, Stefano Scali, Federico Cerisola, and Janet Anders. Accounting for quantum effects in atomistic spin dynamics. *arXiv preprint*, 2023. doi:10.48550/arXiv.2305.17082.

[232] Jonas Glatthard, Charlie Hogg, Federico Cerisola, and Janet Anders. In preparation, 2023.

[233] Shishir Khandelwal, Nicolas Brunner, and Géraldine Haack. Signatures of liouvillian exceptional points in a quantum thermal machine. *PRX Quantum*, 2(4), dec 2021. doi:10.1103/prxquantum.2.040346.

[234] Ángel Rivas, Susana F. Huelga, and Martin B. Plenio. Entanglement and non-markovianity of quantum evolutions. *Physical Review Letters*, 105(5), jul 2010. doi:10.1103/physrevlett.105.050403.